CENTER FOR INFRASTRUCTURE ENGINEERING STUDIES

Post-earthquake Damage Evaluation of Bridge Structures

By

G. Chen
N. Anderson
R. Luna
R. Stephenson
M. Engebawy
P. Silva
&
R. Zoughi

University Transportation Center Program at

The University of Missouri-Rolla

UTC R90

Disclaimer

The contents of this report reflect the views of the author(s), who are responsible for the facts and the accuracy of information presented herein. This document is disseminated under the sponsorship of the Department of Transportation, University Transportation Centers Program and the Center for Infrastructure Engineering Studies UTC program at the University of Missouri - Rolla, in the interest of information exchange. The U.S. Government and Center for Infrastructure Engineering Studies assumes no liability for the contents or use thereof.

Technical Report Documentation Page

1. Report No.	2. Government Accession No.	3. Recipient's Catalog No.
UTC R90		

4. Title and Subtitle	5. Report Date
Post-earthquake Damage Evaluation of Bridge Structures	December 2005
	6. Performing Organization Code

7. Author/s	8. Performing Organization Report No.
G. Chen, N. Anderson, R. Luna, R. Stephenson, M. Engebawy, P. Silva, & R. Zoughi	**RG001232 OTO90**

9. Performing Organization Name and Address	10. Work Unit No. (TRAIS)
Center for Infrastructure Engineering Studies/UTC program University of Missouri - Rolla 223 Engineering Research Lab Rolla, MO 65409	11. Contract or Grant No. DTRS98-G-0021

12. Sponsoring Organization Name and Address	13. Type of Report and Period Covered
U.S. Department of Transportation Research and Special Programs Administration 400 7th Street, SW Washington, DC 20590-0001	Final
	14. Sponsoring Agency Code

15. Supplementary Notes

16. Abstract

The New Madrid Seismic Zone (NMSZ) is the location of several of the largest earthquake events (1811–1812) in the contiguous United States. Due to the infrequent nature of earthquake occurrence in this region, little attention has been paid in the past three decades to its potential threat to regional and national transportation infrastructure. This potential threat is real as inferred from the January 26, 2001, Kutch Earthquake in India, which occurred in a seismic and geological environment similar to the NMSZ and resulted in an estimated 0.45 million deaths and injuries as well as $5 billion in economic losses. This study represents the first systematic investigation in the vicinity of the NMSZ, involving seismologists, geologists, geotechnical and structural engineers, and economists. The objective of this study is to improve earthquake resistance and mitigate earthquake damage to highway transportation networks, including loss of bridges and highways. This is accomplished by developing new seismic design and assessment methodologies, by improving seismic retrofitting measures, and by exchanging and transferring new technologies. The main topics of this study included near-field rock and ground motion, deep soil deposit response, bridge response to near-field ground motion, seismic retrofit of bridge systems, loss estimation methodology, and post-earthquake assessment of structural conditions.

17. Key Words	18. Distribution Statement
Earthquake hazards, condition assessment, site response analysis, largescale test, seismic retrofit, near-field ground motion, composite source model, loss estimation.	No restrictions. This document is available to the public through the National Technical Information Service, Springfield, Virginia 22161.

19. Security Classification (of this report)	20. Security Classification (of this page)	21. No. Of Pages	22. Price
unclassified	unclassified	73	

Form DOT F 1700.7 (8-72)

POST-EARTHQUAKE DAMAGE EVALUATION OF BRIDGE STRUCTURES

G. Chen[1], R. Zoughi[2], R. McDaniel[3], and J. Nadakuduti[4]

1. Associate Professor of Civil Engineering, Department of Civil, Architectural, and Environmental Engineering, 328 Butler-Carlton Hall, 1870 Miner Circle, University of Missouri-Rolla, Rolla, MO 65409-0030
2. Schlumberger Professor of Electrical Engineering, Department of Electrical and Computer Engineering, 224 Emerson Hall, 1870 Miner Circle, University of Missouri-Rolla, Rolla, MO 65409-0030
3. M.S. Graduate Student, Department of Civil, Architectural, and Environmental Engineering, 113 Butler-Carlton Hall, 1870 Miner Circle, University of Missouri-Rolla, Rolla, MO 65409-0030
4. M.S. Graduate Student, Department of Electrical and Computer Engineering, Engineering Research Laboratory, 1870 Miner Circle, University of Missouri-Rolla, Rolla, MO 65409-0030

This project was supported in part by the Missouri Department of Transportation (MODOT), Federal Highway Administration (FHWA), and University of Transportation Center (UTC) at the University of Missouri-Rolla (UMR).

TABLE OF CONTENT

LIST OF FIGURES

LIST OF TABLES

POST-EARTHQUAKE DAMAGE EVALUATION OF BRIDGE STRUCTURES

Bridges, as important components of civil infrastructure, particularly column members and beam-column joints in substructures, are vulnerable to lateral earthquake loading. Immediately after a major earthquake event, the most pressing need is to send emergency vehicles and rescue teams to the affected areas. To meet the urgent need, all bridges along a predesignated emergency vehicle access route have to be evaluated within several hours, if not sooner, to ensure the bridges are safe for emergency vehicles. The current practice, visual inspections of the structural condition of highway bridges, often leads to overconservative conclusions. A decision could be made to close a bridge when it is still capable of carrying reduced traffic loads. More important, damage such as excessive cracks in reinforced concrete (RC) columns is often undetectable under a moderate earthquake event since gravity load will close the cracks immediately after the event. A quantitative method is therefore needed as a complementary tool to make a more sensible decision on the condition of those bridges that is undetectable or unclear from visual inspections.

The impact of such a quantitative method on the post-earthquake emergency rescue and reconstruction is not only an economic issue, but may also be a life threatening/safety matter. Since approximately 50% of the bridges in the U.S. National Bridge Inventory database have either RC or prestressed superstructures and significantly higher percentage for RC substructures (Small, 1998), the implementation of a quantitative method could save thousands to millions of dollars in emergency operations due to the continuous function of critical bridges along a designated emergency vehicular access route that could otherwise be closed from visual inspections. Such a method could also indirectly save lives, since emergency vehicles would not have to detour and could therefore arrive at the affected area sooner.

During a moderate earthquake event, RC members may be subjected to minor or medium damages, such as cracks at plastic hinges. Although cracks are visible on beams, those on columns are often undetectable by visual inspection because of gravity load effects. In either case, it is desirable to determine the residual strength of steel reinforcements that are covered by cracked concrete. The mapping of cracks on the surface of an RC member may yield useful information for this purpose. Consequently, both crack sensor and near-field microwave guiding devices were used to detect shear and flexural cracks, and evaluate their width, extent, and spatial distribution on RC members (Yeh, 1994a; Huber et al., 1997a, 1997b; Chen et al., 2004).

The objectives of this chapter are to propose a new framework for the structural condition assessment of RC structures, develop two electromagnetic waveguide systems for the detection of cracks in RC structural members, validate the technology with the large-scale testing of structures, and discuss the potential for practical implementation of the developed technologies.

CRACK DETECTION SENSORS AND THEIR PRINCIPLES

Several nondestructive evaluation (NDE) techniques, such as ultrasonic, acoustic emission, and eddy current, have been available for years (Zoughi, 2000). They were shown to be effective in detecting damage in various applications. These tools are exclusively used to determine the

severity of damage at a specific location of a structure. However, it is not always feasible to determine the location of potential damage in complex civil engineering structures prior to testing. New ways of evaluating the structural condition of RC members are thus needed.

New Framework for RC Structural Condition Assessment

A three-level strategy is proposed in this chapter to assess the damage of an RC structural system using electromagnetic wave-guiding tools. The first level of detection is to apply the recently developed, distributed cable sensors to locate and detect the near-surface cracks in any major member of the structure (Chen et al., 2004). The second level of detection is to apply microwave technology to refine the crack distribution at critical locations, such as near the beam-column joints or where the first-level detection has indicated the occurrence of excessive cracking. The third and last level of detection is to infer the structural condition of the member from the measured crack patterns (Nazmul and Matsumoto, 2003). Following is a presentation of the development, validation, and application of cable sensors and microwave technology toward the accomplishment of the first two-level detection in the proposed strategy.

Distributed Cable Sensors

Mechanism

The distributed crack sensors are actually coaxial cables. Two different designs of cables have been studied thus far. In the previous study by Chen et al. (2004), each sensor consists of a solid inner conductor, a spirally wrapped copper tape outer conductor, and a rubber tube in between the conductors as dielectric, which is referred to as a rubber sensor in this report. It differs from a commercial coaxial cable in that the topology of the outer conductor of the sensor can change with the onset of a crack in the concrete in which it is embedded. For example, Figure 1 shows the change of current flow path on the outer conductor of the sensor. When two spirals that are originally in perfect contact are partially separated, the original continuous cylindrical outer conductor at zero load becomes spiral at the location of partial separation, and thus changes the topology of the sensor. This topological change results in a detour of the current path. Therefore, one of the most critical sensor parameters is the mechanism to allow partial separation of two adjacent spirals. In the case of rubber sensors, the outer spirals are bonded with adhesive on the rubber tube and it is the flexibility of the rubber tube that enables the separation of spirals when subjected to a pair of equal but opposite forces (Chen et al., 2004).

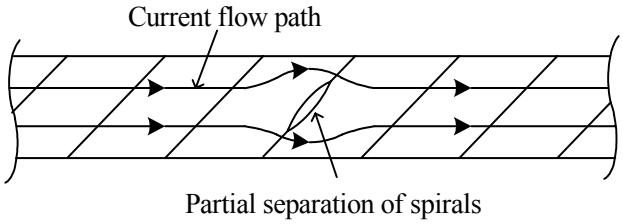

Figure 1 Current flow change due to separation of spirally wrapped outer conductor.

New Design of Sensors and Their Physical Properties

The new design of crack sensors differs from the rubber sensors in the use of dielectric material and in the fabrication process of their outer conductor. The new sensor is made up of an inner conductor, a rigid dielectric material, and an outer conductor which is coated with a layer of solder, as can be seen in Figure 2. The inner conductor is made up of 10-gauge twisted silver plated copper wires surrounded with a PTFE (Teflon) dielectric. As such, the sensor is herein referred to as a Teflon sensor. The outer conductor of the sensor is a stainless steel spiral material. The inner conductor is 2.8 mm (0.11 in.) in diameter and the dielectric material is 0.35 mm (0.014 in.) thick, while each turn of the spiral is 3.0 mm (0.12 in.) in width, as shown in Figure 2. The spiral is wrapped without adhesive around the dielectric in such a way as to ensure that each turn of the spiral is touching edge to edge without any gap or overlapping. The spiral can therefore slide along the dielectric. A thin coat of solder is then evenly applied over the entire surface of the spiral enabling the spiral to remain in place and allowing for a continuous axial current path over the surface of the outer conductor at zero loading. The solder is strong enough to hold the spirals in place while still allowing for the spirals to separate when the concrete surrounding the sensor cracks and pulls the spirals apart. This enables the outer conductor to be electrically continuous but mechanically separate. The sensors can be embedded in 1.27 cm × 1.27 cm (½ in. × ½ in.) channels in the face of RC members and grouted into the channel using a masonry grout. When the crack propagates across the channel containing the sensor, the grout also cracks with the member. The grout adheres to the outer conductor of the sensor and when it cracks, the spiral is separated.

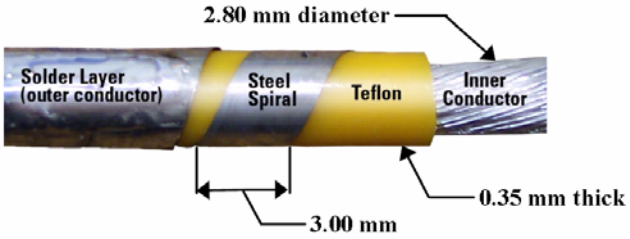

Figure 2 Cut-away sample of a Teflon sensor.

Signal Measurement

The measurement principle implemented in the crack detection system is electrical time-domain reflectometry (ETDR). This involves sending a pulse down a signal carrier, cable or sensor, and the reflection of that signal is then sampled, as illustrated in Figure 3. With a sampling device, time-domain reflectometer (TDR), a bandwidth of 20 GHz can be achieved for repetitive signals at a sampling rate of 200 kHz, using equivalent sampling techniques. If there is an impedance change or discontinuity at one location along the length of the cable, the reflection of the input signal at that location will be distinguishable from the remaining portion. This discontinuity is because of some type of change or interruption in the path of current. This is brought about by either a geometric change of the cable cross-section, or by a change in topology of one of the conductors. In the case of the distributed crack sensors in this study, the change in topology of the outer conductor is what causes an interruption of current flow at the location of a crack in the concrete, as illustrated in Figure 1. When the crack in the concrete propagates across the sensor, the solder across the joint between the spirals at that location is broken and the spirals are pulled

apart. This causes a change in the current path, resulting in a signal discontinuity and reflection in the sensor at that particular location. How much separation between spirals and how many spirals are pulled apart determines the amplitude of the reflected signal. It is in this way that the relative size of the crack can be determined by relating it to the amplitude of the reflected signal. Figure 4 shows a typical sensor signal in real-time as seen on the screen of the TDR (top line only). The location of the discontinuity along the length of the sensor can also be determined from the delay time of the reflected wave. The signal on the sampling device shows the electrical equivalent of the sensor on the screen in time versus the reflection coefficient, which is a measure of how much of the signal is reflected. This reflection coefficient is directly related to the discontinuity in the sensor at the point of deformation (Chen et al., 2004). Since the material properties of the sensor are known, the velocity of the signal can be determined and the time can be directly converted into length, which allows for correlation between the electrical location of the discontinuity and the physical location of the crack.

Before any cracking occurs, a baseline signal is recorded. This baseline is subtracted from all data taken during testing to get a better understanding of what changes are taking place in the sensor. Although the cracks that occur can easily be seen from the raw signal, taking out a baseline shows more clearly the change in the reflected signal at the onset of a crack.

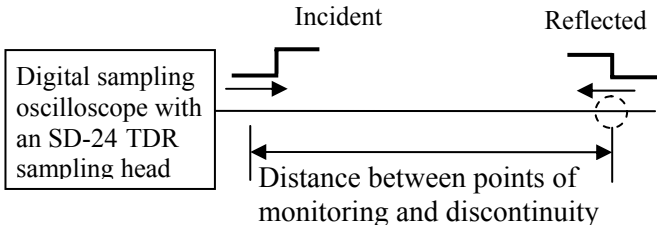

Figure 3 ETDR measurement principle.

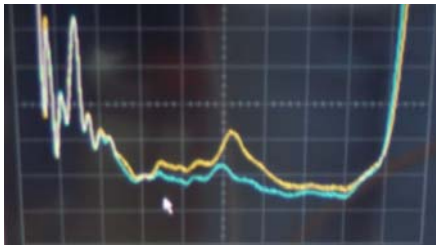

Figure 4 Real-time snapshot (top) and baseline data (bottom).

State-of-the-Art Development

Since the 1950s, ETDR has been applied to power and telecommunication industries to locate and identify faults in transmission cables. The technology slowly began to develop some applications in geotechnics in the 1970s. More recently, its applications have been extended to various topics including the characterization of solute transport parameters (Vanclooster et al., 1993), monitoring of abandoned mines (O'Connor and Murphy, 1997), determination of the volumetric water content of soils in triaxial testing (Grozic et al., 2000), and identification of the causes of ground penetration radar reflections (Van Dam and Schlager, 2000). These applications can be categorized into two groups. The first group includes the detection of leakage in pipelines and the measurement of soil water content, soil salinity, contaminant transport, ground water levels, and moisture changes in embankments and pavements. This group of applications is based on the change in dielectric permittivity of the cable due to liquid permeation. The second group includes the measurement of rock and soil deformation, remote monitoring of slope movement, and monitoring of mine stability. This group of applications is based on the change in local capacitance of the cable, which results from the change in cross-section as a result of external loading. A state-of-the-art review by Benson and Bosscher (1999) and the book by

O'Connor and Dowding (1999) summarized the recent development in geo-applications. Several doctoral dissertations documented most of the original works (Su, 1987; Pierce, 1998).

However, the use of ETDR for the purpose of damage detection of structures is just beginning. Unlike the rock masses or other geotechnical facilities that often undergo significant movement in a widespread area, overstress and damage in structures are often localized before the structures become unstable. The key issue in this application is to improve the sensitivity of cables to local disturbances such as shear and tension effects. At present, its application is limited to RC structures. Specifically, transmission cables are embedded into concrete specimens and, as distributed sensor, they are able to measure the change of characteristic impedance as a result of an external disturbance. Calibrated with actual damage in structures, the change in impedance can be used as a damage indicator.

Several investigators have applied ETDR to detect crack development in RC structures. Su (1987) and Lin et al. (1998) embedded commercial communication cables into small-scale RC beams for this purpose. Their test results did not indicate a strong correlation between the change in impedance of the cable used and the crack development in the beam. This is because the cable was insensitive to the axial deformation associated with the developed crack. To increase sensitivity, Lin et al. (2000) designed and fabricated a new cable. They used rubber as a dielectric medium of the cable instead of polyethylene or Teflon materials that are used in commercial cables. Rubber was selected because of its low stiffness so that large deformation is expected to occur when the cable is subjected to an external load. The new cable has been tested and shown to be approximately ten times more sensitive than commercial cables. However, cables are subject to strain effects when embedded in concrete. Under this condition, the sensitivity of a commercial type of cable to external disturbances is too low to be distinguishable from noises in structural applications (Chen et al., 2004), irrespective of the dielectric materials used in the design of the cable.

Microwave Technology

Microwave NDE techniques have several advantages including the use of low power, provision for noncontact, one-sided and real-time measurement capabilities, and being small, hand-held and operator friendly (Zoughi, 2000; Shull, 2002). Microwave signals have the ability to penetrate inside of dielectric (nonmetallic) materials. They are also sensitive to dielectric, volumetric, geometric, and size distribution of a mixture and its constituents. So, any variation in the local dielectric properties (such as presence of a crack) can be readily detected. This makes these techniques suitable for material property characterization and detection of defects in dielectric media (Qaddoumi, 1998; Bois, 1999; Peer, 2002). Several measurements were conducted on artificial/simulated cracks and also on cracks generated by externally loading mortar and RC specimens. The results of these measurements were analyzed and an electromagnetic model was also developed to simulate crack characteristic signal given the crack dimensions and dielectric property of a cement-based structure.

NUMERICAL SIMULATIONS OF CABLE SENSOR PERFORMANCE

Finite Difference Time Domain Analysis

Four types of prototype sensors were considered for the crack detection of RC beams and columns; they are discussed later. Their dimension and characteristic impedance are presented in Table 1. The diameter of the sensors and the width of the copper tape were determined based on the availability of commercial materials and the insights gained through the analytical study (Mu, 2002). They can be classified into two groups by size. Sensor-I and Sensor-II have a larger diameter of outer and inner conductors than Sensor-III and Sensor-IV. Each group has two cables made of copper tapes of different widths. The dimension of a cable determines its characteristic impedance and the value of a lumped inductance. The width of the copper tape determines the density of separation turns, which leads to different lumped inductances.

Table 1 Types of prototype sensors simulated.

Sensor	Diameter of the inner conductor (mm)	Diameter of the outer conductor (mm)	Width of spirally wrapped copper tapes (mm)	Characteristic impedance (Ω)
I	0.794	7.938	3.175	97
II	0.794	7.938	6.350	97
III	0.605	3.175	3.175	69
IV	0.605	3.175	6.350	69

Before each sensor was embedded into concrete, its response to an applied strain was numerically studied with the FIDELITY software. A Finite Difference Time Domain (FDTD) model was established for each sensor. One such model is illustrated in Figure 5 when the spirally wrapped copper tape of a sensor is completely separated for one to four turns. A round bar was used to model the inner conductor of the sensor. For its outer conductor, sufficiently thin spiral wires were implemented in the FIDELITY and they were accumulated to model a spirally wrapped copper tape. A small gap between two adjacent spiral wires was created to represent the separation between two rounds of spiral tapes. The sensors were excited by a Gaussian impulse, which was integrated over time to obtain the ETDR voltage waveform. By definition, the reflection coefficient can be determined from the voltage waveform (Rao, 2002).

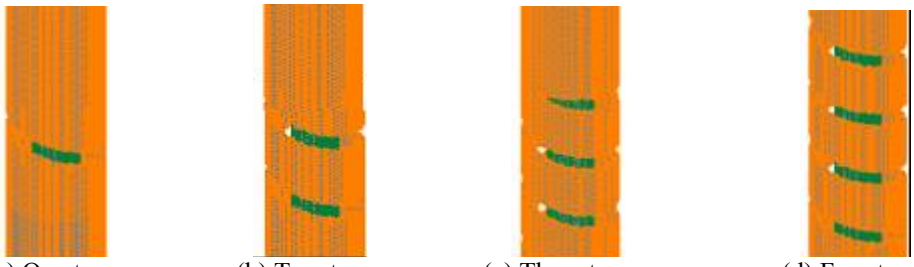

(a) One turn (b) Two turns (c) Three turns (d) Four turns

Figure 5 FDTD model of sensors under various turns of separation.

Figure 6 presents the simulated results or reflection waveforms of one sensor, Sensor-III in Table 1, over the length of approximately 100-mm (3.94 in.) cables as various turns of separation are considered. Only a portion of the reflected wave around the separation of spiral tapes is given in

the figure. A decimal value for the turn of separation means a partial separation of spiral tapes. For example, 0.2 turns mean that two adjacent rounds of spiral tapes are separated in length by 20% of one complete turn. It is seen from the simulation results that the sensor is very sensitive to the topological change of the outer conductor. One turn of separation changes the reflection coefficient by approximately 40 milli rho. By increasing the turns of separation, both the peak value and the bandwidth of the waveform increase.

It can be inferred from Figure 6 that as more turns of the spiral tapes are separated, the reflection coefficient increases almost linearly at the beginning and then nonlinearly at a reduced increasing rate. This is because the reflection coefficient increases nonlinearly with a lumped inductance, L_{gap}, which is in turn proportional to the square of the turn of separation (Mu, 2002). For a small value of the turn of separation or a small separation of spiral tapes, the reflection coefficient of the cable seems to increase linearly. With further development of more separations, the boundary effect from the far end of the wave propagation attenuates and, therefore, the maximum reflection coefficient at the near end of the cable approaches an asymptotical value corresponding to an infinitely long cable with the uniformly distributed separation of spiral tapes.

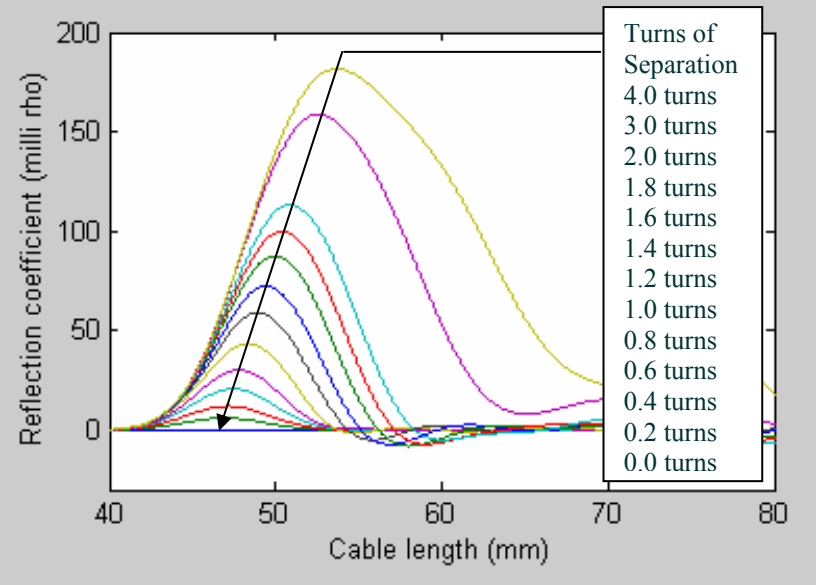

Figure 6 Numerical reflection waveform of Sensor-III.

Interrelation Between Reflection Coefficient, Crack Width, and Lumped Inductance

When the outer conductor of a cable is separated at a loading point, the tube of the outer conductor that was originally cylindrical becomes a spiral coil of copper tape. To describe the extent of separation along the cable that is directly related to crack width, the length of separation is defined as the cable length over which separation(s) occurs, regardless of the gap size between any two spiral rounds. Since the length of separation is directly related to the crack width when a cable sensor is embedded in concrete, it is more relevant to describe the sensor behavior with the length of separation and the turn density. The turn density is defined as the ratio between the turns of separation and the length of separation. Figure 7 presents the reflection coefficient at the loading point as a function of the length of separation. It can be observed that

the sensors made of 3.175 mm (0.125 in.)-wide copper tapes, Sensor-I and Sensor-III, have a larger value of the reflection coefficient because of their higher turn density. The higher turn density corresponds to a larger value of lumped inductance for a given length of separation, and thus a larger reflection coefficient. The highest slope of the curves in Figure 7 corresponds to the most sensitive range of the sensors with respect to the length of separation. This range can be used to guide the optimum design of a sensor. For all four sensors, this range is up to 7.5 mm (0.3 in.), which is significantly higher than the width of a concrete crack of engineering interest (Nawy, 2003). Therefore, the design of all sensors seems appropriate for RC members. However, in terms of the length of separation, Sensor-I and Sensor-III are more sensitive than the other two, as clearly suggested in Figure 7.

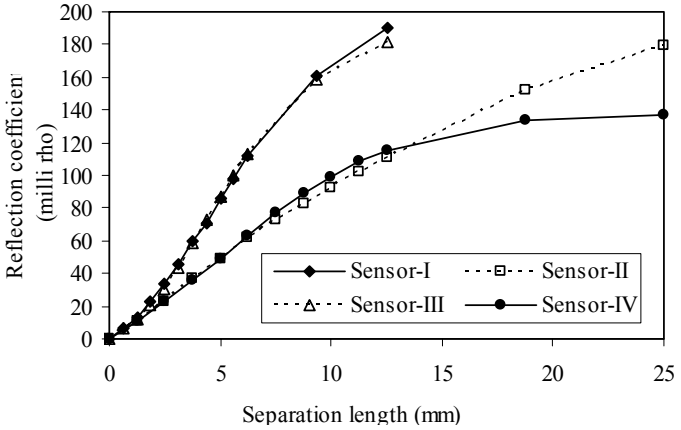

Figure 7 Increase of reflection coefficient with separation length.

To fully understand the sensors performance, it is helpful to examine the value of lumped inductance associated with the separation of adjacent rounds of spiral tapes. A lumped inductance in the order of nano Henry can be determined based on the ETDR waveform from the analytical results (Mu, 2003). For the four sensors under investigation, the reflection coefficient can be plotted as a function of the lumped inductance, as illustrated in Figure 8. The reflection coefficient increases nonlinearly with a lumped inductance. For a lumped inductance of one nano Henry, the reflection coefficient is over 50 milli rho. The lower the characteristic impedance of a sensor, the higher the sensitivity of the sensor will be. In terms of lumped inductances, Sensor-III and Sensor-IV seem more sensitive than the other two sensors, as illustrated in Figure 8.

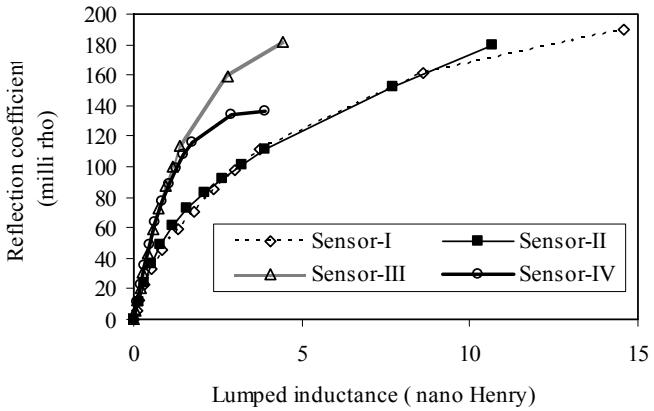

Figure 8 Increase of reflection coefficient with lumped inductance.

CALIBRATION AND VALIDATION OF CABLE SENSOR PERFORMANCE

Cable Calibration With Applied Strain

When embedded in concrete, a cable sensor is used to measure the elongation at the location of the cracks. To correlate the reflection coefficient from ETDR measurements with the normalized elongation or "strain" applied on the sensor, calibration tests were conducted before the sensors were put into concrete beams. Since the relation between four prototype sensors can be understood by numerical simulations, in this study only Sensor-III was considered for experimental calibration. Sensor-III was a rubber sensor made with a single wire of 24 AWG. To investigate the effect of separation turns on the reflection coefficient, the sensors tested had a varying number of turns of the spirally wrapped copper tape.

Tensile Test Setup of Cables

Each prototype cable was set up in a horizontal position during tests. The overall setup of a calibration test, the required data acquisition and their schematic representations are shown in Figure 9(a, b), respectively. Since rubber is very flexible and can be easily stretched with a small load, the cable was loaded at both ends with a pair of equal loads to minimize the potential deformation at the fixed support. To reduce the potential sagging of the cable to a minimum, an additional support was provided around the mid-span. The elongation of the cable was measured with an LVDT toward the right end of the cable, as illustrated in Figure 9(b). To investigate the effect of separation turns on the reflection coefficient, only a portion of the tested cables with different separation turns was made with the new design, and the remaining part is similar to commercial cables. The elongation of the newly designed cable was calculated from the measured deflection over the entire length of the cable based on the relative stiffness factors between the new and the existing designs. The elongation of the cable was finally converted into the strain applied on the portion of the newly designed cable by dividing the elongation by the base length.

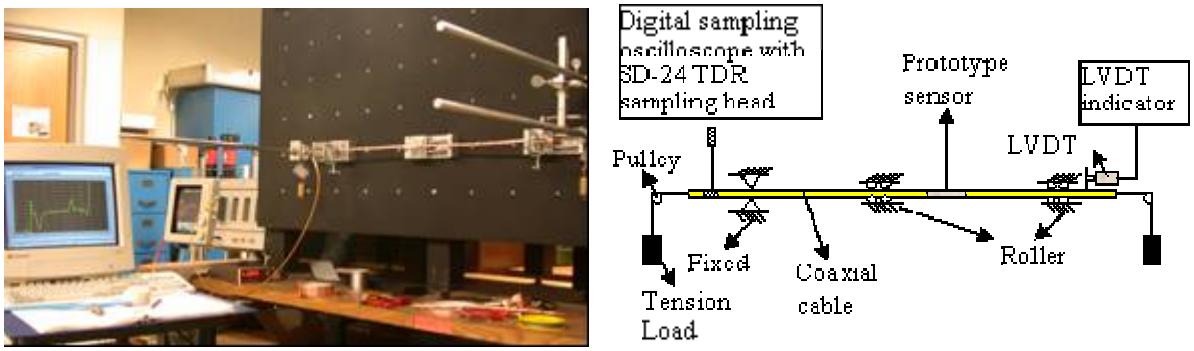

(a) Overview (b) Schematic representation

Figure 9 Cable setup for calibration tests.

Calibration Test Results and Analysis

In practical applications, when a cable sensor is embedded in concrete, the number of completely separated turns of its outer conductor spirals is likely limited to three. Therefore, only the sensors

within three complete turns of the spirally wrapped copper tape were calibrated under various strain levels. For repeatability of test data, three identical cables were made with each number of turns. Each cable was identified by the number of turns and its sequence. The number of separation turns was expressed by English words such as one, two, and three, while their sequence was represented by numerical numbers such as 1, 2, and 3. For example, "one2" represents the second cable of Sensor-III with one complete turn of the spirally wrapped tapes.

A total of nine cables were tested in calibration studies. With the exception of the first one where test data is unavailable due to an unstable boundary condition, the reflection coefficient of each cable corresponding to the peak value of reflection waveforms is shown in Figure 10 as a function of the strain applied on it. Figure 10 illustrates virtually no reflection of the eight cables at zero strain, indicating that two adjacent rounds of the copper tapes of each cable are electrically in nearly perfect contact. In the strain range of engineering interest up to 0.002 (corresponding to the yielding strain of a Grade 60 steel rebar), the reflection coefficient of all sensors ranges approximately from 25 to 110 milli rho, which is substantially higher than what was expected of a commercial cable based on its geometric change or within one milli rho from the previous analysis. The new design therefore improves the cable sensitivity by 25–110 times over the commercial cables. Except for Cable "three1," the cables of an identical design generally have consistent performance when each is subjected to a strain of 0.001 or higher. Within the strain level of 0.001, however, the variation of reflection coefficients for identical cables increases, especially for the cables of three complete spiral wrappings. Related to the initial separation of any two adjacent rounds of spirally wrapped tapes, the inconsistency in performance is mainly due to the nonuniformity of the cable fabrication by hand. This factor can be corrected when in the future an automatic production line becomes available for practical applications. Note that Cable "three1" is not as sensitive to the applied strain as the other two cables of the same design. It was observed during tests that the copper tape spirals (outer conductor) of Cable "three1" sensor gradually separated under strain actions, while the other two separated rapidly from the beginning. It was found that, at the strain level of 0.0045, three rounds of spiral tapes of the sensor had not separated completely. It was believed that, with an increasing strain, the peak reflection coefficient of the sensor will approach 120 milli rho as the other two sensors do.

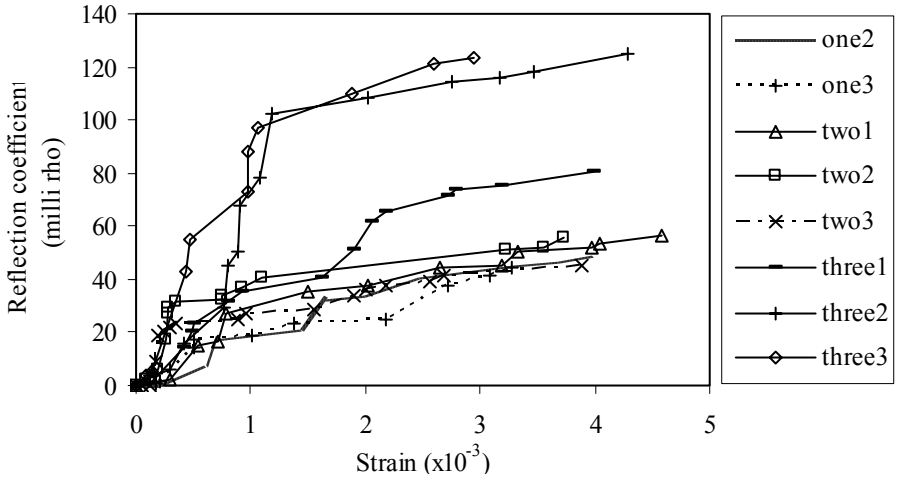

Figure 10 Summary of cable calibration test results for Sensor-III.

It can also be seen from Figure 10 that, on the average, the cables with two turns of spiral wrapping in their outer conductor are slightly more sensitive than the cables with one turn of spiral wrapping. Since the portion of continuous outer conductors was made of a spirally wrapped tape that was covered with a continuous copper tape, it was observed during the tests that at the maximum applied strain, the one-turn cables had separated approximately one and a half turns of spiral wrapping in the outer conductor. The two-turn cables, on the other hand, were not completely separated in their spirally wrapped tape. Overall, it can be observed from this figure that the reflection coefficient increases with the separation turns.

To visualize the change in reflection coefficient over the length of a cable, Figure 11 shows the waveforms (difference) of Cable "three3" at various strains with respect to the initial waveform at zero strain. The differenced waveforms are used to remove manufactured defects of a cable that may exist before the cable sensor is subjected to loading. As the applied strain increases, both the amplitude and bandwidth of a waveform increase steadily except for a significant jump at a strain of 4.67×10^{-4}. This significant increase in reflection coefficient corresponds to an appreciable separation of spiral tapes in the outer conductor of the cable.

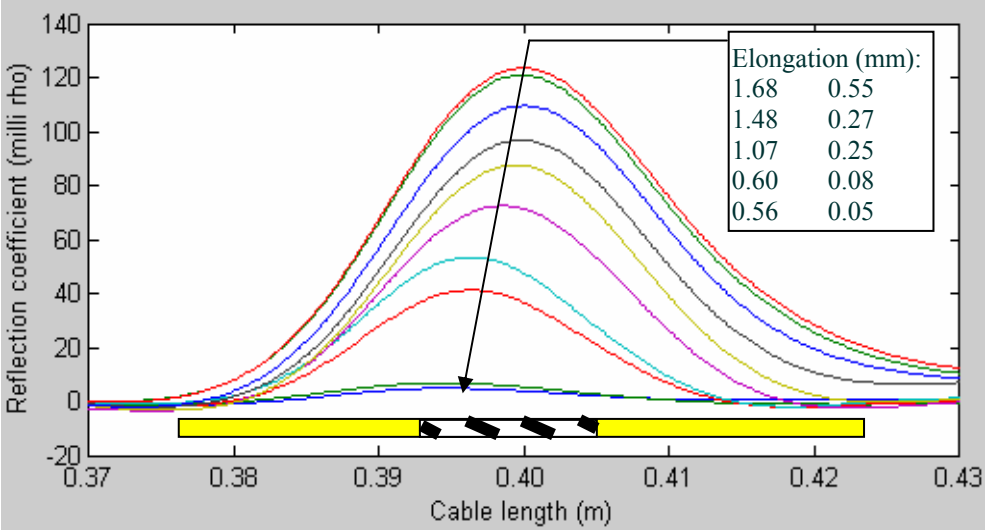

Figure 11 Reflection waveform (difference) over the length of a new cable "three3."

To confirm that the new design of a cable is significantly more sensitive than other similar commercial cable designs, the variation of reflection coefficients along the entire length of Cable "three3" is illustrated in Figure 12. It can be observed that the maximum difference of reflection coefficient at various strains occurs at the location of the new cable. The smaller fluctuations adjacent to the new cable are likely attributable to potential sagging of the cable and transition from the commercial type of design to the new design. This statement is supported by the left span of the cable having a much smaller reflection coefficient associated with its short span length. It is also observed that the reflection coefficient suddenly drops to a minimum at the location of the first support. This is attributable to the cable being tightly clamped during tests to the first support only, significantly reducing the cross-section of the cable or its corresponding reflection coefficient. Additionally, Figure 12 also indicates a level of nonuniform performance of less than 10% "contamination" in reflection coefficient due to imperfection of the cable manufactured by hand, noise effect, and, more important, possible shift in base line. It is noted

that the results shown in Figure 12 are the original recordings, including the initial readings corresponding to zero strain.

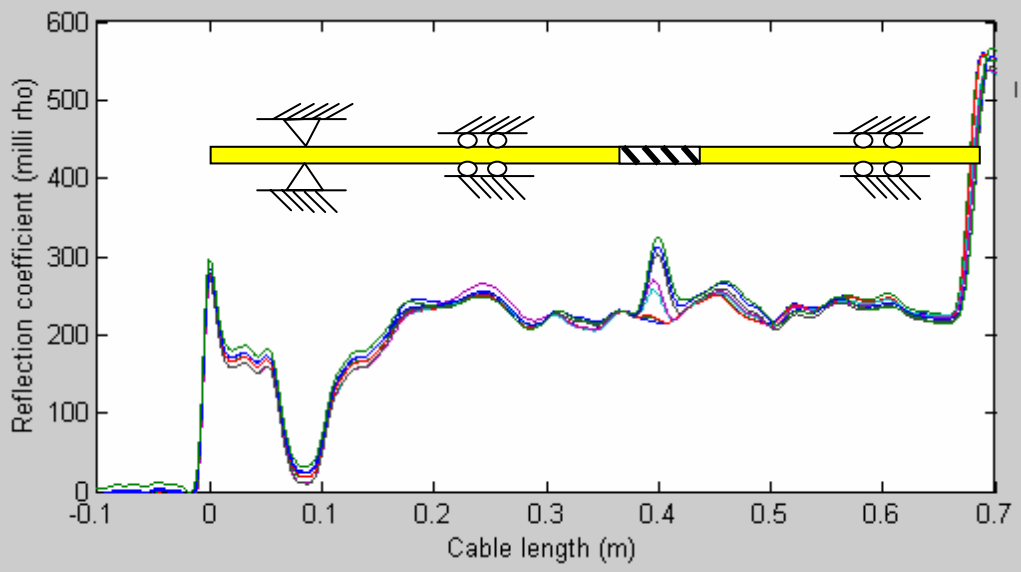

Figure 12 Reflection waveform (original) over the entire length of a cable "three3."

Small- and Large-Scale RC Specimens and Test Setup

Column Specimens

A total of six RC column specimens were tested on the shake table in the high-bay structures laboratory at the University of Missouri-Rolla, as illustrated in Figure 13. The shake table has a payload capacity of 178 kN (20 tons). It operates effectively in a frequency range of 0.1–10 Hz with +/– 2.54 cm (1 in.) stroke. Figure 14 shows the dimensions and reinforcement of the column specimen. Designed with 27.5 MPa (4 ksi) concrete and Grade 60 rebar, each specimen consisted of a footing, a column, and a mass of concrete cast into the top of the column. The footing contained No. 13 (#4 in English Unit) longitudinal reinforcement in both the top and bottom, which was confined by No. 10 (#3) stirrups spaced every 15.24 cm (6 in.). The column was 20.32 cm (8 in.) square in cross-section and 114.3 cm (45 in.) in height. The column reinforcement consisted of four No. 13 (#4) rebars confined by No. 10 (#3) stirrups spaced every 15.24 cm (6 in.). The mass was cast into the top of the column to ensure that the natural frequency of the specimen was within the limit of the shaking table or 10 Hz. The final design of the specimen allowed for a natural frequency before cracking on the order of 8 Hz.

Beam Specimens

A total of six small-scale RC beam specimens, Figure 15, were tested under static and cyclic loading. Each beam was 15.24 cm (6 in.) square in cross-section and 91.44 cm (3 feet) in length, as shown in Figure 16, and was constructed of 27.5 MPa (4 ksi) concrete. All were doubly reinforced; two had No. 10 (#3) reinforcing bars in the tension face (type I), while the other two had No. 13 (#4) reinforcing bars in the tension face (type II). Both had No. 10 (#3) stirrups

spaced at 6.35 cm (2.5 in.) with the compression reinforcement for both types consisting of No. 10 (#3) rebar. A reinforcement schedule for the two types of beams is also given in Figure 16.

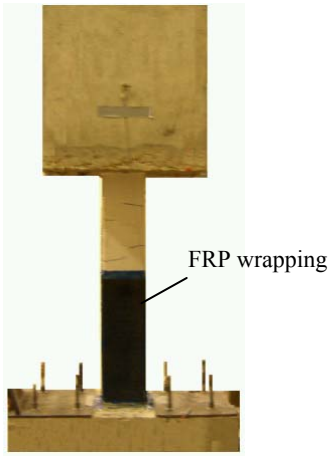

Figure 13 Column specimen.

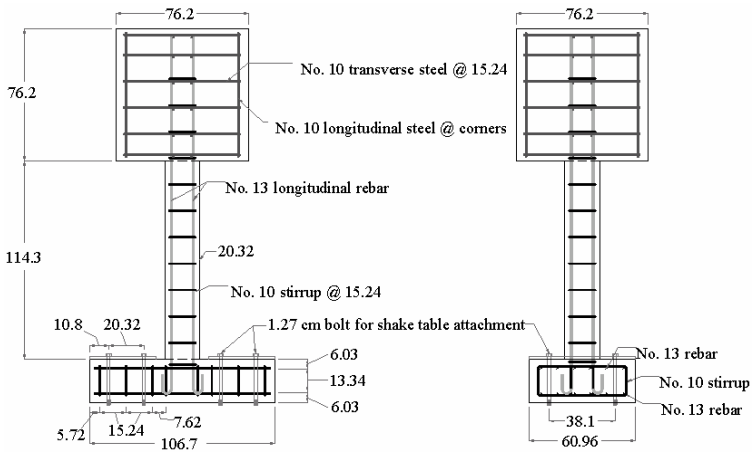

Figure 14 Reinforcement detail (all dimensions in cm).

One Teflon sensor was installed in the tension face of each beam that was tested under a three-point loading system, as shown in Figure 15. The beam was simply supported 7.62 cm (3 in.) from each end, and the load was applied at the center point (mid-span) of the top of the beam through a roller bearing. This series of tests were conducted in three phases. The purpose of the first phase of the experiment was to correlate crack width to the change in the reflected signal with static tests, and to understand the effect of crack width on the memory feature. The second phase was intended to ascertain how many cycles it would take to develop a crack memory with cyclic tests. The last phase was designed to understand the effect of loading rate on the memory feature with additional cyclic tests.

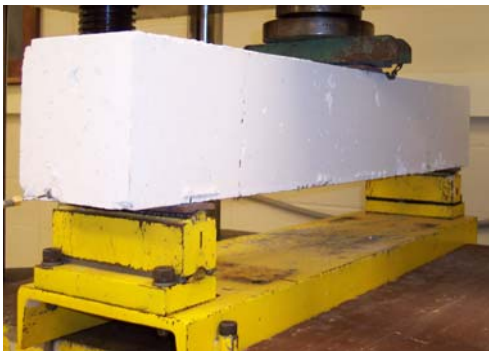

Figure 15 Three-point loaded beam.

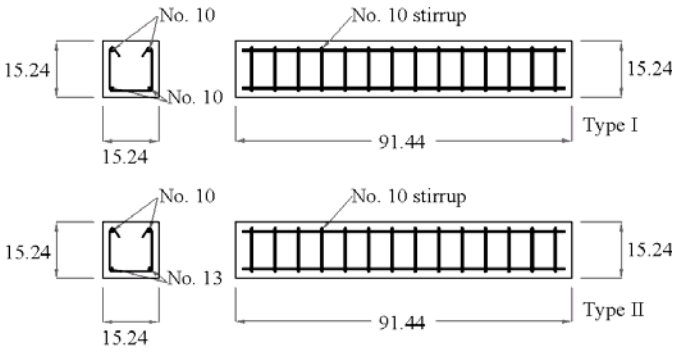

Figure 16 Reinforcement detail (all dimensions in cm).

Beam-Column Specimens

A total of five beam-column specimens were tested as discussed in Chapter 6. The dimensions and reinforcement details of a CEUS bridge specimen were described in Figures 6.6 and 6.7. At least one cable sensor was embedded 1.27 cm (0.5 in.) deep into the tension or compression surface of each specimen for validation of its performance with large-scale structures. In addition, the beam-to-column joint area creates a 90º bend; how a cable sensor responds to the

bend is another reason for this series of tests. For convenience, the physical specimen similar to Figure 6.37 is shown in Figure 17. The detail of cable lengths is illustrated in Figure 18 for the installation of the cable in Specimen #1. Similar deployment of cable sensors are done in Specimen #3, but the length of the sensors may be different.

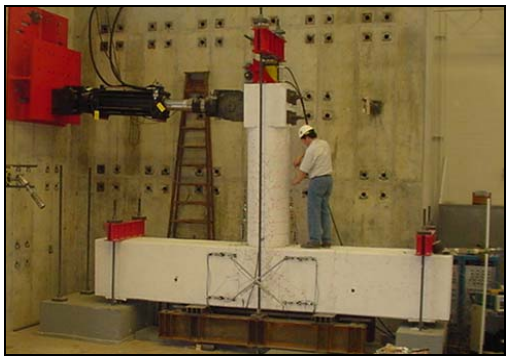

Figure 17 Large-scale beam and column.

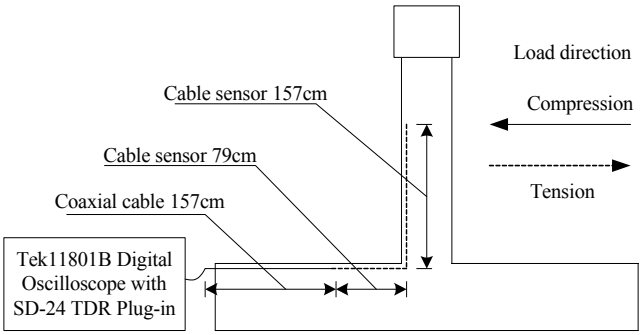

Figure 18 Cable sensor deployment.

Dynamically Loaded Columns on Shake Table

Column Test Matrix and Results

One sensor was installed in each square RC column that was tested under sinusoidal loading. The test matrix of six columns, with and without retrofitting using fiber reinforced polymer (FRP) composites, is presented in Table 2 for the purpose of illustrating both surface and hidden cracks. Each column was tested by incrementally increasing the excitation frequency from 2 Hz to 9 Hz, and then back to 2 Hz in order to obtain useful column response data around the natural frequency of the column. This was done at increasing stroke levels from 0.254 mm (0.01 in.) to 3.81 mm (0.15 in.). In general, the largest stroke level corresponds to fracturing of the vertical reinforcement at the column-footing interface after approximately 20,000 cycles of loading. During testing, it was often observed that the signal from the TDR would reveal cracks in the column face before the cracks were observed by visual inspection. At the stroke specified in Table 2, the crack pattern on all columns and the corresponding TDR signal waveform (difference from the baseline prior to loading) are presented in Figure 19. It is clearly seen from Figure 19 that all cracks have been successfully identified with the measured signal. The data shown for Columns C1-C4 are at a table stroke level of 0.178 cm, and the data for Column C5 was recorded at a stroke level of 0.076 cm. The decreasing levels represent data taken at the frequency shown in the legend in Hz. The reflection coefficient changes with the excitation frequency, representing the dynamic effect on the column behavior. In Columns C3-C5, FRP wrapping was applied to the lower 61 cm (24 in.) of the column. The sensors were installed before the FRP was wrapped around the columns so that the ability of the sensors to detect cracks beneath such retrofit options, which would normally conceal cracks, could also be investigated. In Columns C3 and C4, fibers were oriented horizontally so that the cracks that had occurred beneath the FRP would separate the FRP sheets in the weak direction of the fibers and could therefore be seen at the surface of the FRP sheets. The sensors accurately detected the location of these cracks beneath the wrapping. In Column C5, the cracks beneath the FRP could not be physically seen because two FRP sheets had been applied with horizontally- and vertically-oriented fibers, respectively. However, Sensor T5 in that specimen did show that there

were cracks across the face of the column in the retrofitted region, as indicated in Figure 19 for Column C5. It is clearly seen from Figure 19 that for all excitation frequencies the location of the peaks in the signal correlates well with the respective physical location of the cracks.

Table 2 Test matrix of column specimens.

Column	Retrofit	Stroke (mm)	Rubber-Sensor	Teflon-Sensor	Crack
C1	No	1.78	N/A	T1	Surface
C2	No	1.78	N/A	T2	Surface
C3	Yes	1.78	N/A	T3	Hidden
C4	Yes	1.78	N/A	T4	Hidden
C5	Yes	0.76	N/A	T5	Hidden
C6	No	0.76	R1	N/A	Surface

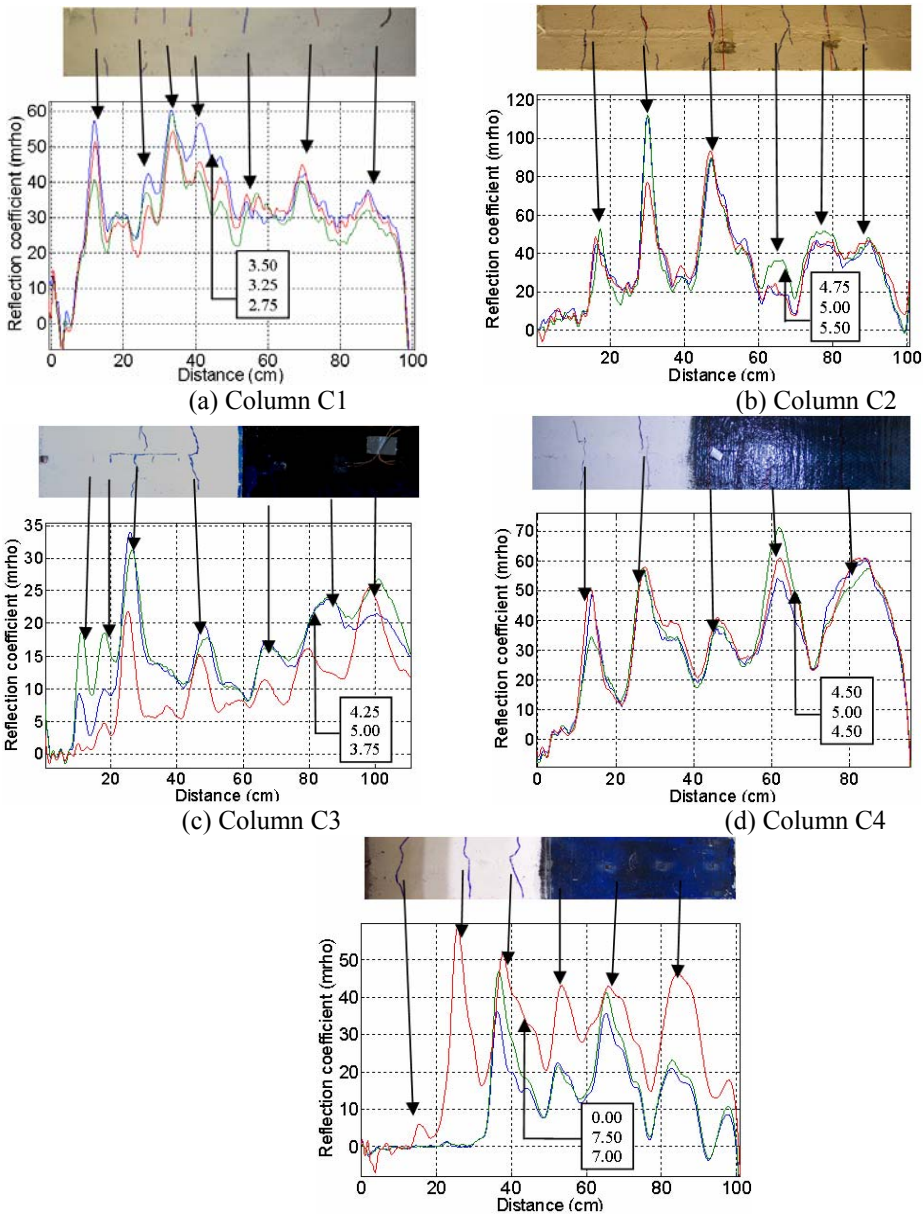

(a) Column C1

(b) Column C2

(c) Column C3

(d) Column C4

(e) Column C5

Figure 19 Differenced signals taken at given excitation frequencies in Hz.

Teflon Versus Rubber Sensors

To understand the performance of rubber sensors under dynamic loading, one such sensor was installed in Column C6, as indicated in Table 2. At an excitation frequency of 5.00 Hz, 5.25 Hz, 5.50 Hz, and 7 Hz, respectively, the reflected signal from the rubber sensor is shown in Figure 20 at a stroke of 0.762 mm (0.03 in.). In comparison with Figure 19, Figure 20 indicates that the reflected signal from the rubber sensor is considerably smaller in responding to the occurrence of cracking. This is due in part to the rubber material likely delaying its response to the rapidly cracking effect because of the material viscosity under dynamic loading. Therefore, the rubber sensors are more applicable to slowly developed cracks or strain measurements, as discussed in Chen et al. (2004).

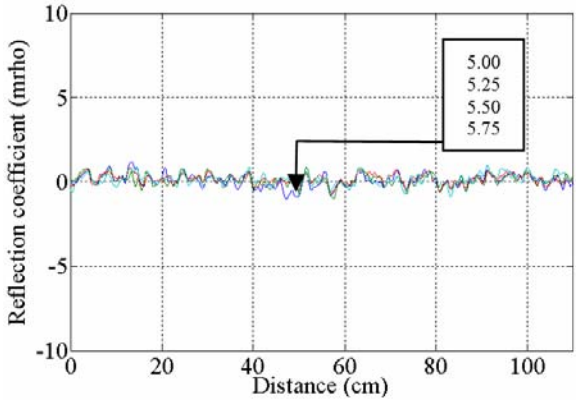

Figure 20 Differenced signal from rubber sensor R1 at given frequencies in Hz.

Sensor Fatigue

An issue that needed to be addressed with these new sensors is their fatigue life. During the shake table tests, it has been observed that all sensors continued to be functional until the failure of tested columns (fracture of main reinforcement) after over 20,000 cycles of motion. The only unexpected situation was with a loose connector at the end of Sensor T1 as a result of bending back and forth repeatedly during testing, but this connector was easily repaired. In the event that a sensor might be damaged, it is relatively simple to cut the sensor from the groove, and replace and regrout a new sensor in its place without disturbing the structure itself. This is possible since the sensor is embedded into the face of the concrete usually no deeper than 1.27 cm (½ in.).

Discovery of Memory Feature

One of the more interesting discoveries after the dynamic column tests, was the observation of the sensor being able to "remember" where the cracks had occurred after testing was completed. While it was visually difficult to detect the cracks on the face of the column, the peaks in the signal from the sensor corresponding to cracking remained visible in the signal once testing was completed. This can be very useful in post-disaster evaluation of RC structural members by being able to more accurately and quickly ascertain the damage that occurred to the structure during the event. Figure 21 shows the signal from Columns C4 and C5 captured after testing was completed. It can be seen from Figure 21 that the cracks that had opened during motion are still visible in the sensor signal.

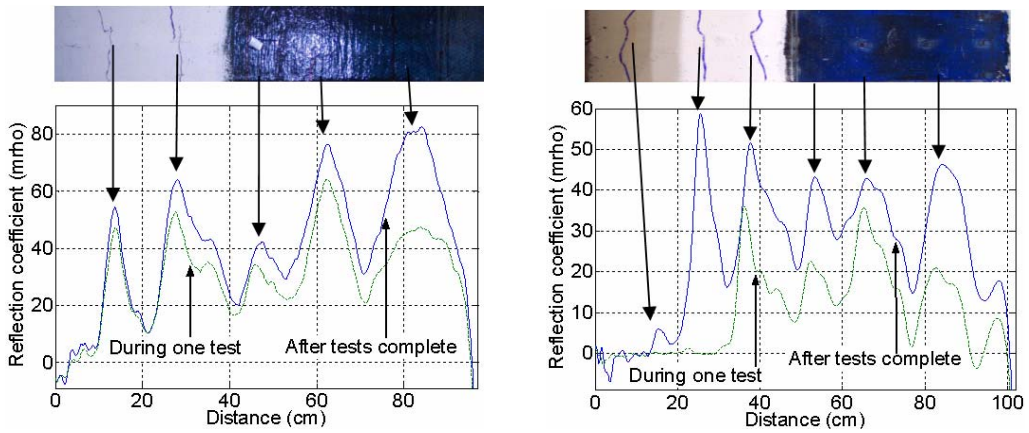

(a) Column C4 (b) Column C5

Figure 21 Difference data captured during testing and memorized after tests.

As will be discussed in the following section, the observed feature above is actually a result of the occurrence of the permanent displacement or misalignment on the sensor. For lack of a better term, it is referred to as a "memory" feature in the remaining presentation. The memory feature will enable the sensors to be implemented either with or without a network for earthquake damage assessment. If a network is used, then it would be possible to acquire real-time data from the crack sensors. It is also possible to implement the sensors without a network, since data reflecting the important part of the crack history close to the maximum crack width can be obtained from the sensor after an event has occurred. This is significant because it allows for useful data to be obtained in the event that data acquisition equipment either loses power or is damaged. This memory feature was investigated more closely and is discussed in the next section of this study.

Statically and Cyclically Loaded Beams for Memory Feature Characterization

With the discovery of the memory feature, a new test protocol was developed to understand when the memory feature appears. The memory feature is related to the sliding mechanism of spirals over the dielectric of a Teflon sensor. When the crack opens, the spirals are separated locally, and when the crack closes again, the spirals can be misaligned which will continue to reveal a discontinuity in the signal. A schematic representation of the misalignment is shown in Figure 22. From this figure, one can see that the edges of the spirals are no longer in contact with one another after they have been pulled apart. Therefore the width of a crack, the rate of loading, and the number of times that the crack opened and closed are considered possible parameters contributing to the permanent deformation of the outer conductor of the sensor at the location of a crack.

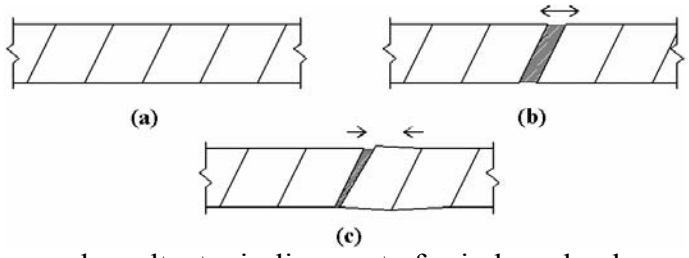

Figure 22 Separation and resultant misalignment of spirals under dynamic loading.

Test Procedure

The test matrix of beam specimens is given in Table 3. For the static loading case, the beam was loaded in incrementally increasing levels so that as cracks appeared, their width could be physically measured at each loading level to compare with the reflected signal from the sensor. The loading was displacement controlled with the Tinius Olsen machine so that the width of the cracks remained as constant as possible while measuring was taking place. As the cracks started to propagate, their width was measured with a crack scope with a resolution of 0.025 mm (0.001 in.) and a maximum measurable width of 3 mm (0.12 in.). The loading displacement level was measured at the mid-span of the beam and was typically increased in steps of 0.5 mm (0.02 in.). However, in some cases when it was observed that the signal from the sensor at the location of a crack was changing rapidly, that interval was decreased to 0.25 mm (0.01 in.) so that the progressive opening of the cracks could be captured in better detail with additional data points. The load deflection was increased until the beam was near the point of yielding based on the change in slope of the load-displacement curve.

Table 3 Test matrix of beam specimens.

Beam	Type	Sensor	Effect studied
B1	I	T6	No. of cycle
B2	I	T7	Crack width/No. of cycle
B3	II	T8	Crack width/No. of cycle
B4	II	T9	No. of cycle
B5	I	T10	Load rate
B6	II	T11	Load rate

For cyclic tests with the Tinius Olsen machine, a constant deflection was repeated throughout an increasing number of cycles. Each beam was loaded to a maximum deflection of 80% of its maximum deflection from the static tests. The deflection value was chosen so that the cracks would open significantly yet preventing the beams from yielding or failing. The load was applied and then released at a rate of 0.762 mm/sec (0.03 in./sec) which was limited by the loading machine. Data was recorded from the sensor at peak displacement and then again after each set of cycles was completed, at no load, to capture the memory phenomenon. The beams were tested until very little or no change was observed in the reflected signal from the TDR at each crack location in the unloaded condition.

To see the effect of a higher loading rate on memory feature, two additional beams (B5 and B6 in Table 3) were cyclically tested. In these cases, a small groove, 3.2 mm in depth (0.125 in.), was cut in the bottom center of the beams to control the location of the largest crack. Both beams were first loaded statically with the Tinius Olsen machine until the first crack was discernable in the signal and visible by sight. Beam B5 and Beam B6 were subjected to a mid-span deflection of 2.54 mm (0.1 in.) and 3.81 mm (0.15 in.), respectively, due to their difference in reinforcement. Once the data from this setup was recorded, the specimens were placed in the MTS880 loading machine and loaded with half-sine motion at a frequency of 1 Hz, or 7.62 mm/sec (0.3 in./sec), in 5 cycle increments. At the end of each 5-cycle set, data was recorded from the crack sensors at zero loading.

Crack Width Versus Reflection Coefficient

Figure 23 shows the reflected waveform at different loading levels that are represented by the mid-span deflections, and the crack pattern corresponding to the largest static load for Beams B1-B4. In the figure, the start and end of the sensor is illustrated by dotted lines on the column face. It was observed from Figure 23 that the smallest detectable crack according to the data recorded from the crack sensors was typically around 0.15 mm (0.006 in.). This value of crack width is larger than that observed in the previous study (Chen et al., 2004), which is attributable to the application of soldering outside the steel spirals. Even so, this is still within the desired detectable range, 0.35–0.41 mm (0.014–0.016 in.), for structural applications (Nawy, 2003). Figure 23 also indicates that the location of most cracks can be clearly identified from the measured reflection coefficient. It is noted that some of the cracks shown on the side view of beams may not actually pass through the sensor installed at the bottom face of the beams. This may explain why a few cracks seem missing from the measured signals.

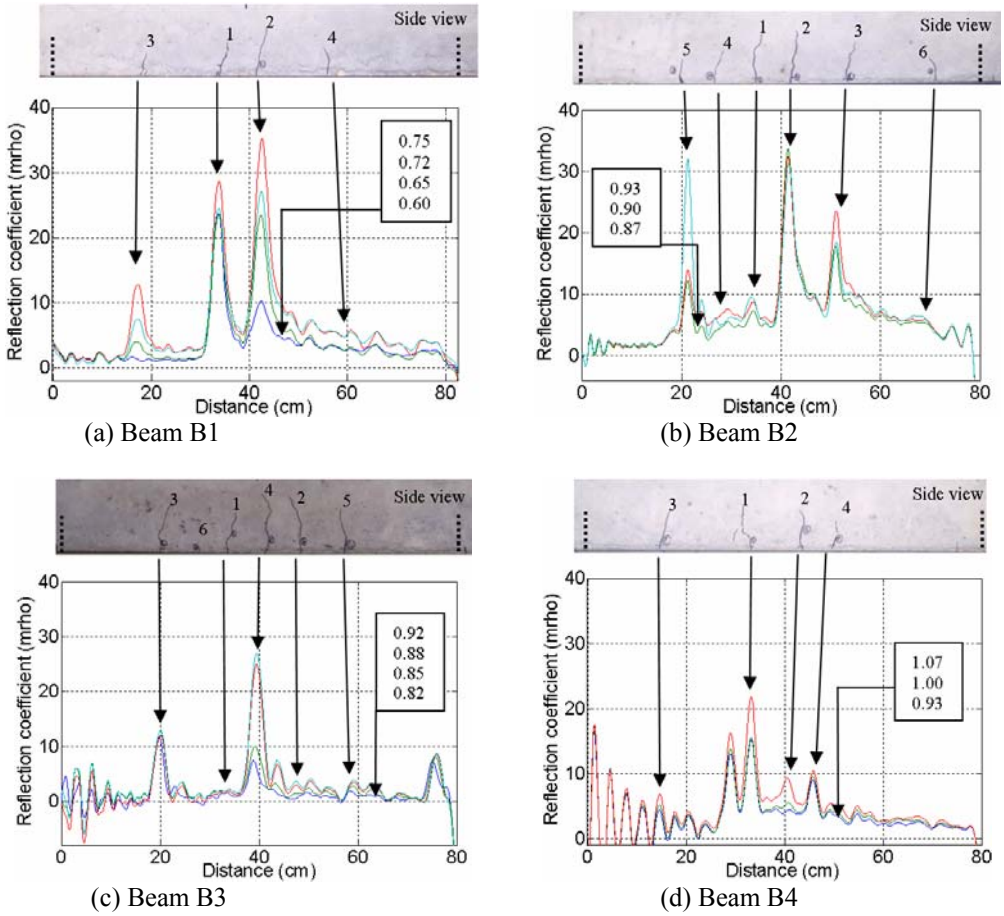

(a) Beam B1 (b) Beam B2

(c) Beam B3 (d) Beam B4

Figure 23 Difference waveforms at given mid-span deflections in % of span length.

An attempt was made to quantify the relationship between increase in crack width and increase in change of the reflected TDR signal from the sensor data. Figure 24 shows both the reflection coefficient and crack width of Beams B2 and B3 under various loading conditions that are represented by the mid-span deflection in terms of percentage (%) of the span length. The crack number shown in Figure 24 refers to Figure 23. In general, the results show an increase in

reflection coefficient as the crack width increases, especially at low loads. For each particular crack, the curves for the reflection coefficient and the crack width show an excellent trend for correlation. It is observed from Figure 24 that at a load level of approximately 0.70%, the crack width and the reflection coefficient corresponding to Crack #1 of Beam B2 drops steeply. This can be explained by the dramatic widening of the adjacent crack, Crack #2, at that loading level, resulting in stress redistribution of the beam. The curves corresponding to Crack #1 begin to increase again as the loading level increases. The presence of multiple cracks makes it difficult to establish a representative correlation between the reflection coefficient and the crack width. It is noted that, in Figure 23(d), several peaks were shown in the reflection waveform of Beam B4 between zero and approximately 15 cm (5.9 in.) due to loose contact of the end connection with TDR. This problem was identified during the testing and corrected before cyclic tests.

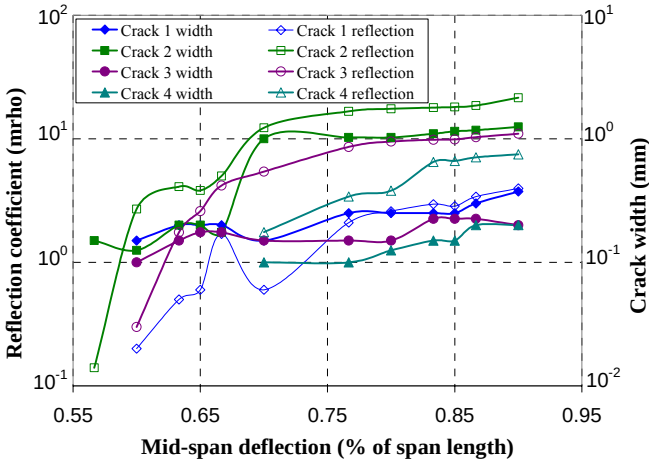

(a) Beam B2

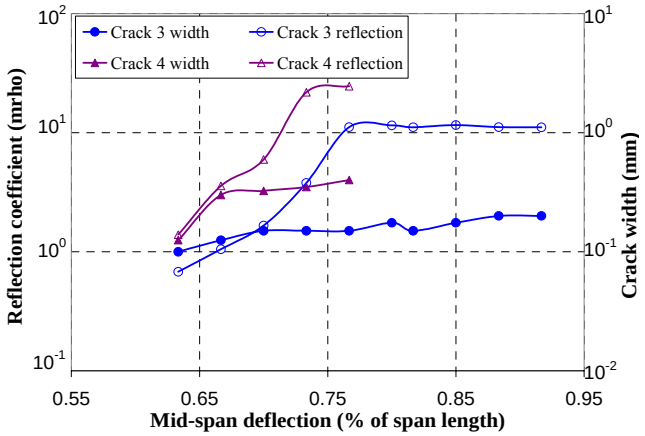

(b) Beam B3

Figure 24 Change in reflection coefficient at crack location and corresponding crack width versus mid-span deflection expressed in % of span length.

Effect of Crack Width on Memory Feature

At the end of static tests of Beams B2 and B3, the reflected waveform was acquired again after the loads applied on them had been removed. This time, only the largest cracks (> 0.25 mm)

could be seen in the signal, as shown in Figure 25. This indicates that crack width is an important parameter affecting the memory feature. Even if a large crack opens only one time, the crack-induced separation of the spirals of the sensor outer conductor could be so large that misalignment of the spirals is likely to occur when the crack closes. As illustrated in Figure 1, this misalignment will cause a discontinuity in the current flow through the outer conductor of the sensor resulting in a permanent change in the reflected signal at that location. However, if the crack is small when it is opened, the spirals of the sensor outer conductor can return to their original configuration allowing for the current path to be undisturbed and no discontinuity to be seen in the signal. It is noted that Figure 25(b) indicates some fluctuation of the reflected signal within approximately 15 cm due to loose contact of the end connection with the TDR device. This was found and tightened immediately after that test.

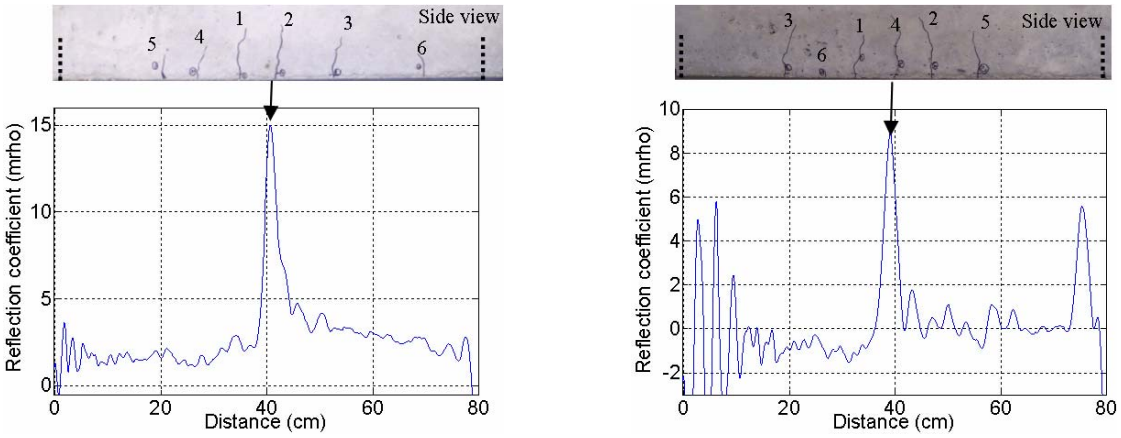

(a) Beam B2 (b) Beam B3

Figure 25 Difference signal taken at zero load after static tests were completed.

Effect of the Number of Loading Cyclic on Memory Feature

Even though a crack is relatively small, when the spirals are separated a number of times due to opening and closing of the crack, some fatiguing of the spiral material likely takes place, and because of permanent deformation, the spirals will again remain misaligned creating a discontinuity in the sensor. As shown in Figure 25, the largest crack in Beams B2 and B3 remained in memory after only one cycle of loading. In each case, the rest of the cracks remained visible in the signal at no load after no more than 15 cycles, as shown in Figure 26. The location of the sensor is shown in dotted lines in Figure 26. As the number of cycles increased, the peaks corresponding to each crack grew in magnitude of reflection coefficient. However, typically by 160 cycles, the peaks had stabilized. These observations confirm that the smaller cracks do in fact remain detectable in the signal at no load after a very low number of cycles. It can be seen from Figure 26 that the crack pattern in each beam was consistent. In each instance, the cracks near the center of the beam were the largest in width. The cracks that opened away from the center were smaller in magnitude. It can be seen that as the number of cycles increase, the magnitude of the disturbances in the reflected wave become larger. This figure also shows the excellent correlation of the location of major cracks along the beams.

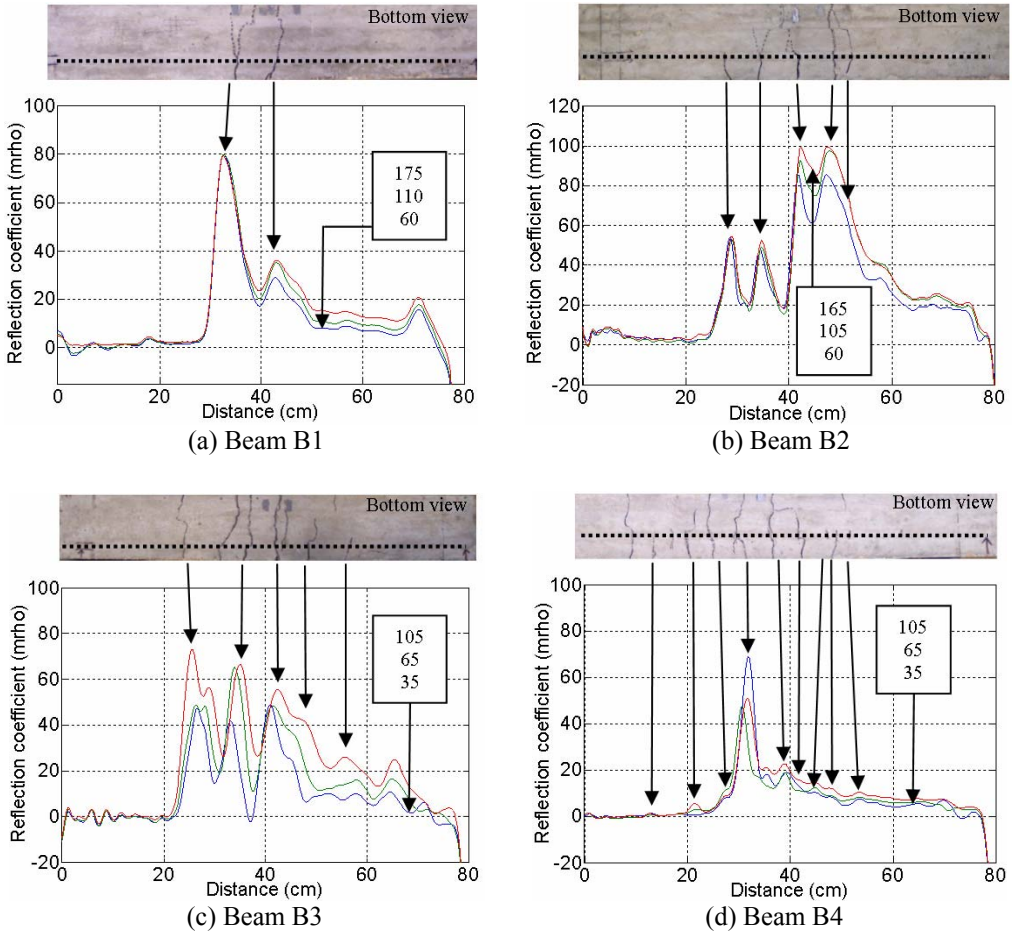

Figure 26 Difference waveform at zero load after given number of cycles (legend).

While the majority of the cracks are apparent in the signal from the sensor at zero loading, some of the smallest cracks do not show up even after several cycles. Therefore, it is important in practical applications to implement a method of data acquisition that will capture a time-history of crack data. This will further improve the performance of the crack sensor system enabling the detection of all cracks that are sufficiently large to have structural implications.

Effect of Loading Rate on Memory Feature

The results from the cyclic tests of Beams B5 and B6 are presented in Figure 27. They are consistent with those from the cyclic tests of Beams B1-B4 under slower loading in that the number of cycles required to invoke the memory of the sensor were in the same order. Within the first five cycles of loading the largest crack was visible in the signal at zero loading. More cracks propagated within the first five cycles as well. The width of those cracks was not able to be physically measured with the crack scope due to the test setup. However, they were smaller in size than the initial crack in both cases, and were similar in size and in pattern to the cracks in Beams B1-B4. The smaller cracks from the previous tests began to remain in the signal at zero loading within 15 cycles. Figure 27 shows how the cracks became increasingly visible as the number of cycles increased. It can also be seen from the photographs that, once again, location of the cracks are easily determined from the crack sensor signal.

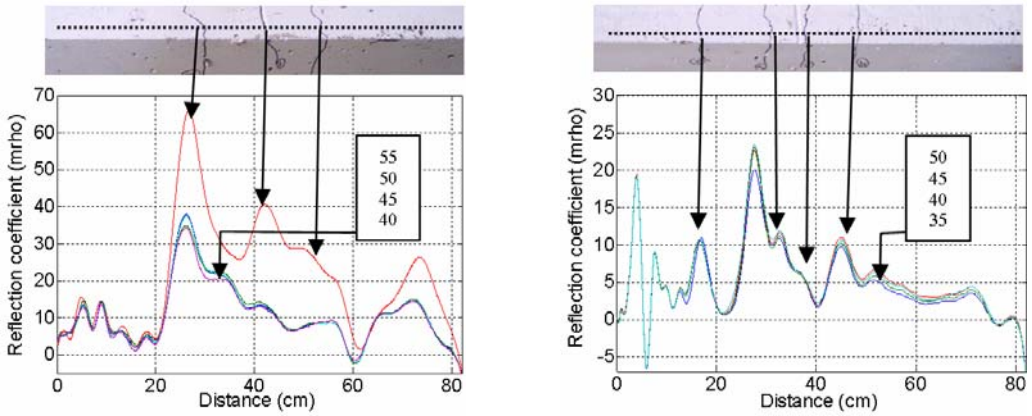

(a) Beam B5 (b) Beam B6

Figure 27 Difference waveform at zero load after given number of cycles.

Cyclically Loaded Beam-Columns as Test Bed of Cable Sensor Application

With small-scale RC beams and columns, the distributed cable sensors proved to be very effective in locating cracks and measuring their width. Their performance is further verified in this section with the large-scale beam-column specimens, especially with the presence of a 90º bend at the beam-column joint.

Specimen #1

A rubber sensor was installed on the first beam-column assemblage, Specimen #1. Under tension loading, the difference waveforms measured from a crack sensor are presented in Figure 28, corresponding to a load of 80 kN (18 kips), 173 kN (39 kips), 300 kN (68 kips), 1.98 cm (0.78 in.), and 2.97 cm (1.17 in.). The crack numbers in Figure 28 correspond to the crack pattern illustrated in Figure 29(a, b), at 177.3 kN (38.85 kips) and 1.98 cm (0.78 in.), respectively.

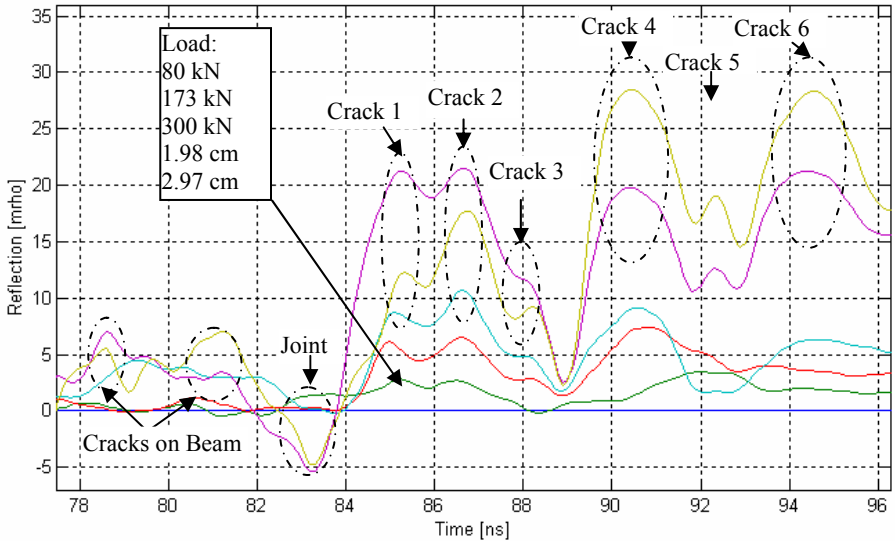

Figure 28 Difference waveform under tension.

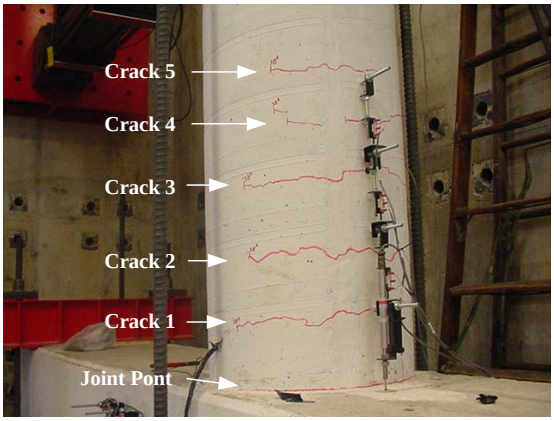

(a) Crack pattern at 173 kN

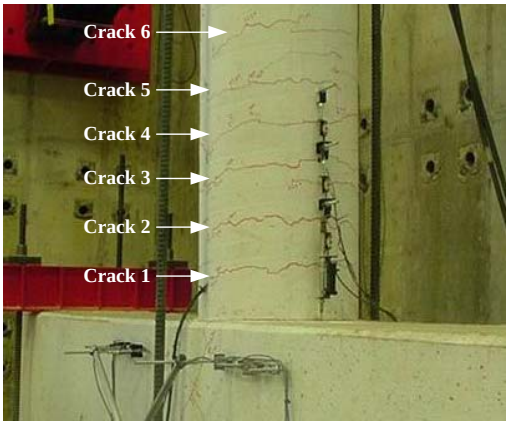

(b) Crack pattern at 1.98 cm

Figure 29 Crack pattern at 173 kN and 1.98 cm in tension.

By comparing Figure 28 and 8.29, it can be seen that the measured waveforms match well with their corresponding crack patterns; the sensor has been successful in detecting cracks in the large-scale beam-column assemblage. It is also observed that the change in reflection waveform follows the development of the cracks. For example, at the load of 86.43 kN (19.43 kips), no noticeable crack was identified by visual inspection; the corresponding waveform changes slowly except for subtle peaks corresponding to Crack #1 and #2. When 177.3 kN (38.85 kips) and 259.2 kN (58.28 kips) are applied on the assemblage, Crack #3 and #4 start appearing in the waveform, and Crack #1 and #2 become very obvious. By the time that the specimen is subjected to a displacement of 1.98 cm (0.78 in.) and 2.97 cm (1.17 in.), all cracks can be clearly identified from the measured signal.

Specimen #3

One Teflon sensor and one rubber sensor were installed on the specimen. The sensors were installed along the beam, bent at the construction joint and continued up the face of the column. To control the change in reflection at the joint, copper foil tape was wrapped around the sensor at the bend because the foil, when bent, reflects a much smaller disturbance when the sensor is bent.

The initial testing, which took place in December of 2003, involved no retrofit scheme. The beam-column was loaded at three loading levels, 86.43 kN (19.43 kips), 177.3 kN (38.85 kips), and 259.2 kN (58.28 kips). There was minor cracking on the face of the column which was detected by both sensors, as seen in Figure 30 and Figure 31. After retrofitting had been completed, the specimen was tested again in August of 2004. The same three loading levels were applied and the results are shown in Figure 30 and Figure 31. The magnitude of the reflection coefficient for most of the cracks is reduced during the second test, more likely as a result of the retrofit.

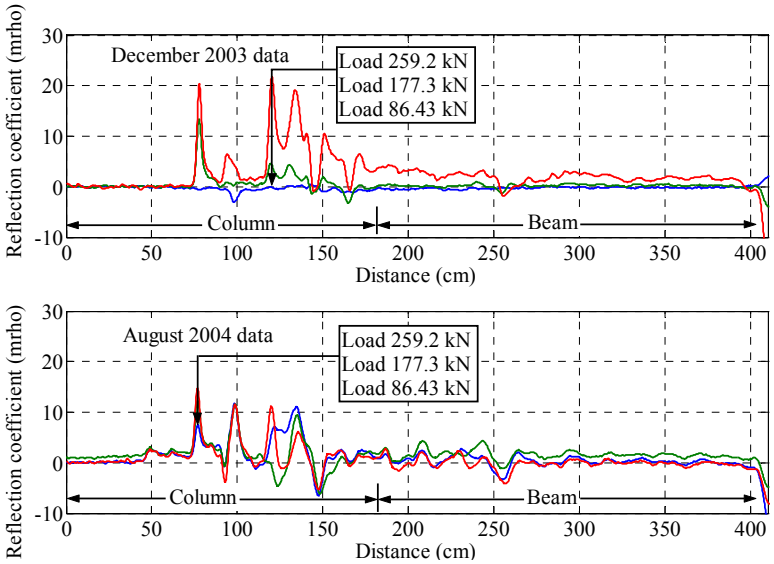

Figure 30 Differenced signals taken of the Teflon sensor.

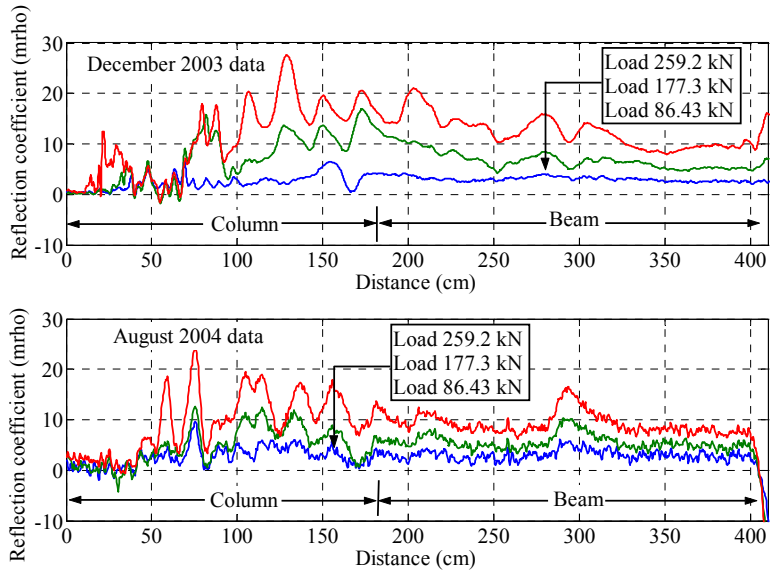

Figure 31 Differenced signals taken of the rubber sensor.

The higher levels of loading were done on a displacement-controlled basis to control the displacement ductility level of the column. During these higher levels, the reflection of the respective cracks grew in magnitude, as seen in Figure 32. As can also be seen in Figure 32, the Teflon sensor incurred damage at the construction joint, and the section of the data correlation to the beam can no longer be seen as of the loading displacement of 2.97 cm, cycle B. The rubber sensor does not show this. The cause of the damage can be seen in Figure 33 which shows the sensors at the location of the construction joint under load. The rubber sensor, whose dielectric is very flexible, was able to stretch and the outer conductor, never losing contact thus allowing the signal to be uninterrupted at the joint. However, as can be seen, the outer conductor of Teflon sensor had been damaged due to the frailty of the copper foil exposing the Teflon dielectric material. It should be noted that the cable itself did not break; only the copper foil was “scraped”

off by the excessive motion of the rough concrete against the sensor during cyclic testing. The sensors also revealed an increase in crack growth at successive cycles of the same load level, as seen in Figure 34. This progressive change in the sensor signals indicates the widening of the cracks after repeated cycles of loading.

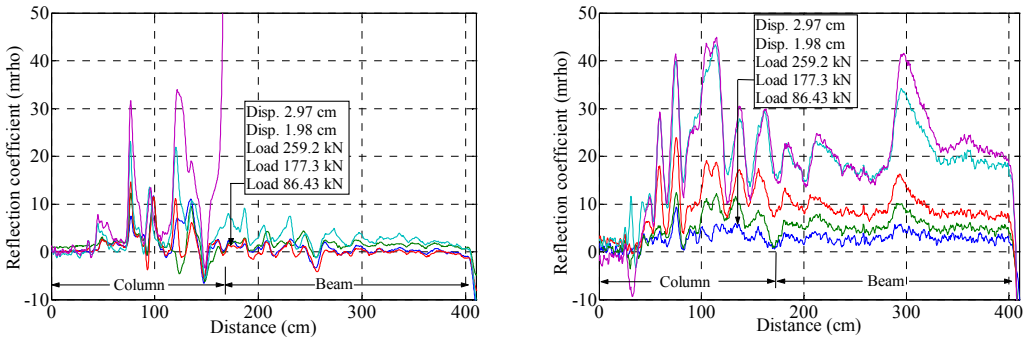

(a) Teflon sensor (b) Rubber sensor

Figure 32 Differenced signals taken at given load/displacement level.

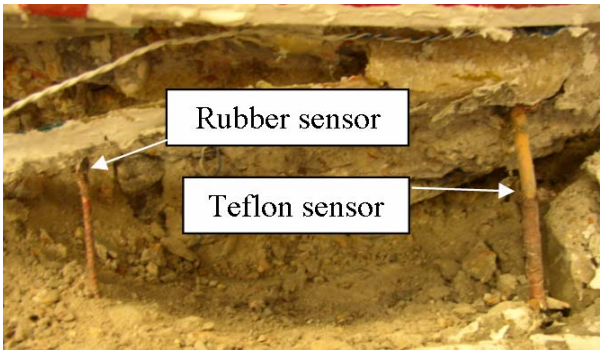

Figure 33 Photo of two sensors at the beam-column construction joint.

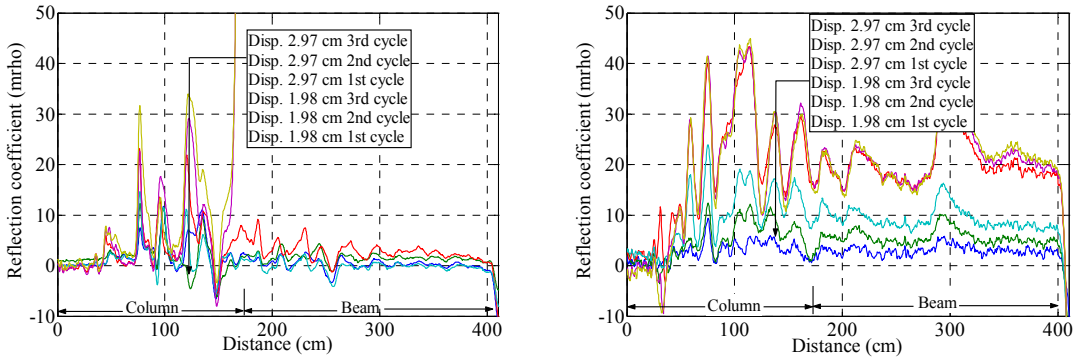

(a) Teflon sensor (b) Rubber sensor

Figure 34 Differenced signals taken at two displacement levels.

NEAR-FIELD MICROWAVE MEASUREMENTS

Test Specimens, Setup, and Procedure

Test Specimens

Several mortar and concrete cylindrical specimens, 102 mm (4 in.) in diameter and 203 mm (8 in.) in length, were cast for the detection of cracks with near-field microwave measurements. Each specimen had a 1 mm (0.039 in.) or 2 mm (0.078 in.) wide artificial crack that was created on its side face during construction. Both surface crack and interior crack were considered, as illustrated in Figure 35. The surface crack can be seen on the side surface of the specimen, while the interior crack, simulated with an embedded thin plastic sheet, extended to approximately 2–3 mm (0.078–0.117 in.) from the cylindrical surface to represent a crack that does not yet break to the surface.

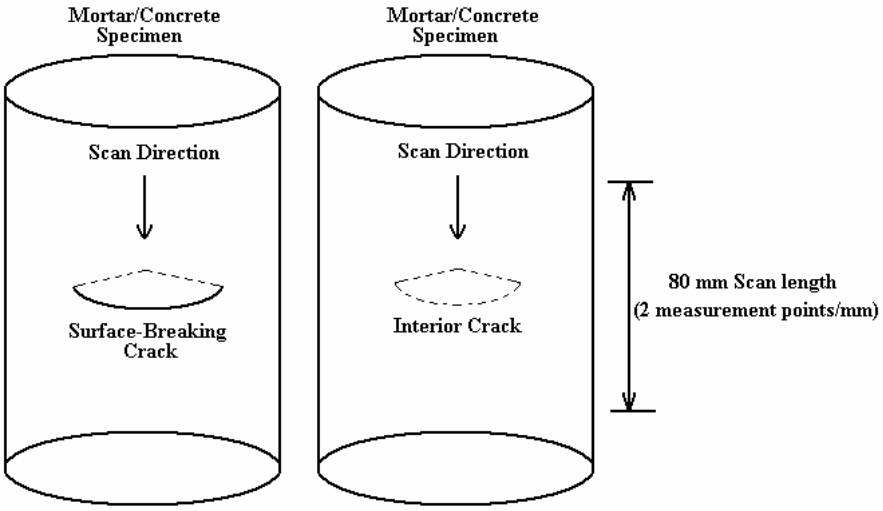

Figure 35 Test specimens.

Experimental Setup

Figure 36 shows the schematics of a laboratory designed microwave reflectometer that was used to scan each specimen. The key component of the reflectometer, an open-ended rectangular waveguide, is placed away from the specimen by a standoff or liftoff distance, which represents the physical space between the waveguide aperture and the surface of the specimen. The rectangular waveguide can be positioned either at an inclination angle to the surface of the specimen, as shown in Figure 36, or perpendicular to the specimen surface (0º incidence angle). A microwave oscillator sends a signal to the open-ended rectangular waveguide at a given frequency. The incident wave launched from the waveguide propagates through the air over the standoff distance and encounters the surface of the specimen. A portion of the incidence wave is reflected back to the waveguide and picked up at the waveguide aperture. The reflected wave, along with the incident wave, forms a standing wave inside the waveguide. The voltmeter reads a voltage proportional to the reflected signal existing at the location of a diode detector in the waveguide. This voltage is recorded as the waveguide scans along the length of the specimen.

The reflected signal depends on the local dielectric property of the material present in the vicinity of the open-ended rectangular waveguide. For an inhomogeneous mixture, such as mortar or concrete, the local dielectric property of the material varies depending on the composition of its constituents (i.e., sand and coarse aggregates) present at that location. Thus, in the presence of a defect such as a crack, the defect's orientation, dimensions, and composition directly affect the local dielectric property of the material. The variation in the reflected signal is influenced by the variation in the local dielectric property of the material. Crack characteristic signal is the detector voltage plotted as a function of scanning distance, obtained when a crack is scanned over a waveguide aperture (Huber et al., 1997a; Yeh, 1994a).

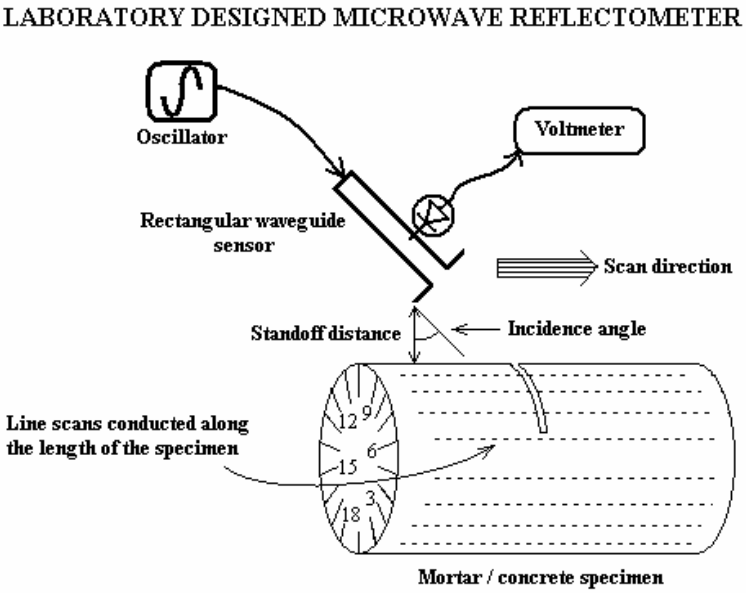

Figure 36 Experimental setup.

Testing Procedure

Each cylindrical specimen, as shown in Figure 35, was scanned for eighteen times over its side/circular surface with the open-ended rectangular waveguide sensor operated at 10.5 GHz. As illustrated in Figure 36, each line of scan started at one end of the specimen, along its length, and ended at its other end. After one line of scan, the specimen was turned approximately 20 degrees and scanned again. This process was repeated for eighteen times until the entire side surface of the specimen was covered. The eighteen scans were then plotted next to one another to produce a coarse two-dimensional (2-D) microwave image of the specimen as if the cylindrical surface had been unwrapped into a flat surface. The specimen was also scanned at several standoff distances.

Factors Influencing Crack Characteristic Signal

The degree by which these cracks can be detected depends on many factors including standoff distance, frequency, homogeneity (i.e., mortar versus concrete) of the specimen, incidence angle of the probe, crack opening dimension, and contrast between the dielectric properties of the crack (i.e., air) and the specimen (i.e., mortar or concrete) (Zoughi et al., 1996). Soaking the specimens

into water can increase this contrast. Indeed, in practice structural columns may be subject to moisture. Thus, in addition to the measurements mentioned above, the specimens were also soaked for about 24 hours and then similar scans were obtained right after their removal from a water bath, approximately two hours after removal from the bath (i.e., some of the water evaporating), and one day later.

Moisture and Water

A representative set of results is included in this report. Figure 37 shows the microwave images of the mortar specimen with a 1 mm (0.039 in.) wide surface breaking crack at a standoff distance of 3 mm (0.117 in.). The results clearly show the presence of the crack. They also show the expected improvement in the contrast when the specimen is moist.

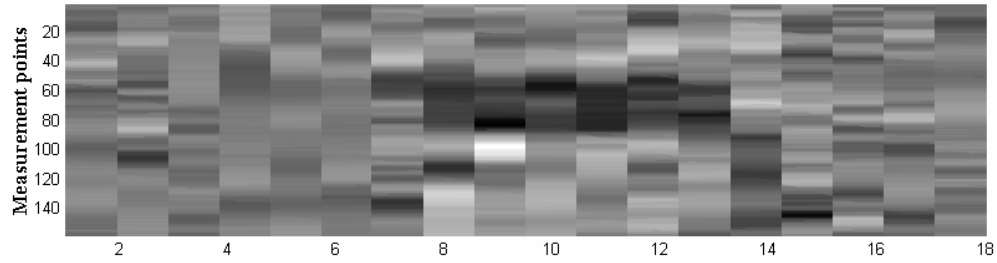

(a) Dry specimen

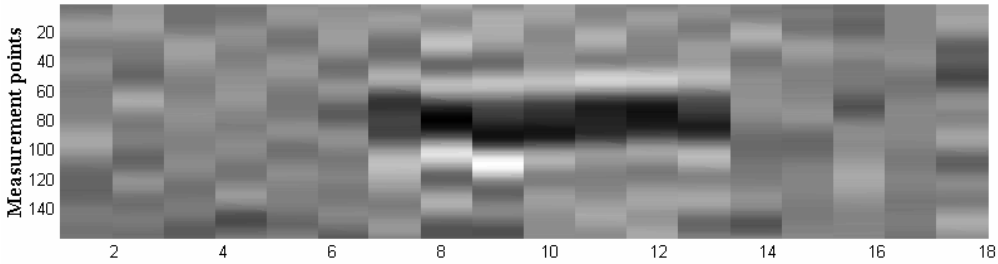

(b) Soaked specimen scanned just after removal from bath

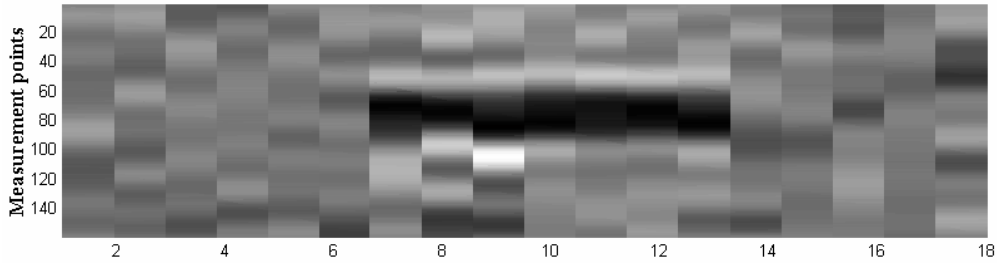

(c) Soaked specimen scanned approximately two hours after removal from bath

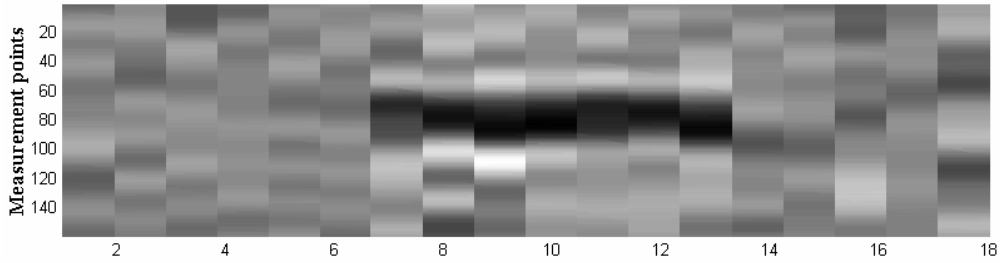

(d) Soaked specimen scanned one day after removal from bath

Figure 37 Results of the mortar specimen: 1 mm-wide surface breaking crack.

Similarly, the microwave images for the 2 mm (0.078 in.) wide surface breaking crack in mortar specimen were obtained at the same standoff distance. They are presented in Figure 38. As expected, this wider crack can be more easily detected from the images than the narrower one in the previous case, especially when the specimen is dry. Figure 39 is a reproduction of the results for the dry case in a cylindrical format, clearly indicating the location of the crack.

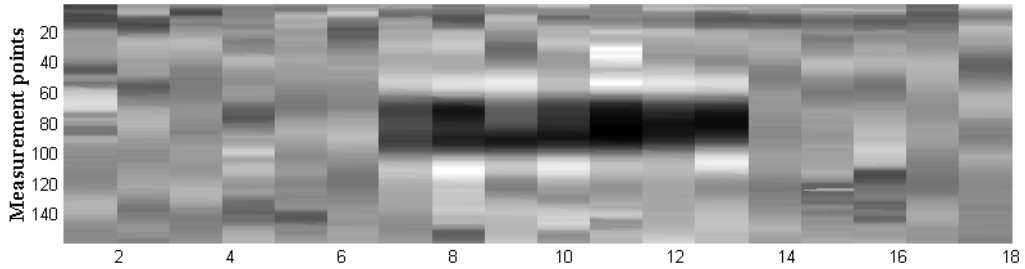

(a) Dry specimen

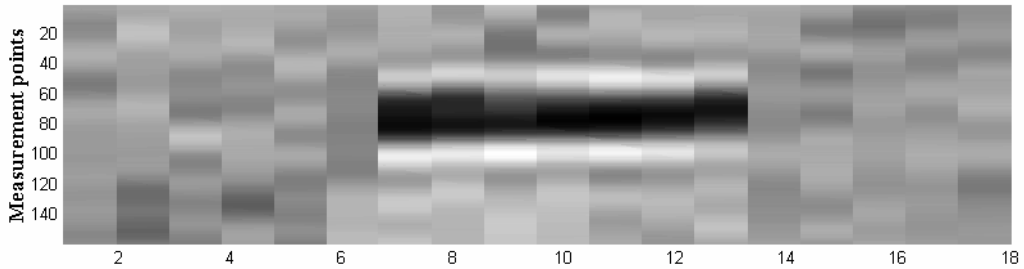

(b) Soaked specimen scanned just after removal from bath

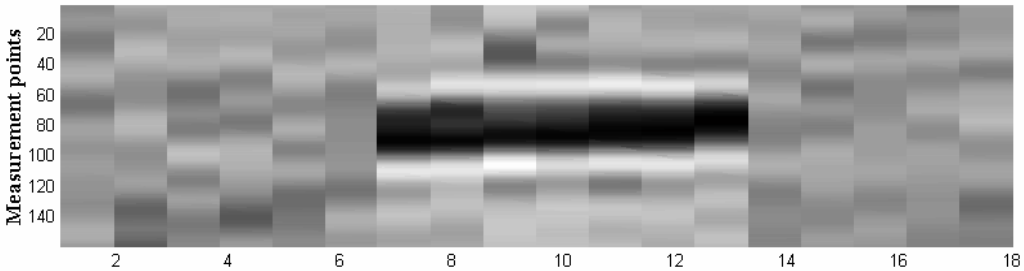

(c) Soaked specimen scanned approximately two hours after removal from bath

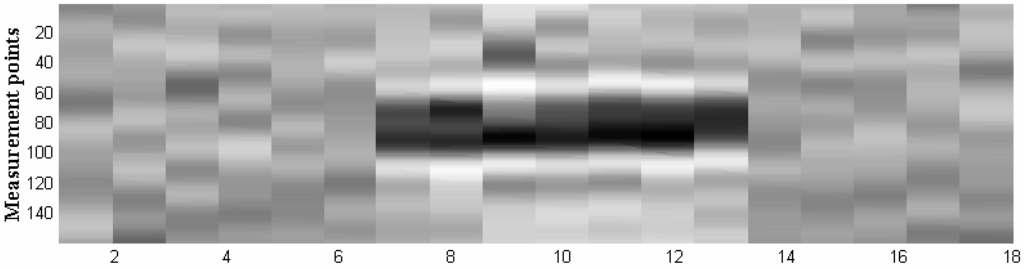

(d) Soaked specimen scanned one day after removal from bath

Figure 38 Results of the mortar specimen: 2 mm-wide surface crack.

Interior cracks are more difficult to detect. Figure 40 shows the images obtained from the specimen with a 2 mm (0.078 in.) wide simulated interior crack. The results do not indicate the presence of the crack as clearly as when it is surface breaking. This is primarily due to the lack of adequate microwave signal penetration into the specimen at 10.5 GHz. Results may be improved by lowering the frequency of operation and increasing the incident power level.

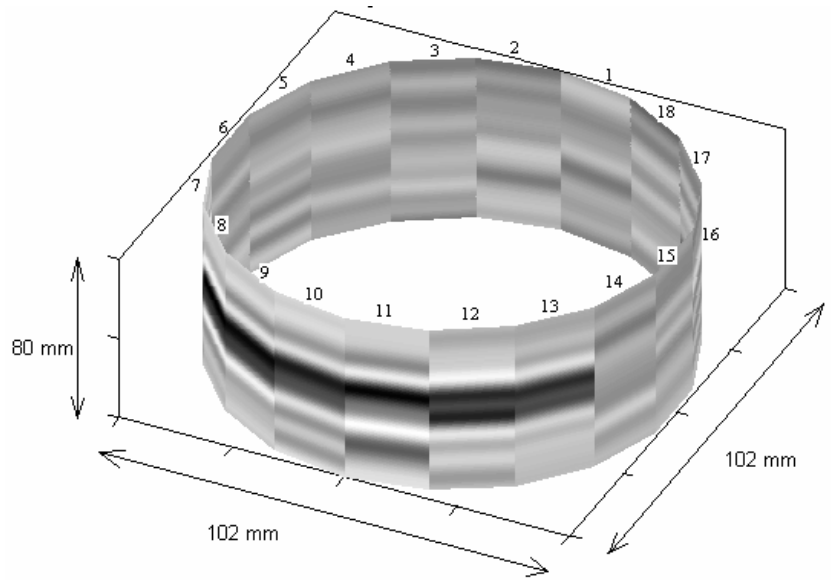

Figure 39 3-D images for dry specimen: 2 mm-wide surface crack, 3 mm standoff distance.

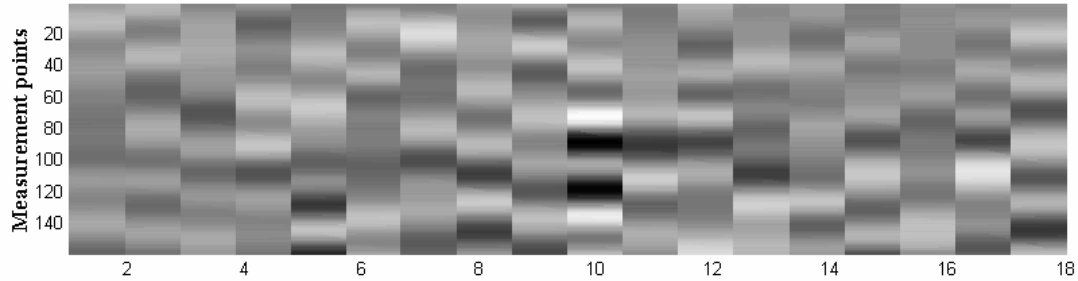

(a) Dry specimen

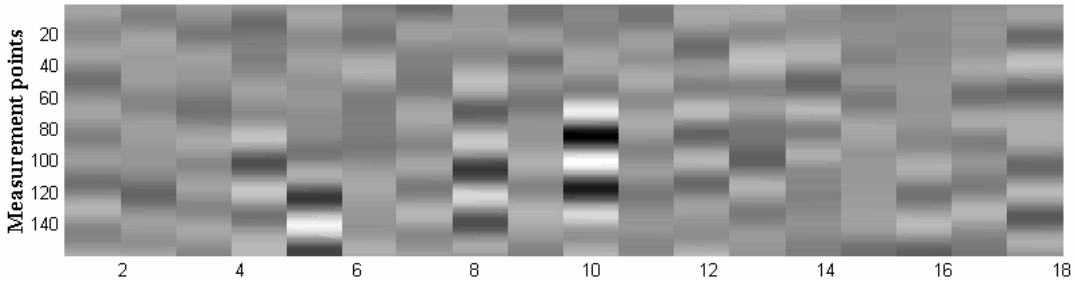

(b) Soaked specimen scanned just after removal from bath

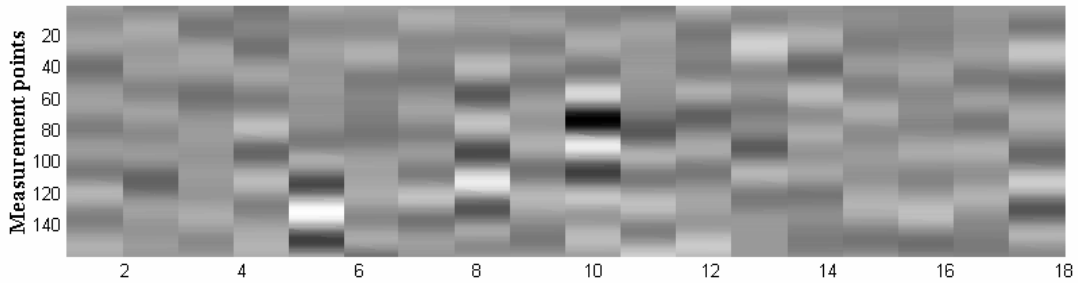

(c) Soaked specimen scanned approximately two hours after removal from bath

Figure 40 Results of the mortar specimen: 2 mm-wide interior crack.

Coarse Aggregates

In the presence of aggregates, the detection of cracks in a concrete specimen becomes more challenging. Figure 41 shows the results for the 1 mm (0.039 in.) wide surface breaking crack in concrete. The results clearly indicate the existence of the crack. However, due to presence of the aggregates, 6.35–12.7 mm (0.25–0.5 in.) in size, the images become less uniform and appear noisier. This is the direct result of the increased inhomogeneity associated with concrete materials in comparison with more uniform mortar specimens. Operating at lower frequencies not only allows for more signal penetration, but it also reduces the effective inhomogeneity of the specimen since the wavelength is longer at lower frequencies. However, operating at lower frequencies decreases the sensitivity to the presence of smaller cracks; i.e., the resolution degrades. In practical applications, a proper tradeoff must be made between the two effects.

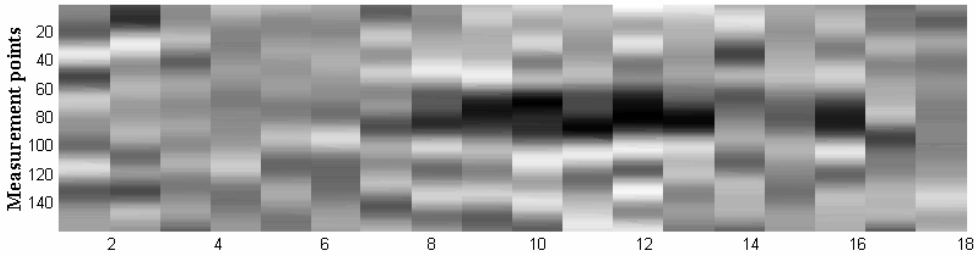

(a) Dry specimen

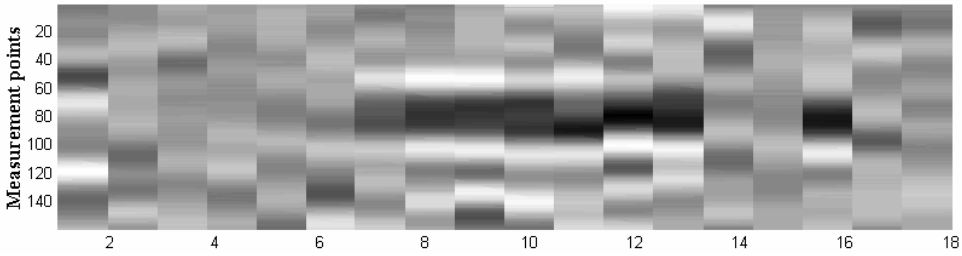

(b) Soaked specimen scanned just after removal from bath

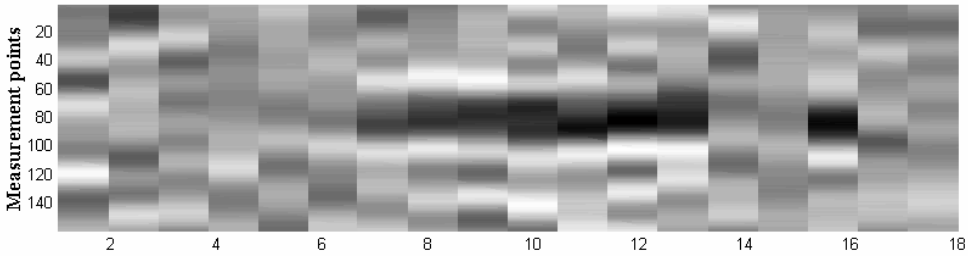

(c) Soaked specimen scanned approximately two hours after removal from bath

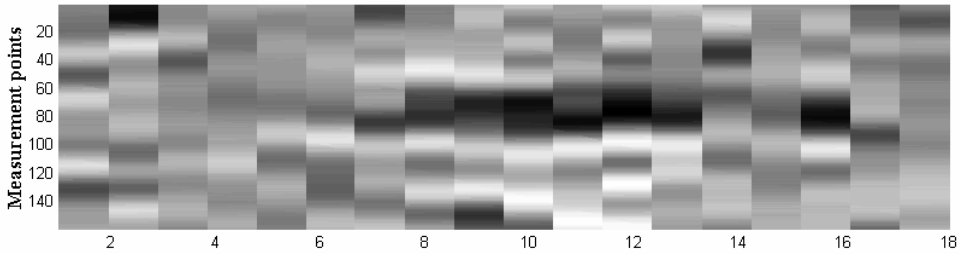

(d) Soaked specimen scanned one day after removal from bath

Figure 41 Results of the concrete specimen: 1 mm-wide surface crack.

Incidence Angle

Figure 42 shows the scan results of a concrete specimen with an interior crack at different incidence angles. Positioning the open-ended rectangular waveguide at an inclination to the specimen lengthens the crack characteristic signal as the waveguide sees the crack over a period of time so that the crack virtually becomes "wider" (Huber et al., 1997b). This increases the crack detection sensitivity as the likelihood of detecting a signal which exists for a longer duration is greater than the likelihood of detecting a signal which exists for a shorter duration. However, when operating at larger incidence angles, for instance 40º, the waveguide begins to see the surroundings as well, and thus making the results less sensitive to local variations in the material. This decreases the crack detection sensitivity as the level of crack characteristic signal decreases. Therefore, an optimum incidence angle has to be determined.

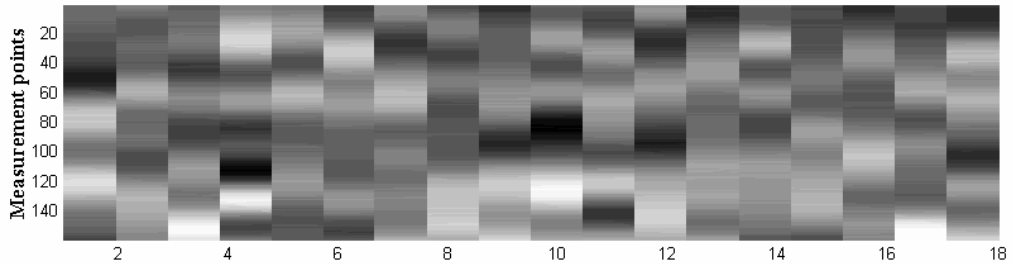

(a) Angle = 0º and distance = 10.0 mm

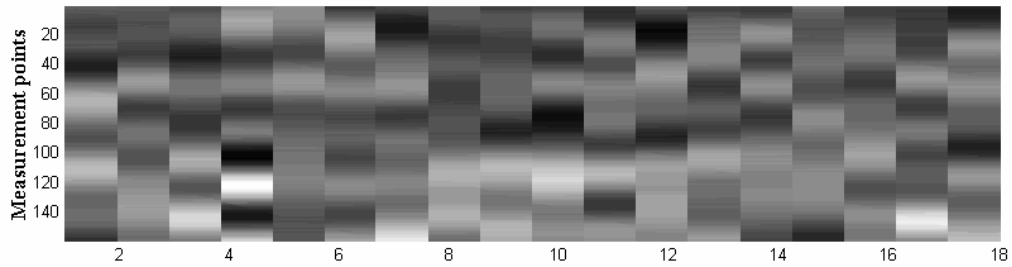

(b) Angle = 20º and distance = 4.5 mm

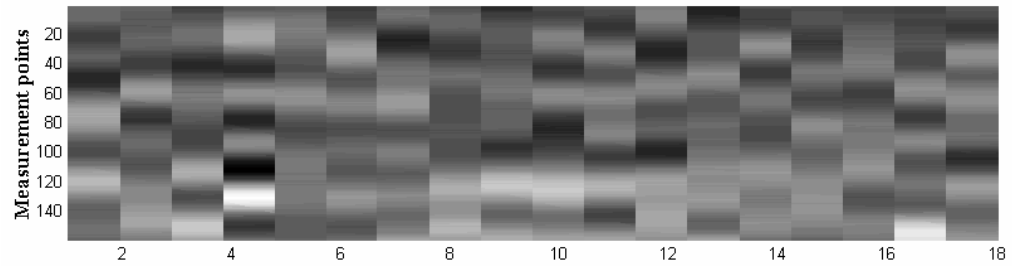

(c) Angle = 30º and distance = 2.0 mm

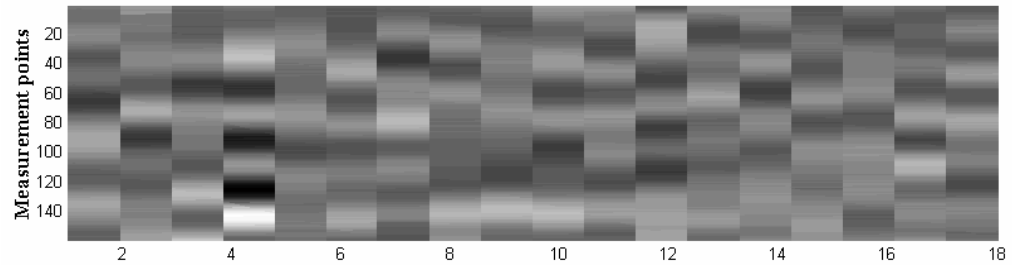

(d) Angle = 40º and distance = 0.5–1.0 mm

Figure 42 Images at various incidence angles and standoff distances:1–2 mm interior crack.

The images in Figure 42 do not clearly show the crack pattern. They were therefore processed by placing a threshold level on the gray scale intensity in the image. Figure 43 shows the processed images of those obtained by scanning the concrete specimen at 30º incidence angle. The crack pattern can be easily identified in the processed image, as marked with a box.

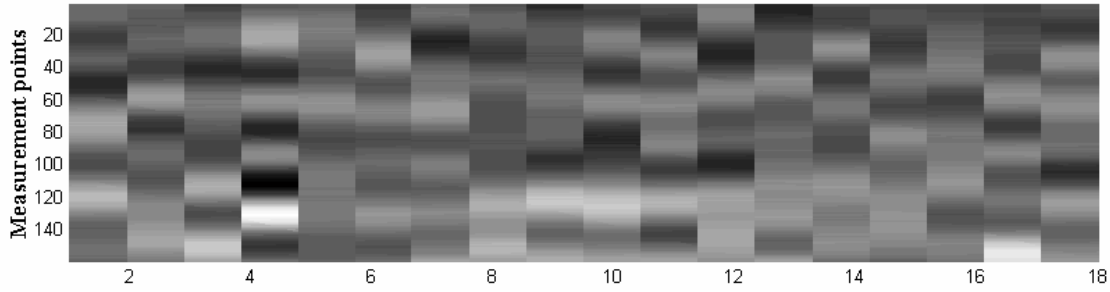

(a) Original image

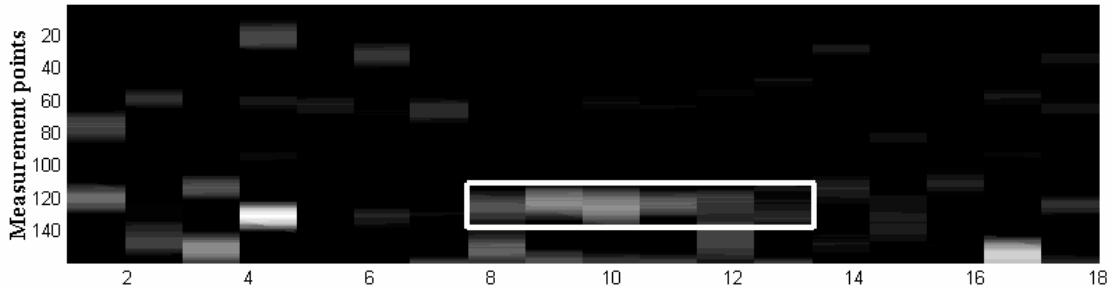

(b) Processed image

Figure 43 Effect of image processing: concrete specimen with 1–2 mm wide interior crack at 30º incidence angle.

Frequency of Operation

To study the influence of operating frequency on the detection of cracks, measurements were conducted at 10.5 GHz (X-band) and 7.5 GHz (J-band), respectively. The aperture dimension of the rectangular waveguide becomes larger at lower frequencies (J-band); hence, specimens with larger dimensions, 152 mm (6 in.) in diameter and 305 mm (12 in.) in length, were used for this investigation. These specimens included a 1 mm (0.039 in.) thick plastic sheet embedded at a depth of approximately 15 mm (0.585 in.) from the side/circular surface. The images from scanning the large concrete specimen at 10.5 GHz (X-band) are presented in Figure 44. They do not show the crack pattern because of inadequate penetration of microwave signals at 10.5 GHz.

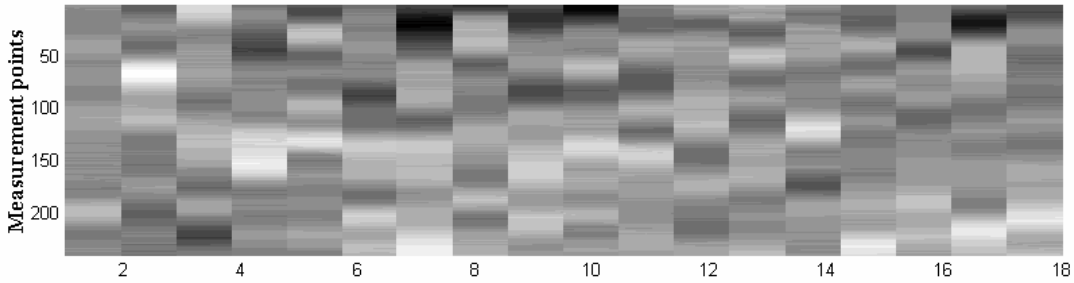

(a) Angle = 0º and distance = 8.5 mm

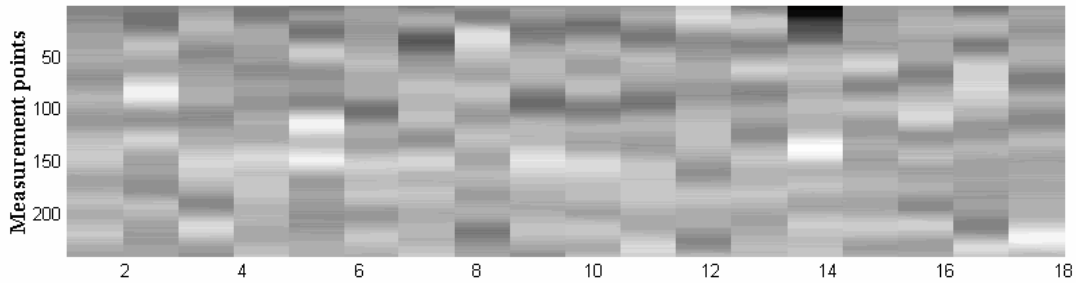

(b) Angle = 20º and distance = 4.0 mm

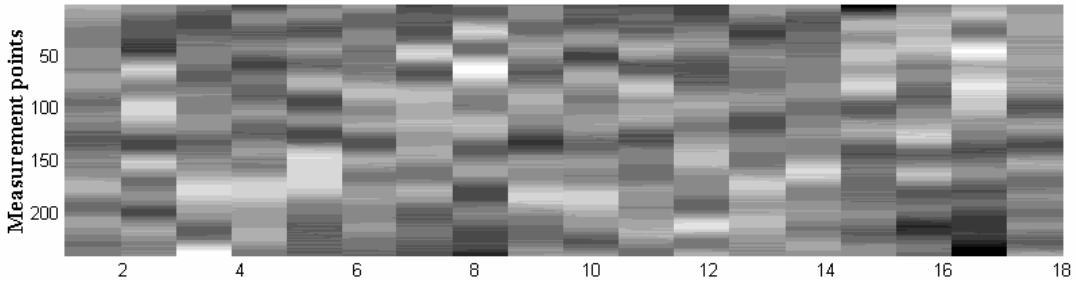

(c) Angle = 40º and distance = 0.5–1.0 mm

Figure 44 Images of concrete specimen (152 mm × 305 mm) at different incidence angles and distances: 1 mm-wide interior crack, operating frequency = 10.5 GHz (X-band).

To increase the penetration of signals, the same specimen as the one used for Figure 44 was scanned at 7.5 GHz (J-band). The results are presented in Figure 45. As expected, lowering the operation frequency increases the depth of penetration of microwave signals into the specimen, allowing for the detection of cracks at greater depths, as clearly illustrated in Figure 45(b), but decreasing the ability to detect small cracks (resolution). These images also tend to be smoother than the images obtained at X-band as the effective inhomogeneity of the concrete is reduced. It can be seen that a crack is detected at J-band with an incidence angle of 20º. Although the crack characteristic signal can be further lengthened at a 30º incidence angle, contrast in the intensity of the signal between the crack and the specimen is decreased. As mentioned earlier, the interior crack is no longer visually identifiable in the images obtained at higher incidence angles (approximately 40º).

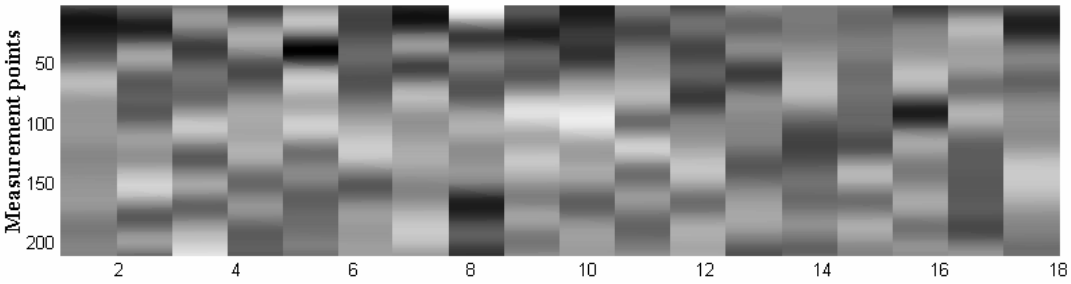

(a) Angle = 0º and distance = 6.5 mm

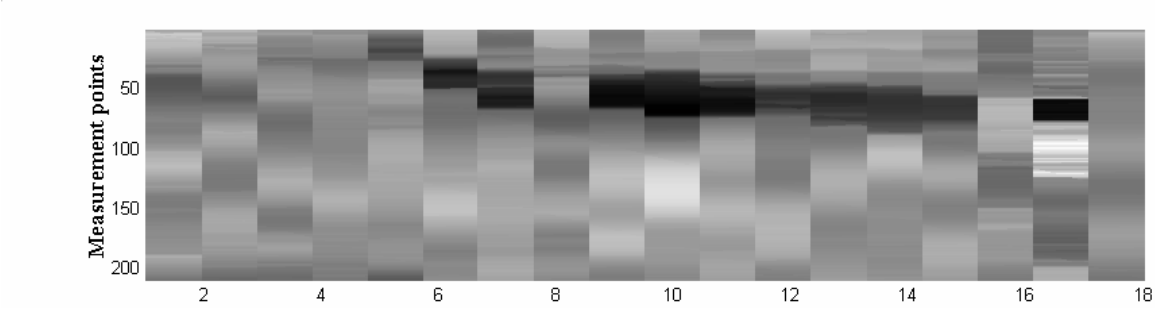

(b) Angle = 20º and distance = 3.5 mm

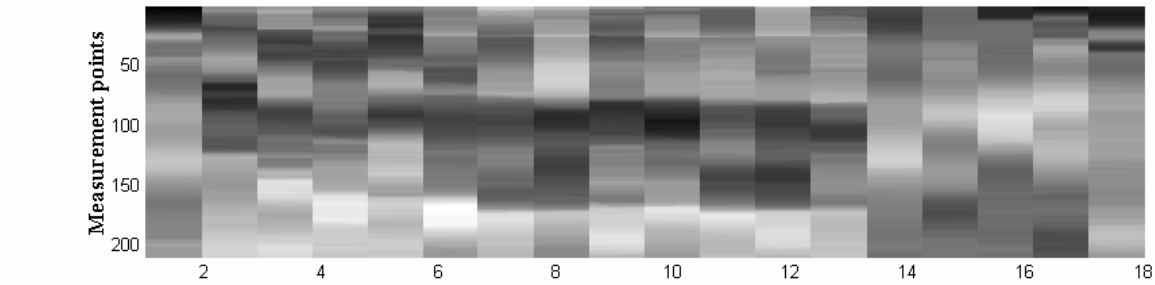

(c) Angle = 30º and distance = 1.0 mm

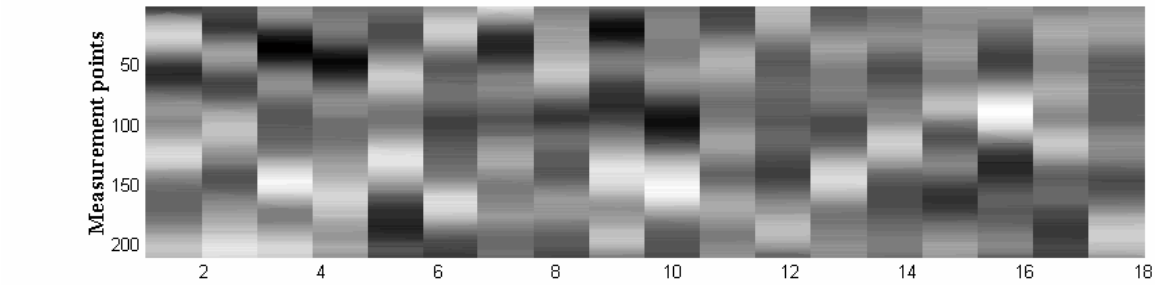

(d) Angle = 40º and distance = 1.0 mm

Figure 45 Images of concrete specimen (152 mm × 305 mm) at different incidence angles and standoff distances: 1 mm-wide interior crack, operating frequency = 7.5 GHz (J-band).

Cracks in Axially Loaded RC Cylinders

Test Specimens

In the previous section, experimentations were conducted on several mortar and concrete specimens with artificial/simulated cracks. The width of these simulated and interior cracks was about 1–2 mm (0.039–0.078 in.). This section extends the previous investigation into the detection of cracks that are induced by external loading.

Mortar and concrete cylindrical specimens were cast with two different sizes: 102 mm × 203 mm (4 in. × 8 in.) and 152 mm × 305 mm (6 in. × 12 in.) (diameter × length). Each 102 mm × 203 mm (4 in. × 8 in.) concrete specimen was reinforced with a 6.35 mm (0.25 in.) rebar passing through the center of the specimen along its length. For a 152 mm × 305 mm specimen (6 in. × 12 in.), the rebar passes through the specimen along its length but at a depth of 51 mm (2 in.) from the side surface of the specimen, as illustrated in Figure 46. This depth of 51 mm (2 in.) was chosen because in practice columns generally have rebars at a depth of 38–51 mm (1.5–2

in.). A notch was cut in the middle of the rebar prior to producing the test specimens so that cracks could be produced near this location once the rebar was loaded, see Figure 46.

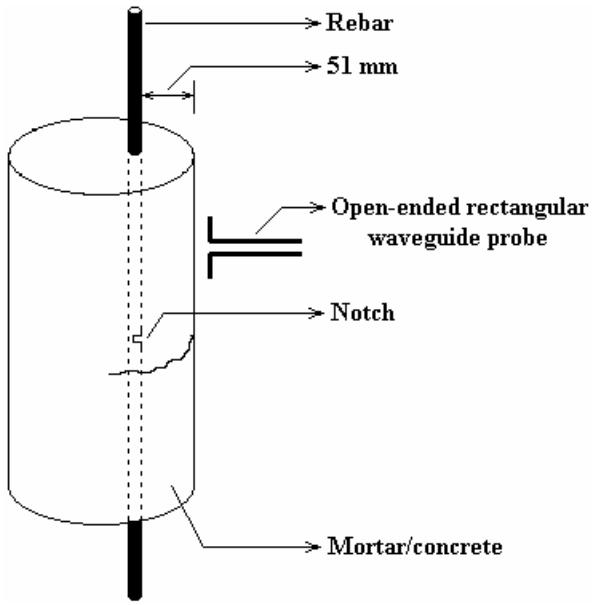

Figure 46 Schematic of a load-induced crack at the location of notch on rebar.

The portion of the rebar protruding out of the specimen was attached to a Tinius Olsen machine for external loading. As the tension applied on the rebar gradually increases, a transverse crack is expected to initiate at the location of the notch and propagate to the closest surface of the specimen. After reaching the surface and upon further loading, the crack widens while slowly extending to the other side of the specimen. The specimen breaks when a crack propagates throughout its cross-section.

Testing Procedure and Results

As the loading on the rebar was gradually increased, a single one-dimensional (1-D) scan was performed along the length of the specimen for each increment of loading using a microwave reflectometer. All of the line scans obtained at each increment of loading were later compared with the line scan performed at zero loading (average/static variation) to detect the presence of a load-induced crack and its propagation.

These 1-D scans were conducted manually by moving the open-ended rectangular waveguide over the specimen while recording the diode detector voltage. The system records the diode detector voltage at a rate of 100 data points per second. The number of data points recorded in each scan depends upon the speed at which the manual scan is performed. Also, with a non-constant speed during each individual scan, the recorded data is either compressed or expanded in time. Using a cross-correlation approach, the scans can be properly lined up and compared.

Several mortar specimens, Figure 47, were tested at X-band and J-band. The results of one 102 mm × 203 mm (4 in. × 8 in.) mortar specimen tested at X-band are presented in Figure 48. The mortar specimen was scanned with a standoff distance of 3 mm and at 0º incidence angle. The

corresponding unprocessed data is shown in Figure 48. These sets of scans were performed at the same location for each increment of loading. All of them fall in the same range of voltage, but in Figure 48 they were shifted so as to depict the differences between them. As explained earlier, these line scans are aligned in space by cross-correlating them with the no load condition (reference line scan) on the rebar as shown in Figure 49.

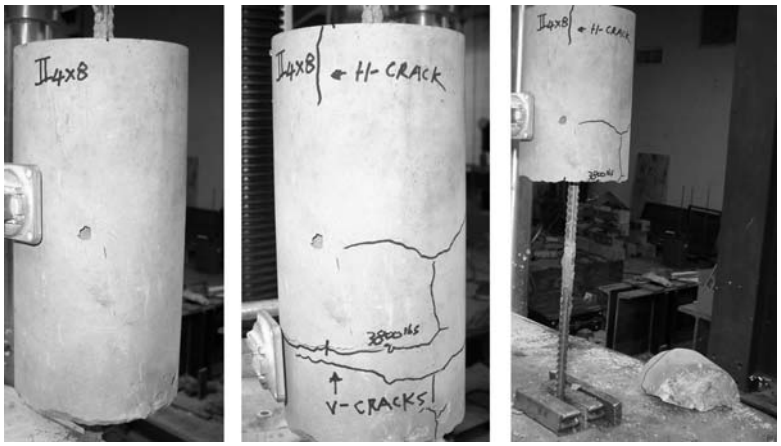

Figure 47 Mortar cylinder testing with an X-band rectangular waveguide.

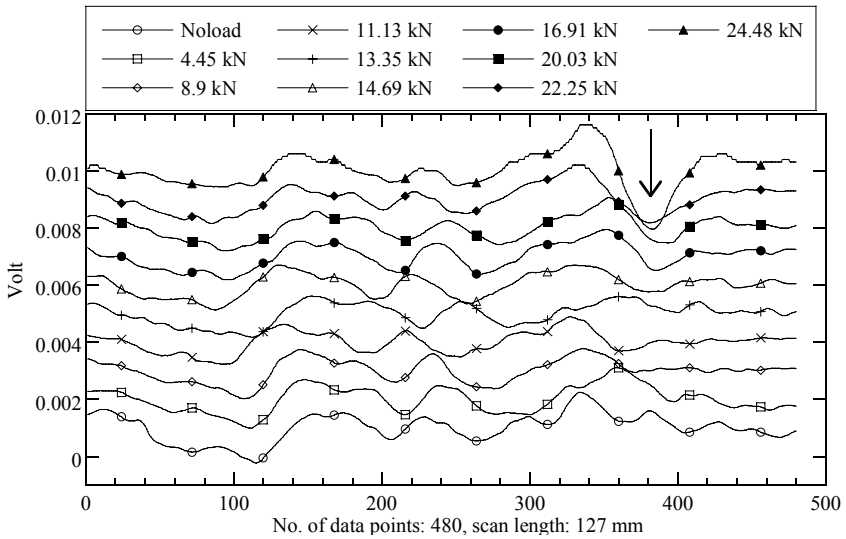

Figure 48 Unprocessed line scans for various loadings on mortar specimen at X-band.

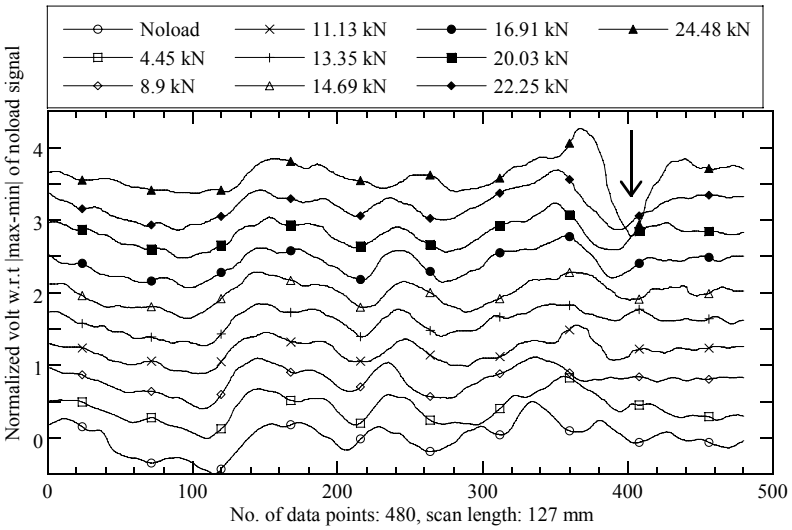

Figure 49 Aligned line scans for various loadings on mortar specimen at X-band.

From Figure 49, it can be seen that the prominent features of the line scan for the no load condition, also referred to as the average/static variation, are preserved in all of the line scans. This particular specimen failed at about 25.81 kN (5800 lbf). The last scan performed before the specimen failed was at a load of 24.48 kN (5500 lbf) and, at this load, the specimen had a hairline crack throughout its cross-section. Thus, the difference in line scans obtained at 24.48 kN (5500 lbf) of load and at no load should have the crack characteristic signal. The topmost graph in Figure 49, corresponding to 24.48 kN (5500 lbf) of load, clearly shows a crack characteristic signal. It can also be seen that the crack characteristic signal does exist in some of the other scans. In order to see the crack characteristic signals more clearly, the static variation at no load was removed from all line scans. Figure 50 shows the difference obtained after removing the average/static variation. We can see the presence of crack characteristic signal starting from 16.91 kN (3800 lbf) of load. At that load, the hairline crack was barely visible by naked eyes. As the load increases, the crack is widened and the prominence of the crack characteristic signal increases.

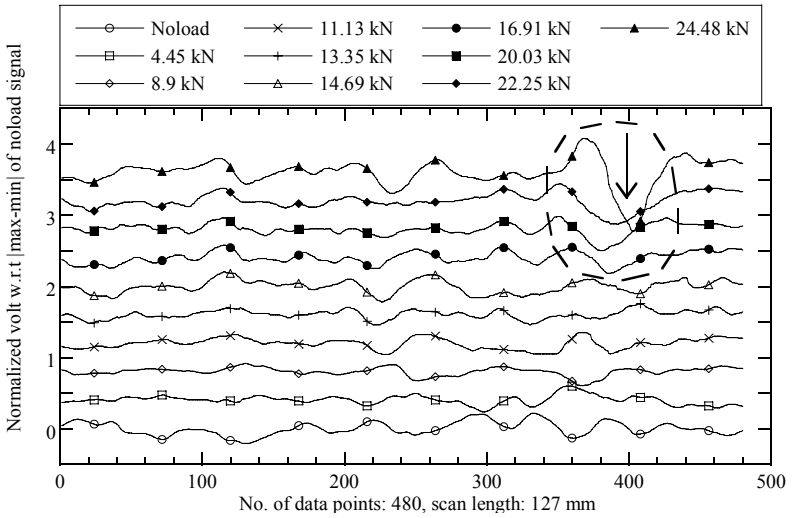

Figure 50 Aligned line scans after removal of the average/static variation at zero load.

Line scans shown in Figure 49 are aligned by cross correlating each of them with no load condition. However, these line scans are not perfectly aligned, implying there is no point-to-point alignment. If the line scans were perfectly aligned, then the coherent subtraction of no load condition from all the line scans would have been more sensitive to detect the presence of crack characteristic signal at a load lower than 16.91 kN (3800 lbf). However, more complex measurement techniques have to be applied to obtain a coherent (i.e., magnitude and phase) measurement.

Cracks of Cyclically Loaded RC Beams in Flexure

Three-foot-long RC beams, Figures 8.15 and 8.16, with a 127 mm × 127 mm (5 in. × 5 in.) square cross-section were tested. Here, line scans were performed simultaneously with two open-ended rectangular waveguides operating at X-band (10 GHz) and K-band (24 GHz). The higher the operating frequency, the smaller the dimension of a rectangular waveguide aperture will be. For example, the K-band waveguide aperture is 10.7 mm × 4.3 mm (0.421 in. × 0.169 in.) smaller than X-band aperture. Rectangular waveguides with smaller apertures are more sensitive to small variations in the local dielectric property of the material than those with larger apertures (X-band). They have the ability to detect cracks of smaller dimensions (high resolution). However, they are also sensitive to non-crack local variations, such as the presence of coarse aggregates, making it challenging to identify a crack characteristic signal on scanning an inhomogeneous media such as concrete.

The RC beams were initially statically loaded in flexure to generate cracks, as shown in Figure 51. The beams were slowly loaded and unloaded; the amplitude was gradually increased each time. Line scans were performed along the length of the beam after each cycle of loading and unloading operation. After unloading the beam, cracks were partially closed leaving hairline cracks which were barely visible. After removing the static variation, some of these partially closed cracks were detected at K-band (24 GHz) (line scan performed at no load condition) but were not detected at X-band (10 GHz).

Line scans were also performed at different heights from the bottom face of the beam (see Figure 51) where the crack was expected to initiate. The larger the height of the line scan from the bottom face, the smaller the crack width/opening is. This investigation can allow for the potential of this technique to detect real cracks of varying widths to be gauged. However, it was difficult to detect the cracks as they were closing after the beam had been unloaded. In order to generate cracks that remain permanently open to a significant degree after unloading, RC beams were loaded cyclically.

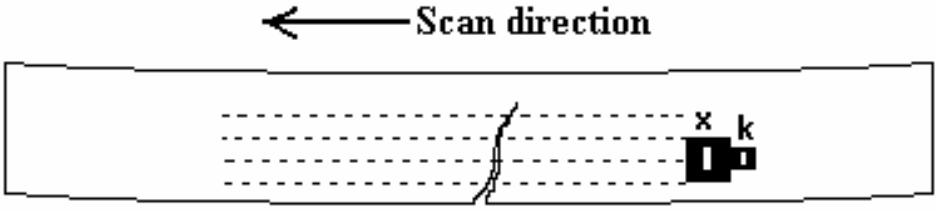

Figure 51 Schematic of testing procedure.

Testing Procedure

Each beam had initial hairline cracks that were induced by loads in the previous static tests. It was then subjected to cyclical loading for a stipulated number of cycles to generate cracks that remain permanently open. Four line scans were performed at heights of 20 mm, 30 mm, 40 mm, and 50 mm from the bottom face of the beam. These set of line scans were repeated after each set of loading cycles. Repeated cyclical loading of RC beams increases the crack opening. In order to measure the increase in width of the cracks, for each crack extensometers were placed on the under side of the RC beams.

A manual scanning system was used to record the detector voltages of X-band and K-band sensors/probes as well as the distance moved by the probes. The manual scanner records 28 data points for every 5 mm (0.2 in.) scanned. As the distance information is recorded by the manual scanner, line scans performed at different cycles can be perfectly aligned to remove the line scan performed at no load condition (static variation). Figure 52 shows the manual scanning system used for scanning the RC beam.

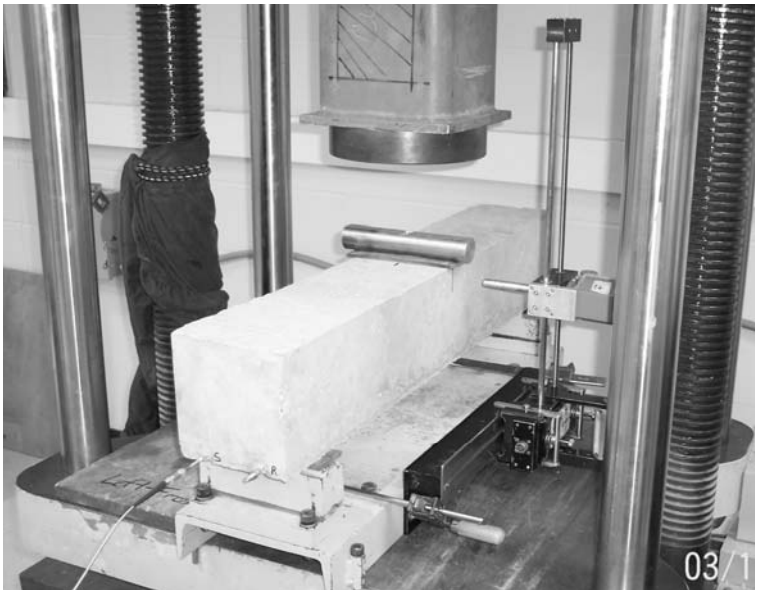

Figure 52 Manual scanning system used for scanning the RC beam.

Results and Analysis

The results of two RC beams scanned at X-band are discussed here. Figure 53(a) shows the first RC beam before cyclical loading with two extensometers attached to the bottom face of the beam. Figure 53(b) shows the cracks on the RC beam after cyclical loading. The deflection of the beam during the cycling was set to 7.6 mm (0.3 in.). The RC beam had two hairline cracks prior to cyclical loading. The width of the cracks was measured by the extensometers. After the beam had been cyclically loaded, the cracks were widened to 0.675 mm (0.0266 in.) and 0.244 mm (0.0098 in.), respectively.

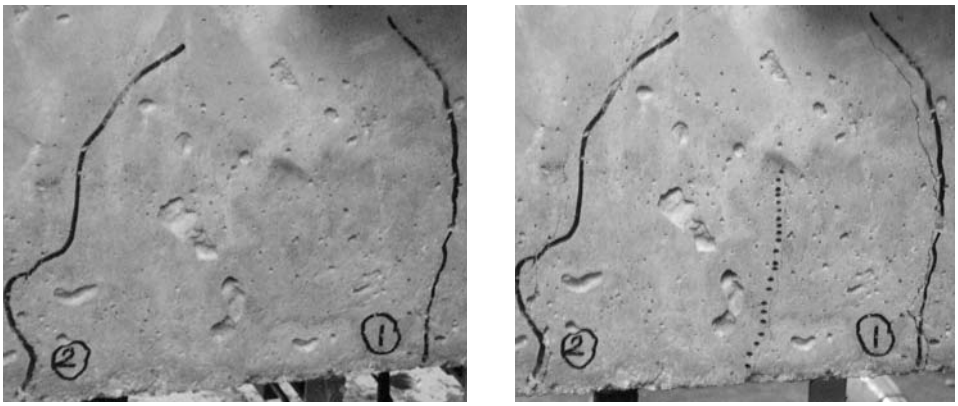

(a) Before cyclic test (b) After cyclic test

Figure 53 Cracks in RC beam: (B3 in Table 3).

The results of scanning this RC beam with a K-band waveguide are inconclusive because of the severe surface roughness of the specimen. The size of the voids present on the surface of the RC beam, Figure 53(a, b), are about the size of a K-band waveguide aperture. Thus, the surface roughness resulted in high reflection at the waveguide aperture and subsequently masked the crack characteristic signals.

Figure 54 shows the results of scanning the RC beam with an X-band waveguide at a standoff distance of 4 mm (0.156 in.). The line scans shown in the figure are performed at a height of 30 mm from the bottom face of the RC beam. Figure 55 shows the results of line scans after removing the line scan conducted before cycling (0 cycles), which clearly depict crack characteristic signals of both cracks.

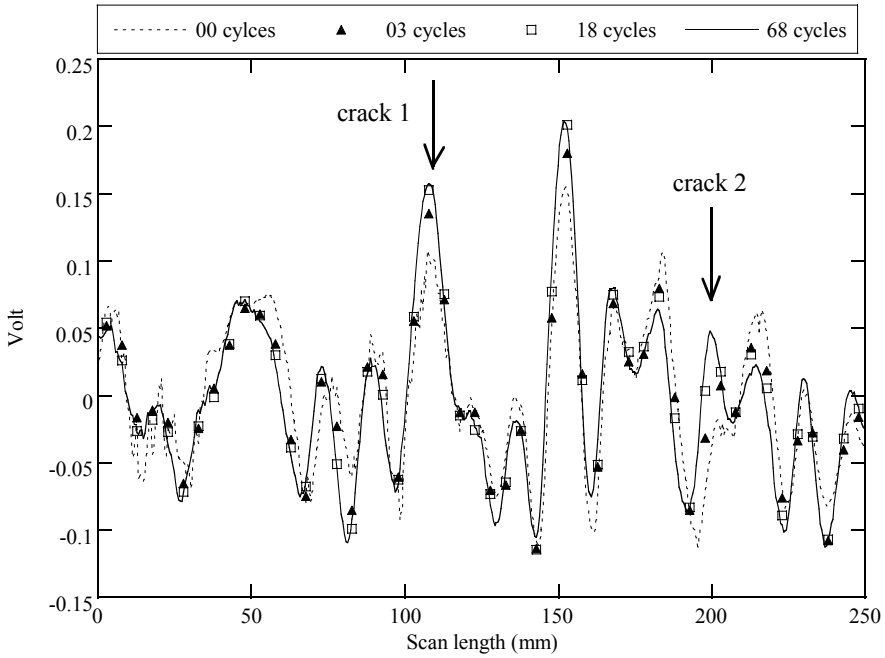

Figure 54 Line scans conducted after various cycles at X-band.

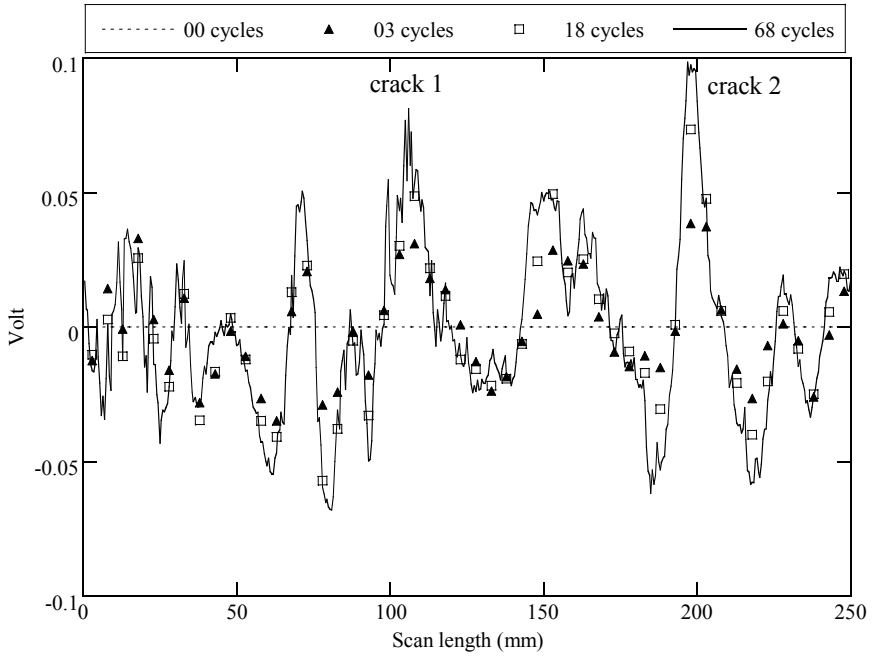

Figure 55 Difference line scans with static variations removed.

The second beam also had two cracks present prior to cyclical loading. One crack was present at the center of the beam to which an extensometer was attached, and the other was a hairline crack at a distance of about 90 mm (3.54 in.) from the center of the beam. The deflection of the beam during the cycling was set to 5.6 mm (0.22 in.). Figure 56(a) shows the RC beam before cyclical loading with the extensometer attached to the bottom face. Figure 56(b) shows the cracks on the RC beam after 105 cycles of loading. The extensometer indicated that the width of the center crack was widened by 1.6 mm (0.063 in.) as a result of the cycling action. The hairline crack which was present prior to the cyclical loading also expanded, and a third hairline crack appeared in between the two existing cracks.

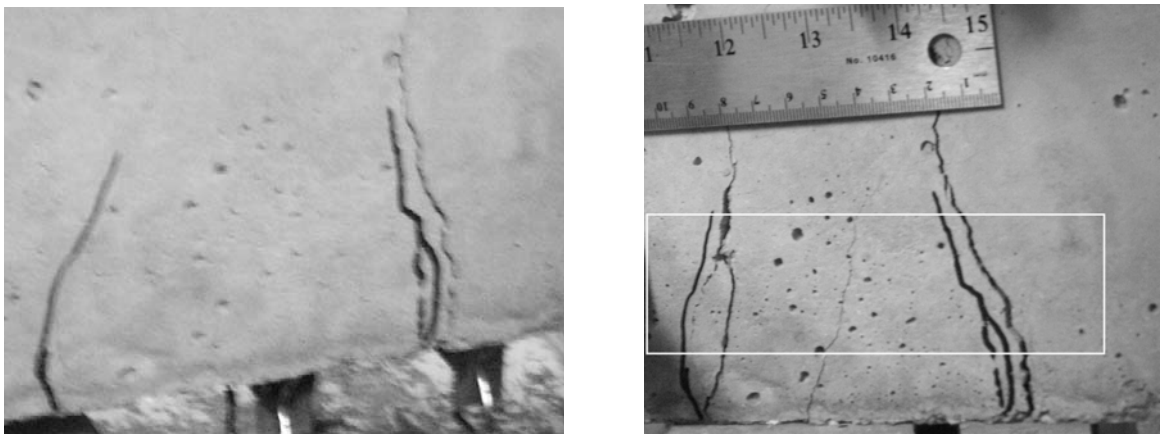

(a) Before cyclic test (b) After cyclic test

Figure 56 Cracks in RC beam (B3 in Table 3).

The surface of the second beam is relatively smoother without many voids present. Thus, the results were better than the results obtained with the first beam. Four line scans were performed

at heights of 20 mm (0.787 in.), 30 mm (1.181 in.), 40 mm (1.575 in.), and 50 mm (1.968 in.) from the bottom face of the beam. The sets of line scans performed at different heights were placed adjacent to each other forming a 2-D microwave image.

The microwave images of the boxed area in Figure 56, which was scanned with an X-band waveguide at a standoff distance of 5 mm (0.197 in.), were presented in Figure 57(a) before a cycling load was applied, in Figure 57(b) after 65 cycles of loading, and in Figure 57(c) after 105 cycles with the static variation removed. In these figures, two data points were plotted for every 1 mm (0.0394 in.) scanned. It can be observed from Figure 57(c) that all three cracks, and the new hairline crack in between the two existing cracks, can be clearly identified. As indicated in Figure 57(b), the new hairline crack has not yet formed after 65 cycles of loading. At this stage, even the left crack induced during static tests was narrow and short, as seen from the image.

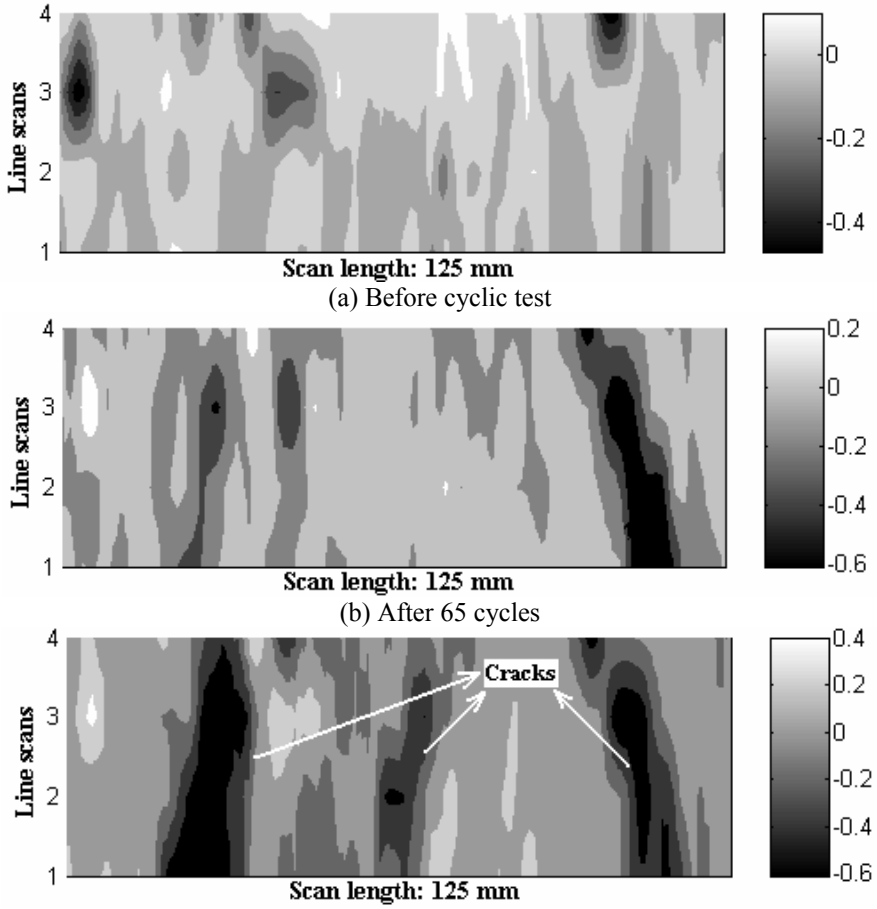

(a) Before cyclic test

(b) After 65 cycles

(d) After 105 cycles with static variation removed

Figure 57 X-band microwave images of scanned area: 4 lines with 125 mm of scan length.

The microwave images scanned with a K-band waveguide at a standoff distance of 4 mm (0.157 in.) are shown in Figure 58(a, b) before and after a cyclic load was applied on the beam, respectively. Since K-band sensor is more sensitive to local variations than X-band, the reflection from the surface of the beam is much higher because of the presence of voids or coarse aggregates. As a result, the crack characteristic signals present around the voids or aggregates were masked, as indicated in Figure 58. It can be seen from Figure 58(a) that a high reflection

was recorded in the middle region of the beam where the new hairline crack is later formed as a result of cyclical loading. Figure 58(b) shows only two cracks, and the new hairline crack formed between them was masked.

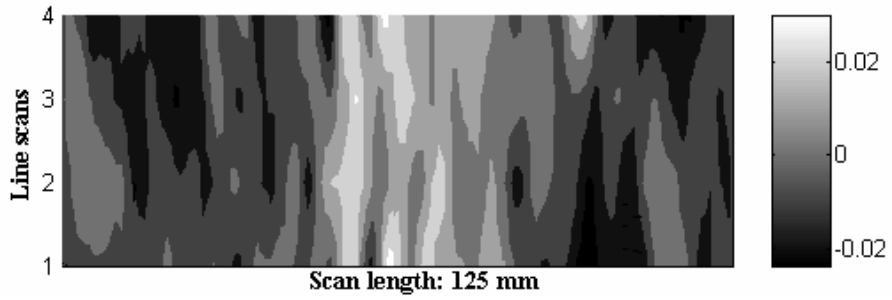

(a) Before cyclic test

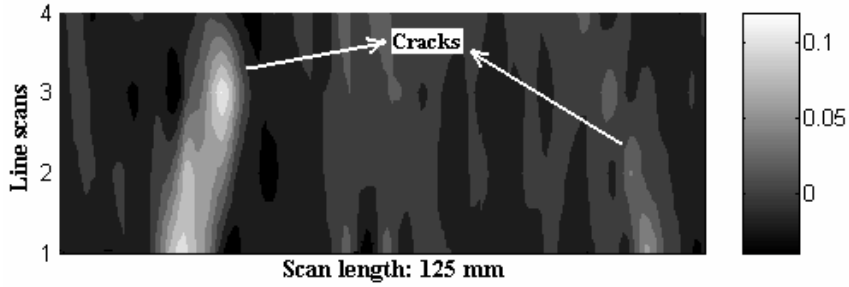

(b) After 105 cycles

Figure 58 K-band microwave image of scanned area: 4 lines with 125 mm of scan length.

The complete set of results of cyclical loading the RC beams indicated that crack characteristic signals performed at different heights from the bottom face of the beam have signal strengths proportional to the crack width. Thus, line scans performed away from the bottom face do not show the presence of crack characteristic signals as the crack widths get smaller.

ELECTROMAGNETIC MODELING

The microwave images obtained from the rectangular waveguide sensor, or crack characteristic signals, can be used to locate cracks on the surface of RC members. It is difficult, however, to utilize the images for the determination of crack width and depth. To quantify their relation, an electromagnetic model will be developed in this section. Such a model can be applied to optimize the measurement parameters for crack detection and, more important, to extract the information on crack width and depth from the crack characteristic signal. This extraction process is typically referred to as a reverse engineering problem, which is difficult to solve in practical applications. As a first step toward this endeavor, a forward model will be developed in this section, allowing the simulation of the crack characteristic signals of a cracked concrete surface given the operating frequency, crack width, crack depth, dielectric property of the concrete, waveguide dimensions, and standoff distance. To simplify the simulation, cracks are assumed to have an infinite depth. This will ensure that there is no microwave signal reflecting back as a result of the termination of the crack.

Mortar Specimens

Two mortar specimens having dimensions of 102 mm × 203 mm × 203 mm (4 in. × 8 in. × 8 in.) were prepared with 0.55 water-to-cement ratio and 2.25 sand-to-cement ratio. These mortar cubes were used to produce the cracks of various widths, as shown in Figure 59. The depth of the simulated cracks is 203 mm (8 in.), and at such depth the microwave signal reflected from the crack termination is negligible. Thus, these simulated cracks can be assumed to be electrically infinitely deep. This arrangement of mortar cubes allows the simulation of any crack width, which is important for the calibration of the electromagnetic model.

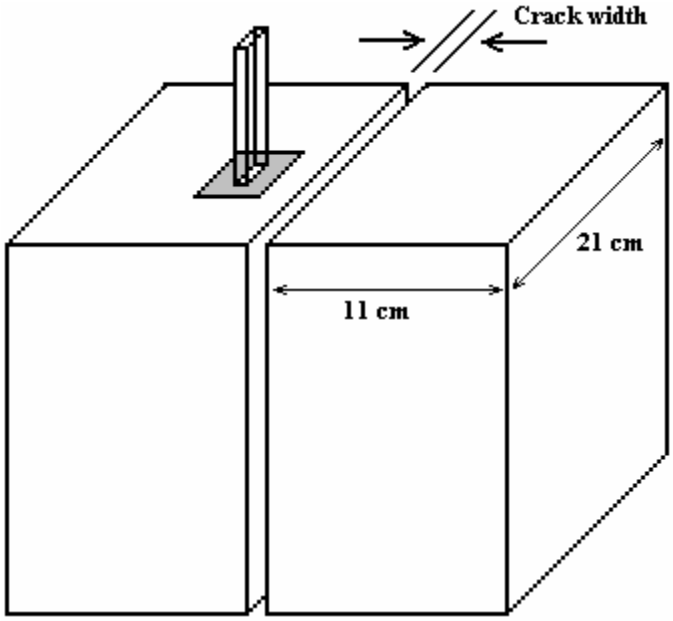

Figure 59 Arrangement of mortar cubes to simulate crack.

Calibrated Measurements With Network Analyzer (Coherent Measurements)

A total of three crack widths, 0.5 mm, 1.0 mm, and 2.0 mm (0.02 in., 0.039 in., and 0.078 in.), and ten standoff distances from 0.5 mm (0.02 in.) to 5.0 mm (0.195 in.) in steps of 0.5 mm (0.02 in.) will be considered to facilitate the development of the forward model. For calibration of the model, the arrangement shown in Figure 59 was scanned with an open-ended rectangular waveguide for each crack width and several standoff distances. The magnitude and phase of reflection coefficient was measured with an HP8510C vector network analyzer. These measurements were conducted every day as the mortar specimens were curing, starting from day 3 to day 13. The average dielectric property ($\varepsilon'_r - \varepsilon''_r$) of the mortar specimens was also measured every day (Bois et al., 1999). Crack characteristic signals were obtained as a function of varying standoff distance, crack width, and dielectric property of mortar specimens. Figure 60(a, b) shows the magnitude and phase of the reflection coefficient as a function of standoff distance for a 2 mm (0.078 in.) wide crack on day 13. Figure 61(a, b) shows the magnitude and phase of the reflection coefficient as a function of crack width at a standoff distance of 2.0 mm (0.078 in.) on day 13.

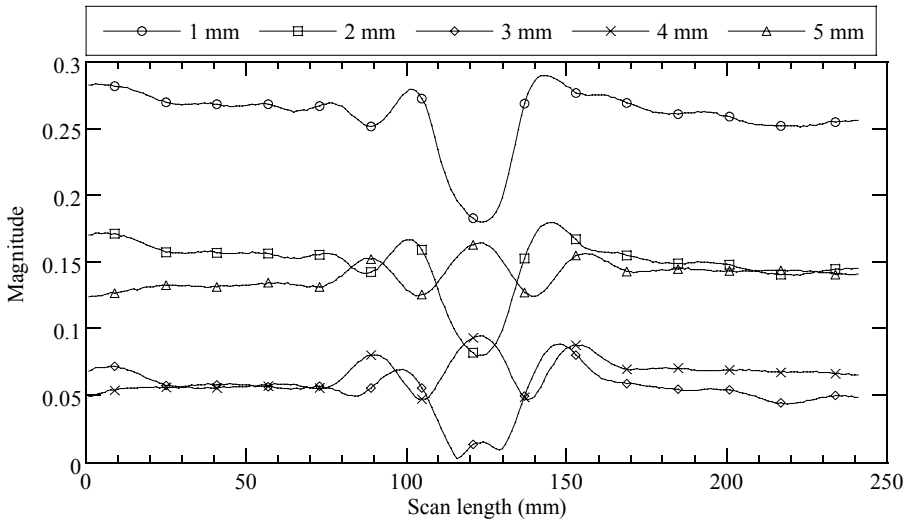

(a) Magnitude

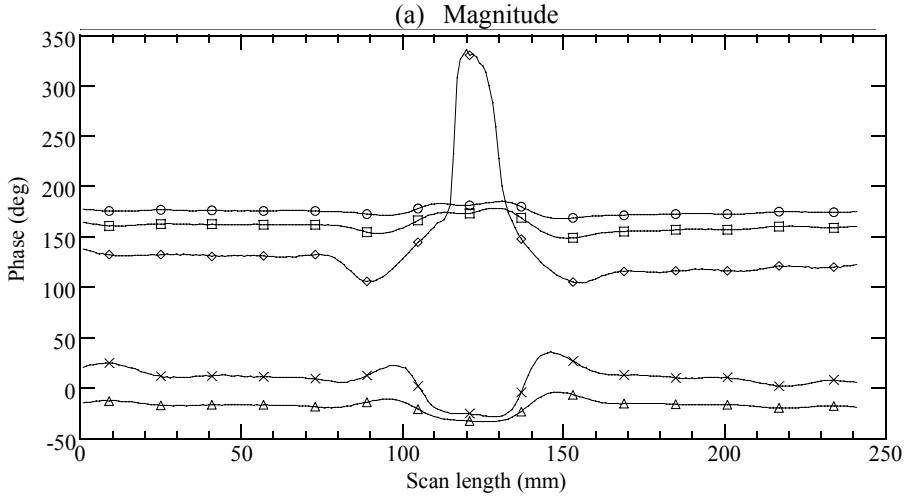

(b) Phase

Figure 60 Reflection coefficient for a 2 mm-wide crack on day 13 at different standoff distances.

The small degree of asymmetry in the crack characteristic signals shown in Figures 8.60 and 8.61 is primarily attributed to the not-so-sharp edges of the crack produced using two mortar cubes. Figure 62 shows the measured average dielectric property ($\varepsilon'_r - \varepsilon''_r$) of mortar cubes from day 3 to day 13 (Bois et al., 1999). It can be observed that the water content decreases as the specimen cures, lowering its dielectric property. Figure 63(a, b) shows the magnitude and phase of reflection coefficient as a function of dielectric property of the specimen. As a result of reduction in dielectric property of the specimen, the magnitude of reflection coefficient effectively decreases.

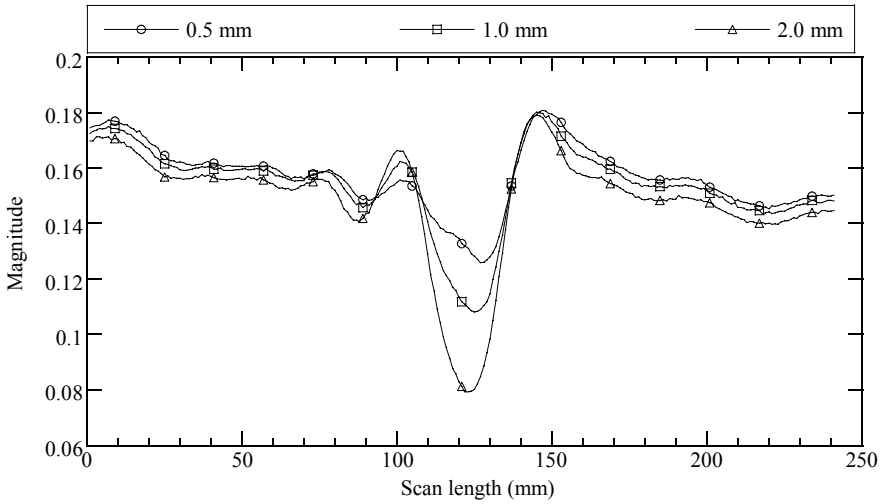

(a) Magnitude

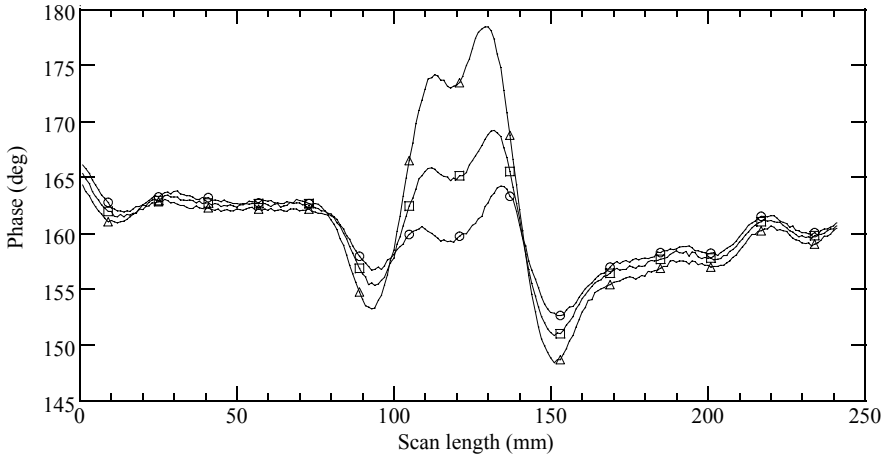

(b) Phase

Figure 61 Reflection coefficient for different crack widths at a standoff distance of 2.0 mm on day 13.

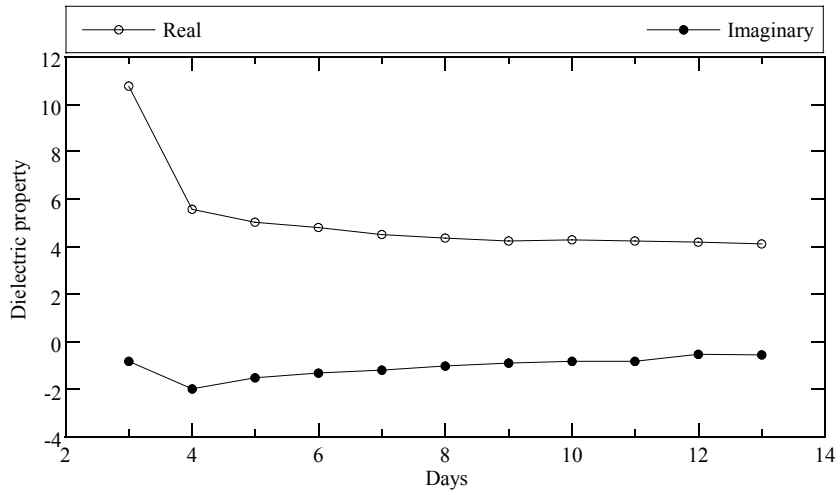

Figure 62 Average dielectric property of mortar cubes from day 3 to day 13.

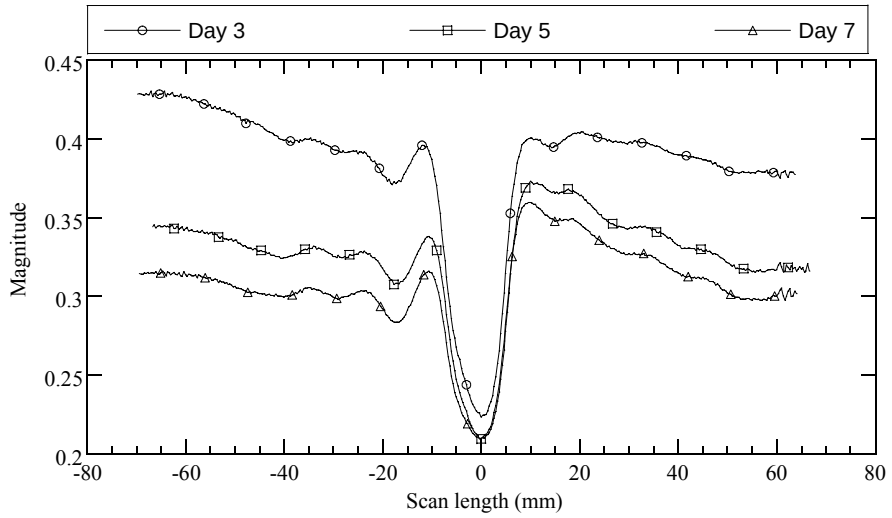

(a) Magnitude

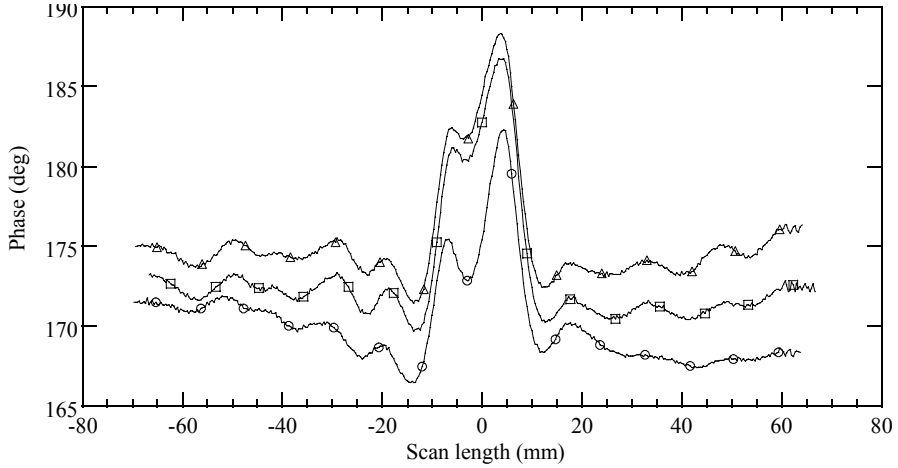

(b) Phase

Figure 63 Reflection coefficient for a 2 mm-wide crack at a standoff distance of 0.5 mm measured on different days.

Similarity to Eddy Current Signals

By examining the magnitude and phase of the crack characteristic signals shown in Figure 60, it seems that these signals do not follow any particular pattern. However, after the magnitude and phase of a crack characteristic signal are presented in a complex plane, a unique feature is revealed. For example, Figure 64 shows how magnitude and phase of the crack characteristic signal of a 2-mm (0.078 in.) crack measured at a 2 mm (0.078 in.) standoff distance vary in the complex plane. The complex representation of the crack characteristic signal looks similar to the impedance plane diagrams from eddy current testing, which is promising for the determination of crack width.

The crack signal in the complex plane looks like a spiral that opens up as the waveguide flange approaches the crack and reaches the tip of the spiral when the waveguide aperture is exactly in the middle of the crack. This part of the crack signal is represented by empty circles in Figure 64.

The crack characteristic signal should then retrace back to the center of the spiral as the waveguide crosses over the crack. However, as shown in Figure 64, the crack signal in the complex plane does not retrace to the center of the spiral on the same exact path. As mentioned earlier, this asymmetry in the crack characteristic signal is primarily attributed to the not-so-sharp edges of the crack produced using two mortar cubes.

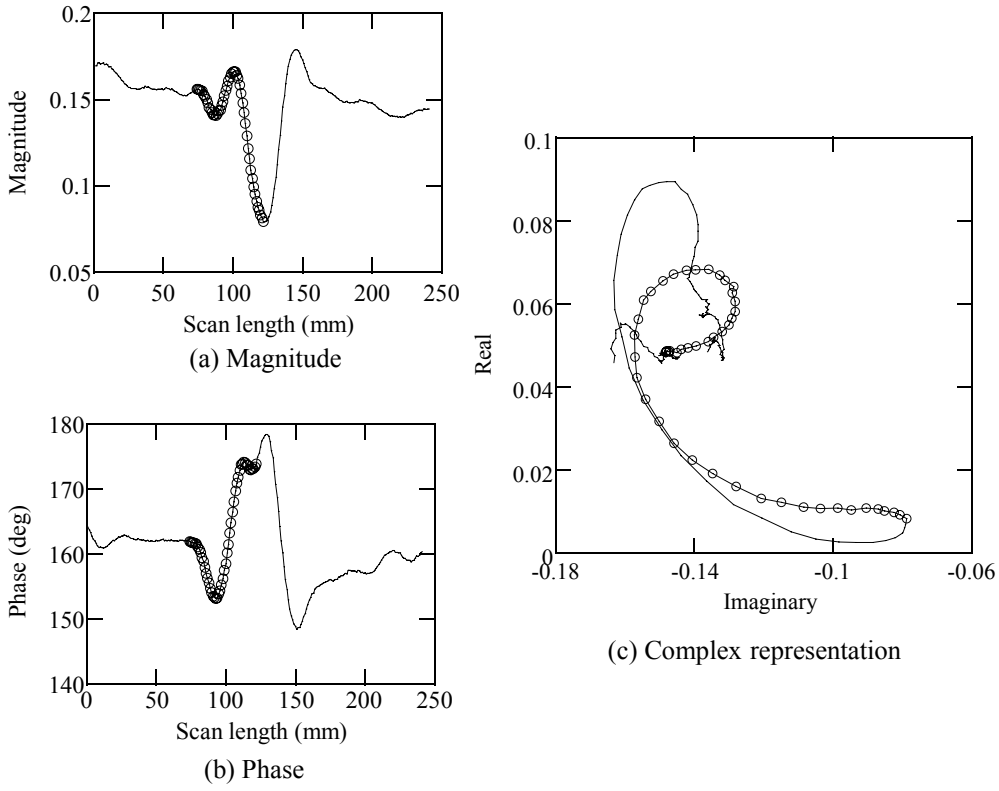

Figure 64 Complex plane representation of reflection coefficient of 2 mm wide crack at a standoff distance of 2.0 mm on day 13.

Variation of Standoff and Crack Width

In an ideal case such as a crack on a smooth concrete surface, the crack characteristic signal is expected to be symmetric about the center line of the crack. Therefore, only half of the crack signal is plotted in the following presentations for the purpose of calibrating an electromagnetic model. Figure 65 and Figure 66 show the variation of crack signals as a function of standoff distance and crack width, respectively. As one can see, the spiral shape represented by empty circles in Figure 64 is preserved in the complex representation of a crack characteristic signal irrespective of the standoff distance, crack width, and dielectric property of the specimen.

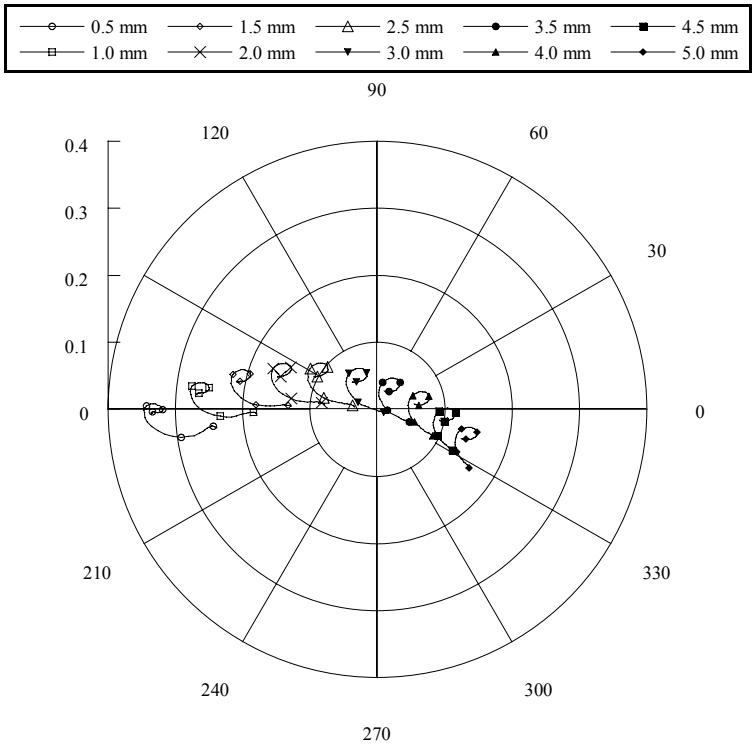

Figure 65 Variation of standoff distance for crack characteristic signals of a 2 mm-wide crack on day 13.

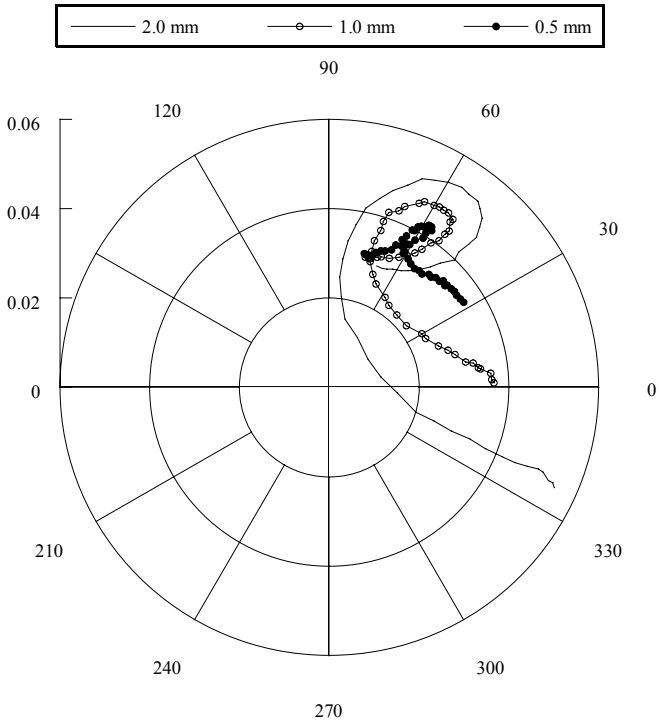

Figure 66 Variation of crack width at standoff distance of 3.5 mm on day 13 for various crack widths.

Numerical Simulations of Crack Characteristic Signal

HFSS (High Frequency Structure Simulator) Model

This section discusses the results of the comparison between measured crack characteristic signals and those obtained from a 3-D electromagnetic field solver. Figure 67 illustrates a schematic of the model developed in Ansoft HFSS 9.0 to simulate a crack (Ansoft Corporation, Pittsburgh, PA).

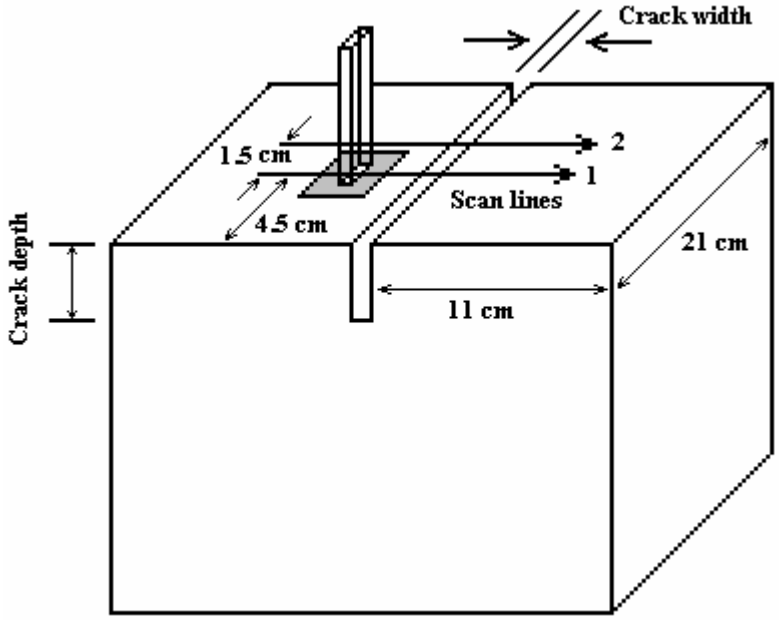

Figure 67 Schematic of HFSS model developed for simulating crack characteristic signal.

A 203 mm × 203 mm × 203 mm (8 in. × 8 in. × 8 in.) mortar specimen was prepared and a notch of 1.143 mm (0.045 in.) wide and 5.0 mm (0.195 in.) deep was cut in it with a hacksaw. The dielectric property of this cube was measured to be (5.96 – j1.02) at 10 GHz. To reduce the computation time in Ansoft HFSS, a smaller mortar block was created with the same notch dimensions. Figures 8.68 and 8.69 show the magnitude and phase of simulated and measured crack characteristic signals obtained at a standoff distance of 1.0 mm (0.039 in.) and 4.0 mm (0.156 in.), respectively. Two sets of measurements were performed along the two scan lines that are parallel to each other and separated by a distance of 1.5 cm (0.585 in.), as shown in Figure 67.

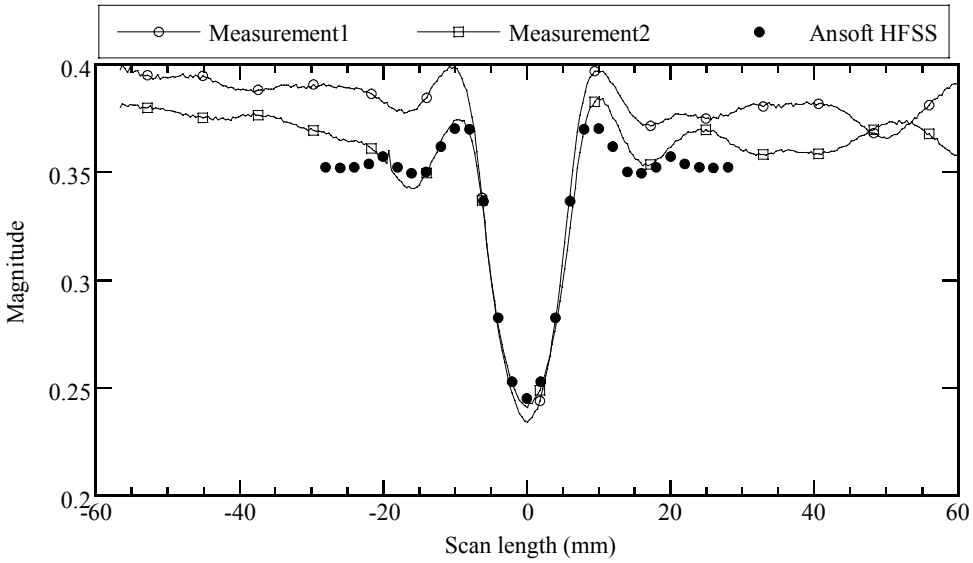

(a) Magnitude

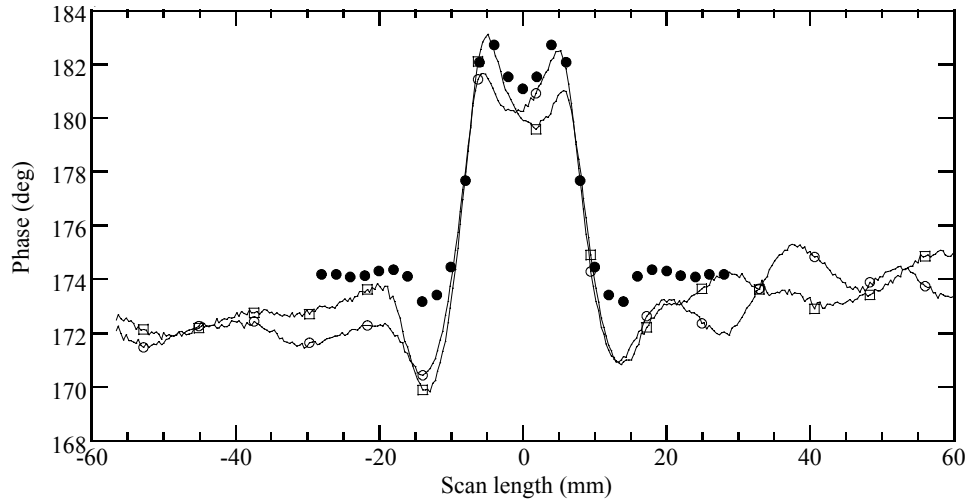

(b) Phase

Figure 68 Measured and simulated characteristic signals of a crack of 1.143 mm wide and 5.0 mm deep: standoff distance = 1.0 mm, dielectric property = 5.96 – j1.02 at 10.0 GHz.

It can be observed that HFSS model can accurately simulate crack characteristic signal given the standoff distance, operating frequency, dielectric property of cement-based material, waveguide dimensions, crack width, and crack depth. However, it should be noted that the simulation time is about one hour to compute one point. It takes approximately 15 hours to simulate one crack characteristic signal using HFSS.

Ansoft HFSS can simulate crack characteristic signals for cracks with finite depth, whereas the empirical model is limited to cracks which are electrically infinitely deep. This tool can be used to simulate crack characteristic signals prior to conducting measurements in the field, which will aid in estimating the sensitivity of rectangular waveguide probes to detect cracks of small dimensions. Ansoft HFSS may also be useful in the inverse problem, which comprises of estimating crack depth and width information from crack characteristic signals.

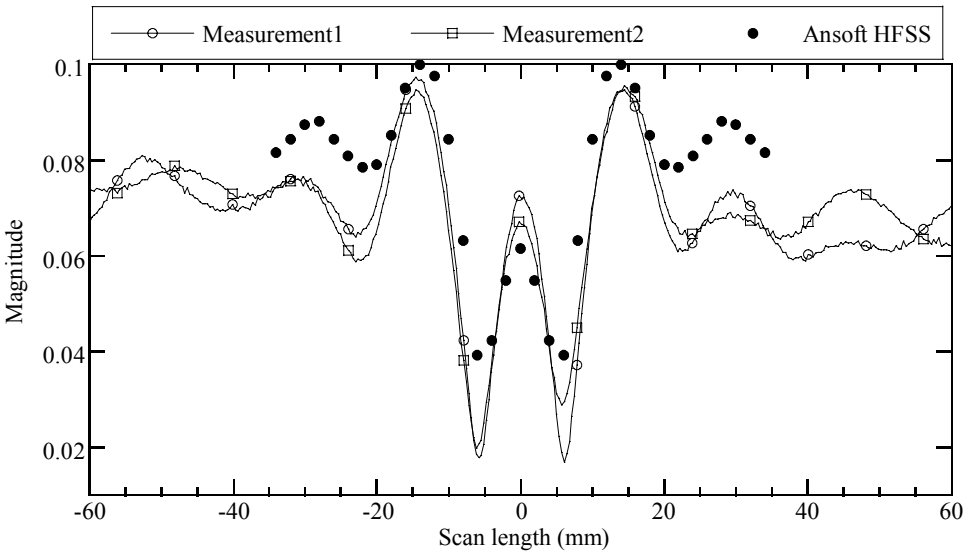

(a) Magnitude

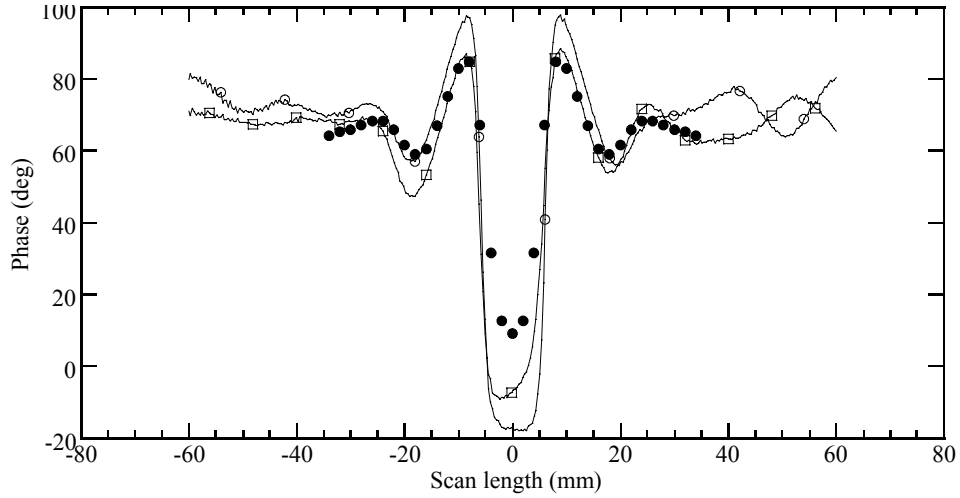

(b) Phase

Figure 69 Measured and simulated characteristic signals of a crack of 1.143 mm wide and 5.0 mm deep: standoff distance = 4.0 mm, dielectric property = 5.96 – j1.02 at 10.0 GHz.

This Study

The empirical model is limited to cracks of infinite depth only and comprises three stages to simulate a crack characteristic signal. The three stages in simulating a crack signal in complex domain involve computing the magnitude and phase of reflection coefficient of open-ended rectangular waveguide at the aperture when:

1. Open-ended rectangular waveguide is placed on an infinite half-space (cement-based material) at a given standoff in the absence of a crack: the starting point.
2. The crack is placed in the middle of the waveguide aperture: the end point.
3. Open-ended rectangular waveguide moves from the starting point (with the crack being located outside the waveguide flange) to the end point (where the crack is located in the middle of the waveguide aperture): the intermediate points.

The starting point, end point, and intermediate points are shown in Figure 70 for a 2.0 mm (0.078 in.) wide crack at a standoff distance of 3.5 mm (0.137 in.) on day 13. Half of the crack characteristic signal can be simulated once these points are computed. The other half of the crack characteristic signal is symmetric wherein the waveguide crosses over the crack to the other side.

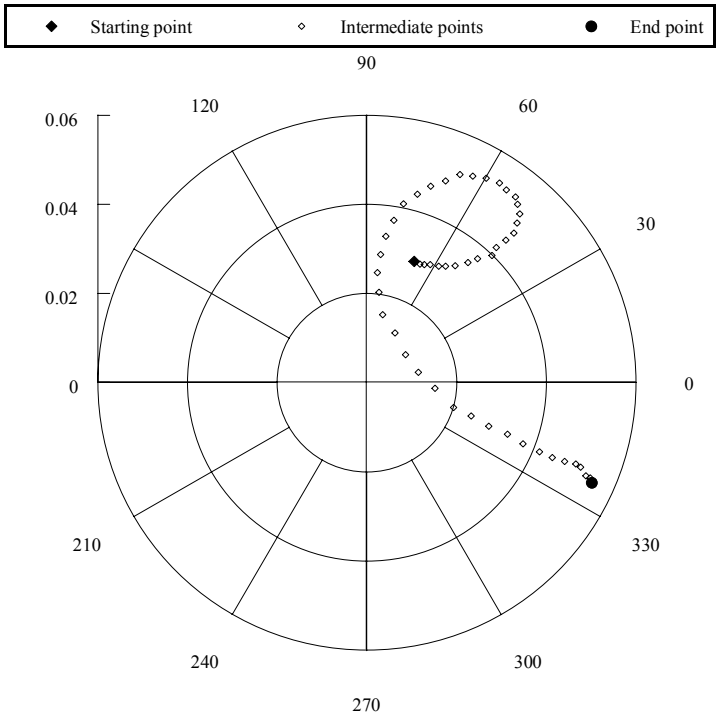

Figure 70 Measured characteristic signal of a 2.0 mm-wide crack at a standoff of 3.5 mm on day 13 comprising of starting point, intermediate points, and end point.

The first step in simulating the crack characteristic signal involves computing the starting point. This can be accomplished by using a custom-built electromagnetic model ("nlayer") available from previous studies dealing with the interaction of open-ended rectangular waveguide with an infinite half-space of a dielectric material (Bakhtiari et al., 1994). The inputs to "nlayer" program are the thickness of each layer, the dielectric property of each layer, and the frequency of operation. In this case, the inputs to the program are the standoff distance and the dielectric property of the cube, as shown in Figure 71. The program computes the reflection coefficient at the open-ended rectangular waveguide aperture. Figure 72 shows a comparison between the computed starting point and the measured crack signals at different standoff distances. These results indicate that the starting points computed from "nlayer" program at different standoff distances agree well with the starting points of measured crack characteristic signals in the complex domain.

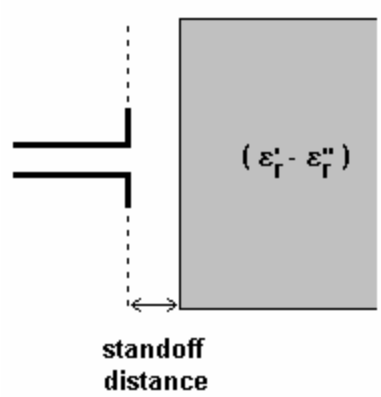

Figure 71 Inputs to "nlayer" code at open-ended waveguide aperture (starting point).

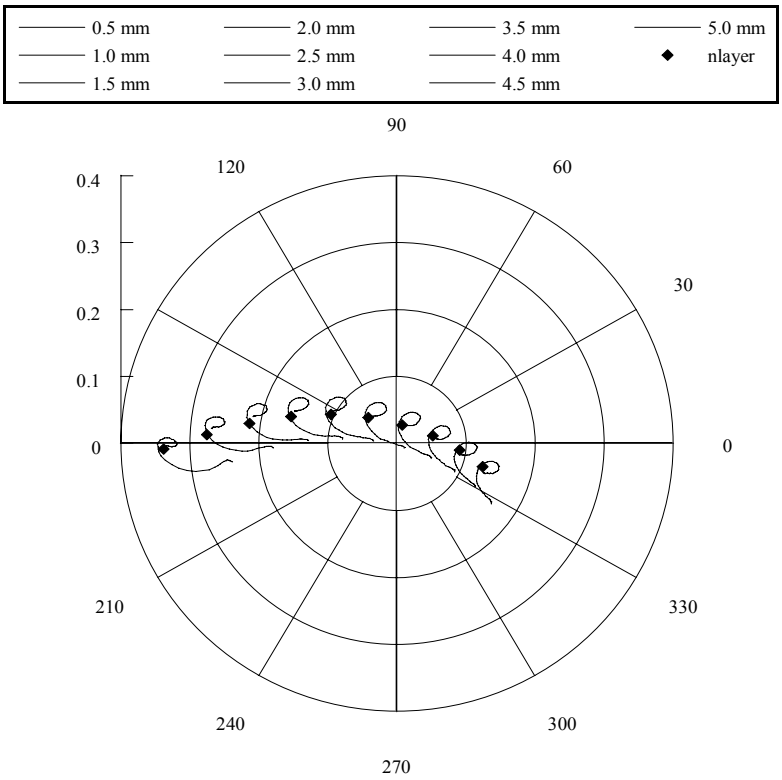

Figure 72 Computed versus measured starting points at different standoff distances for a 2.0 mm-wide crack on day 13 (4.11 – j0.56) at 10.0 GHz.

The second step involves computing the end point when the waveguide is right on top of the crack. This can be achieved by replacing the mortar cube and the crack present in it with an effective dielectric medium ($\varepsilon'_{eff} - \varepsilon''_{eff}$), as shown in Figure 73, and subsequently computing the reflection coefficient from the same "nlayer" code which was used for computing the starting point.

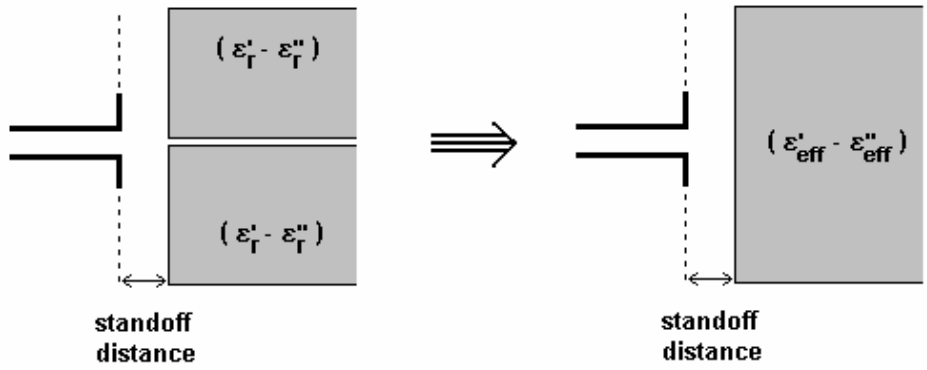

Figure 73 Schematic showing how the model is simplified to compute the end point.

The effective dielectric constant is computed using a simple mixing rule:

$$\varepsilon_{eff} = \varepsilon_{air} \times (volume\ fraction) + \varepsilon_{cement-based\ material} \times (1 - volume\ fraction) \quad (1)$$

However, the volume fraction is weighed with the near-field pattern of the open-ended rectangular waveguide (Qaddoumi, 1998). The near-field pattern for an open-ended rectangular waveguide can be computed using an available electromagnetic model previously developed (Hughes, 2003). Figure 74 shows the electric field intensity plot used to weigh the volume fraction in the dielectric mixing formula.

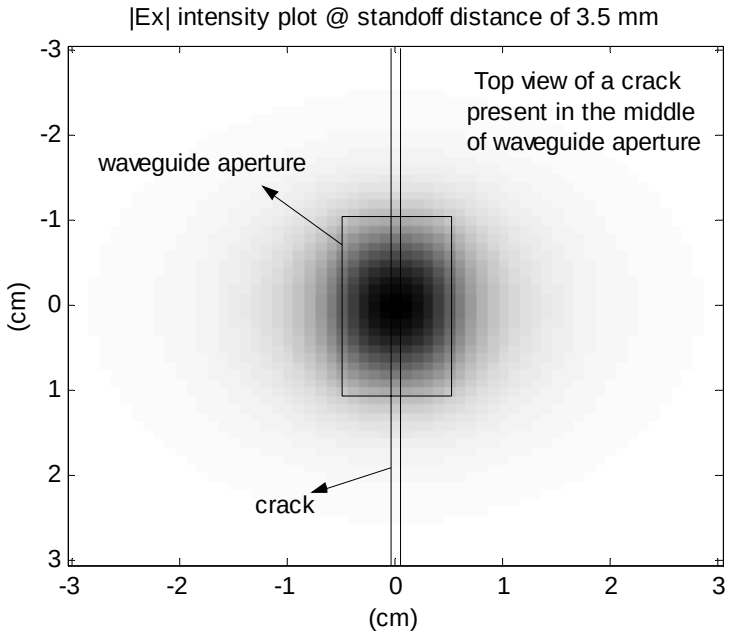

Figure 74 Intensity plot of electric field component perpendicular to the crack with the waveguide at a standoff distance of 3.5 mm at 10.0 GHz.

The third step involves computing the intermediate points which comprise of the reflection coefficient of the open-ended rectangular waveguide with the crack moving from the tip of waveguide flange to the middle of the waveguide aperture. This is accomplished empirically by

taking two template signals from the measurements at standoff distances of 0.5 mm (0.02 in.) and 4.5 mm (0.176 in.) for a crack width of 2.0 mm (0.078 in.). These templates are primarily used to obtain the overall shape of the crack characteristic signal and can be used to simulate a crack of any given width. The standoff distances of 0.5 mm (0.02 in.) and 4.5 mm (0.176 in.) are chosen because these template signals encompass all the possible shapes of a crack characteristic signal, as can be observed from Figure 65. Crack signals at any other standoff distance can be obtained by interpolating or extrapolating the two template signals, as shown in Figure 75.

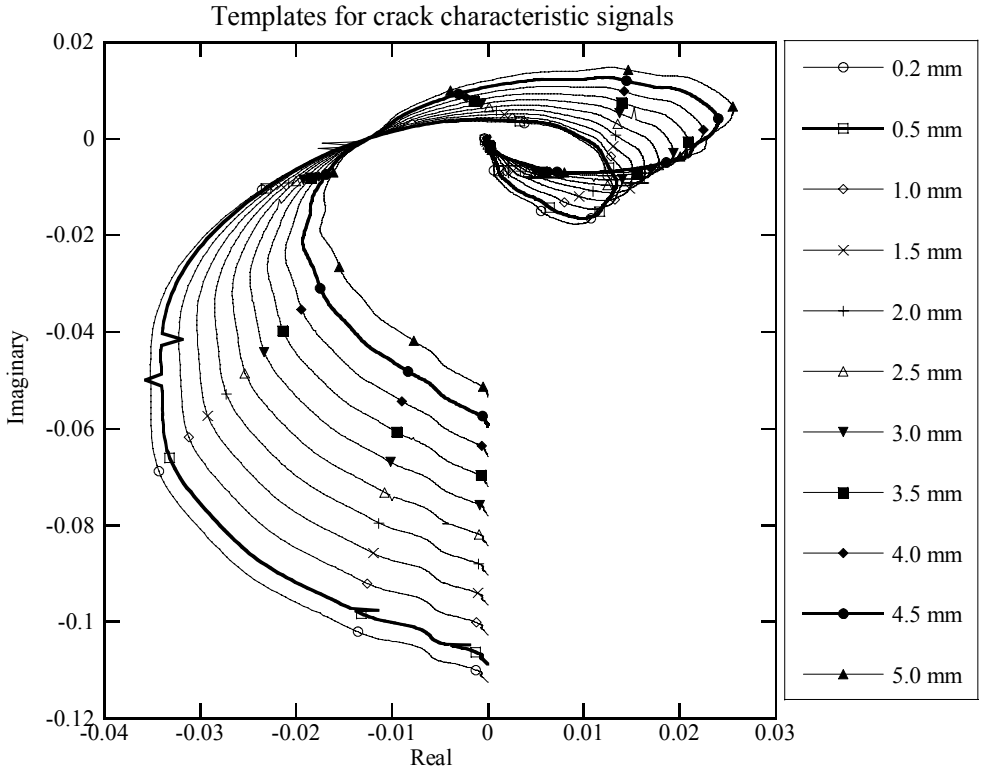

Figure 75 Crack signals at other standoff distances obtained by interpolating or extrapolating the template signals at standoff distances of 0.5 mm and 4.5 mm.

Once the template signal is found for a given standoff distance, a scaled version of this signal is rotated and translated such that it fits between the starting and the end points. Thus, the crack characteristic signal is simulated in the complex domain for a given standoff distance, crack width, and dielectric property of the mortar cube.

Results and Discussions

The simulated crack characteristic signals in the complex domain are unwrapped to get the magnitude and phase plots of the reflection coefficient of open-ended rectangular waveguide. Figures 8.76 through 8.78 are some results showing a comparison between the measured and the simulated crack characteristic signals. For a 2.0 mm (0.078 in.) wide crack, Figures 8.76 and 8.77 show magnitude and phase of measured and simulated crack characteristic signals at standoff distances of 0.5 mm (0.02 in.) and 5.0 mm (0.195 in.). For a 1.0 mm (0.039 in.) wide crack, Figure 78 shows the magnitude and phase of measured and simulated crack characteristic signals at a standoff distance of 3.5 mm (0.137 in.).

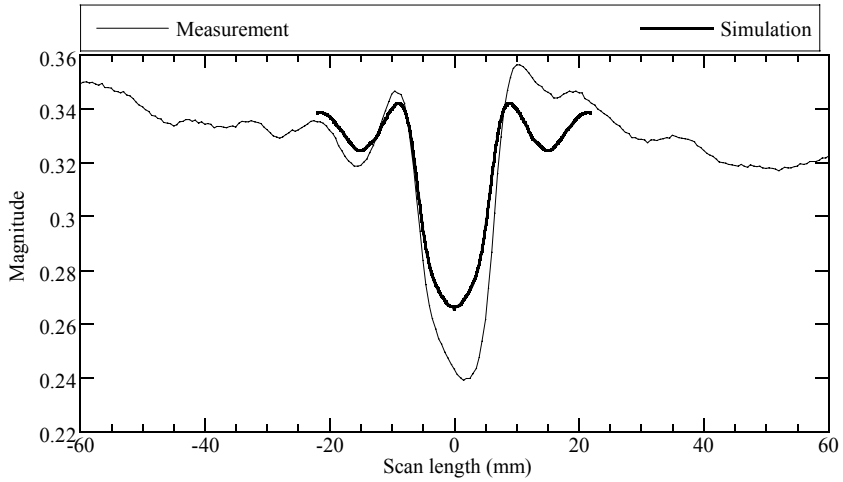

(a) Magnitude

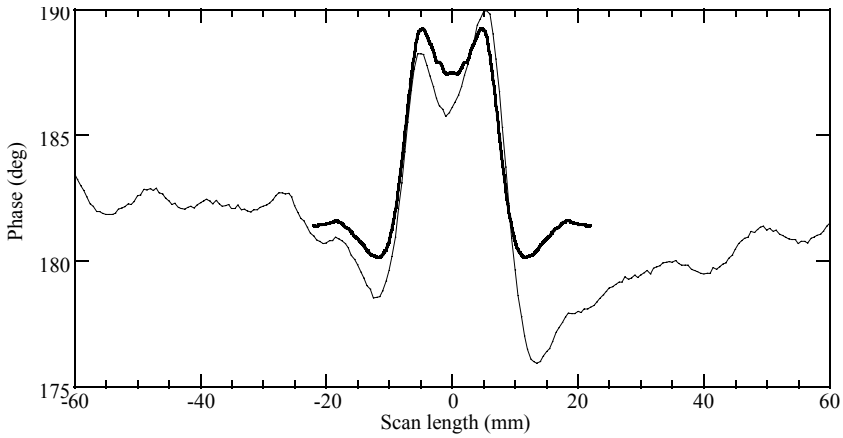

(b) Phase

Figure 76 Measured and simulated crack signals for crack width of 2.0 mm at standoff distance of 0.5 mm.

The results show that the simulated crack characteristic signals are similar to the measured signals. This model has the potential to accurately simulate crack characteristic signals for a given standoff distance, operating frequency, waveguide dimensions, and crack width.

POTENTIAL APPLICATIONS IN CIVIL INFRASTRUCTURES

Both cable sensors and microwave technology can be used to effectively detect surface cracks that are being developed on RC members. Cable sensors are also a viable means of locating hidden cracks near the surface of RC members, or in detecting damage in inaccessible areas. These applications include, but are not limited to:

- Monitoring of the behavior of RC pile and shaft foundations.
- Monitoring of the behavior of massive concrete structures such as dams.
- Monitoring of hidden cracks in RC columns retrofitted with steel, concrete, or FRP jacketing.
- Recording of the damage that has occurred during a recent disaster event such as an earthquake, explosion, and/or wind gust.

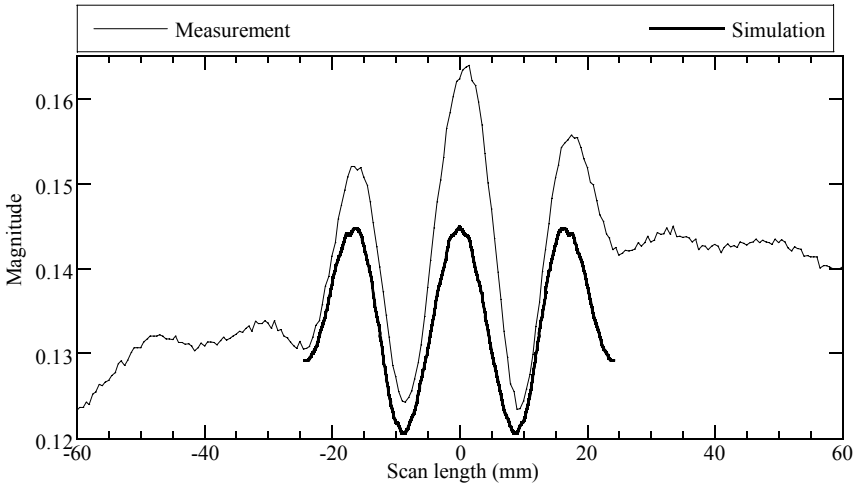

(a) Magnitude

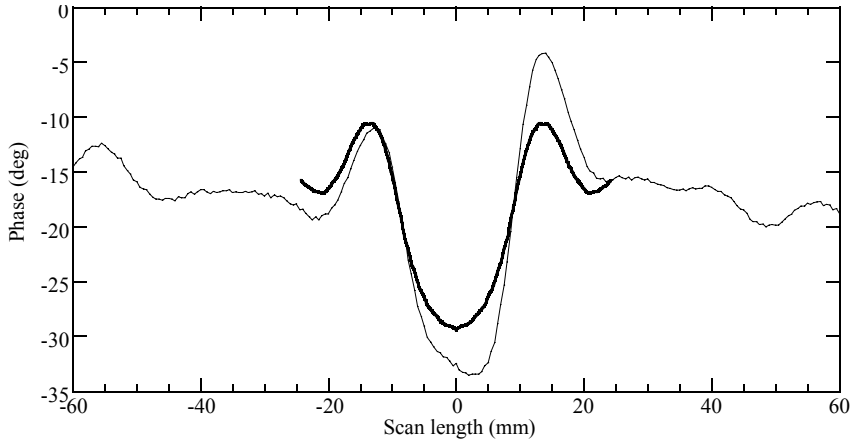

(b) Phase

Figure 77 Measured and simulated crack signals for crack width of 2.0 mm at standoff distance of 5.0 mm.

Two Teflon sensors were installed on the underside of the concrete deck of a bridge being load-tested, perpendicular to the traffic direction, as illustrated in Figure 79(a). The bridge is a three-span structure with a total length of 38.7m (127 ft), Figure 79(b), located in Dallas County, Missouri. The superstructure has three RC beams that were cast integrally with the deck. The sensors were installed in November of 2003 before tests were conducted. As expected, there were no significant changes due to the loading of the bridge. The vehicles were parked back to back, as seen in Figure 80, in the lane opposite to the lane directly above the location of the sensors. The second loading case which affected the sensors, the trucks were parked back to back, similar to Figure 80, but in the center of the bridge width. These tests were repeated in May of 2004. The sensors were once again measured under the same load cases. The data from Figure 81 and Figure 82 reflect the signal from each sensor at zero loading after each load case had been completed in both November and May. Sensor 2 showed little change during the months of inactivity, while Sensor 1 showed a very small crack after the loading test in May. The location of the sensor in the deck was visually inspected for cracks and none were seen.

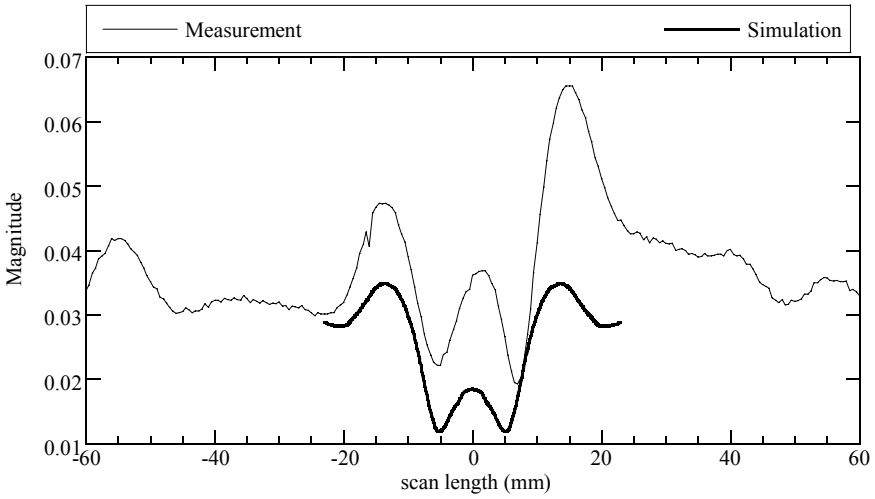

(a) Magnitude

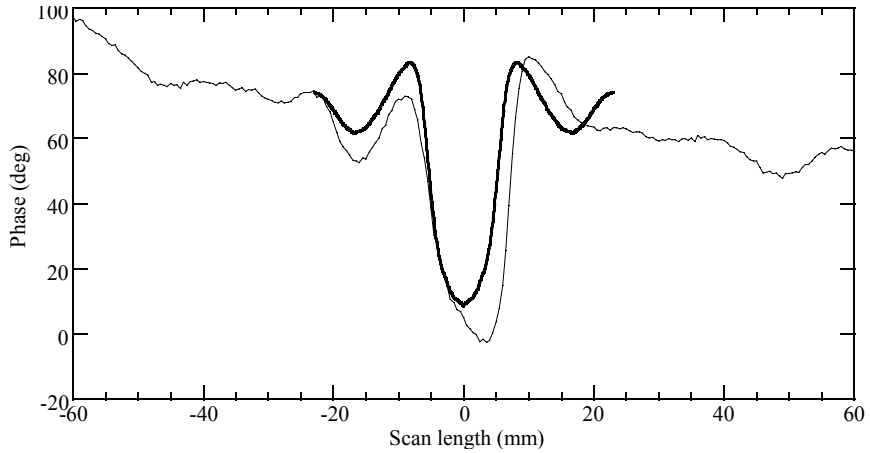

(b) Phase

Figure 78 Measured and simulated crack signals for crack width of 1.0 mm (0.039 in.) at standoff distance of 3.5 mm.

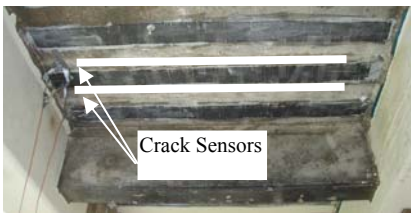

(a) Installed sensors


(b) Overview

Figure 79 Sensor implementation on Dallas County Bridge.

Figure 80 Trucks in loading position.

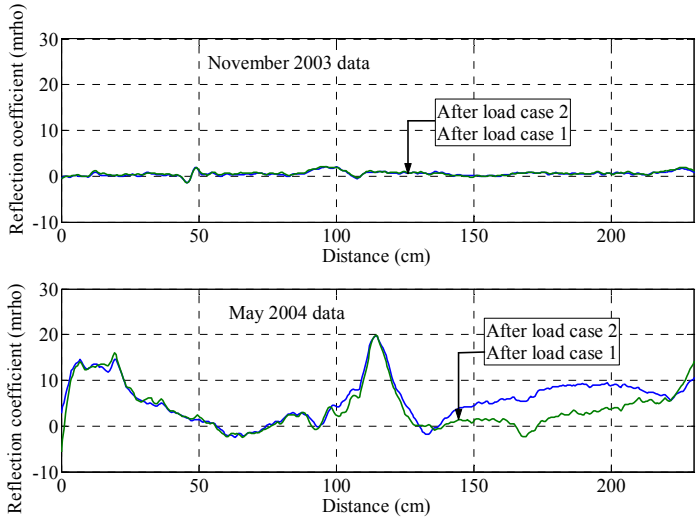

Figure 81 Difference signals taken at zero loading at bridge site (Sensor 1).

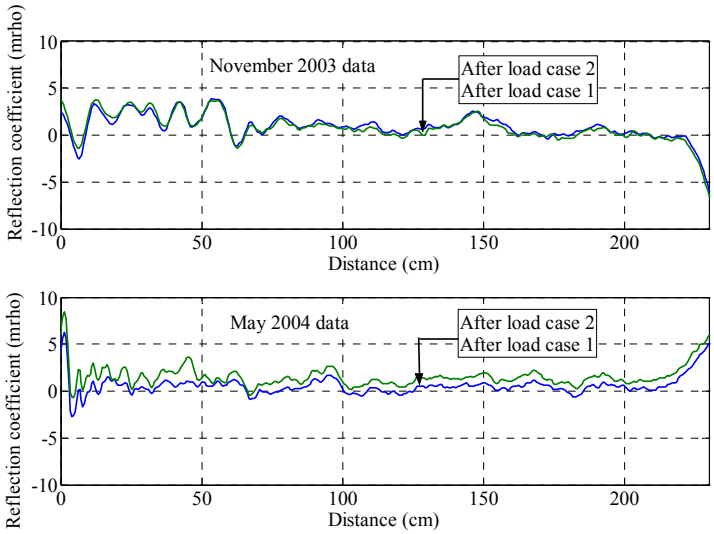

Figure 82 Difference signals taken at zero loading at bridge site (Sensor 2).

CONCLUSIONS

Distributed cable sensors were developed for the location detection and size measurement of cracks that traverse the cables. Their dynamic performance has been studied through the shake table tests of six RC columns. After the discovery of the memory feature of the sensors, an attempt was made to quantify the memory feature with a series of static and cyclic tests of six RC beams. On the other hand, microwave technology was investigated to conduct crack mapping on the surface of an RC member after the location of cracks of structural implications has been identified. Based on the analyses and experiments, the following conclusions can be drawn:

1. The newly designed Teflon sensors have performed well under static and dynamic loads while rubber sensors are more suitable for structures subjected to static loads. Both sensors proved to be rugged and durable. In the shake table column testing application, both sensors survived over 20,000 cycles of loading without failure. In the crack width calibration and

cyclic testing, the Teflon sensors encountered numerous relatively large cracks and did not show any signs of failing.

2. For a particular crack, the increase in crack width was in general agreement with the increase in reflection coefficient at the crack location. However, the relationship between physical width and resulting change in reflected signal is inconsistent throughout the number of cracks due to multiple crack effects on stress redistribution, unknown sensor-concrete interaction, and adhesion. It was observed that the smallest crack width that is discernable according to the sensor is approximately 0.15 mm (0.006 in.). Although larger than that of the sensors without soldering on spirals, this value is much smaller than the smallest crack width of structural implications.
3. In almost all test cases, the location of the cracks can be clearly identified from the measured signal when the cracks open. Even after the load has been removed, large cracks (> 0.225 mm) can remain permanently discernable in the sensor signal, while small cracks (< 0.20 mm) remain detectable in the signal typically after no more than 15 cycles of loading. The memory feature depends on both the crack width and the number of loading cycles; it is independent of the load rate within the test range up to 7.62 mm/sec (0.3 in./sec).
4. For cyclic testing, the Agilent Infiniium DCA Wide-Bandwidth Oscilloscope is sufficient for the acquisition of reflection waveforms at any time. Even for harmonic/dynamic testing in the frequency range of 1–9 Hz, though somewhat challenging, the capturing of data at the moment of maximum crack width proved to be achievable. In both cases, the signal from the sensor on the TDR screen changes in real time as the cracks opened and closed. This observation reveals the possibility for future data acquisition techniques using a TDR sampling device with a GPIB interface card that will enable a time-history of crack propagation to be captured.
5. To improve upon the lower limit of detectable crack width and the correlation between reflected signal and crack width, further research in three areas is necessary: (a) use of an automatic spray metallization process, (b) understanding of the concrete-to-sensor interfacial and adhesion behavior, and (c) controlled cyclic testing of beams with a progressively increasing single crack.
6. A portable hand-held probe of certain size can be directly applied to map the crack distribution on the surface of a concrete member at a given standoff distance and operating frequency. The width of cracks can potentially be identified by comparing the simulated with the measured crack characteristic signals, which is a function of standoff distance, operating frequency, waveguide dimensions, and crack width. The simulated crack characteristic signals were generated with the electromagnetic model that was developed in this study and well validated with test results.
7. To directly determine the width and depth of a crack, an inverse model needs to be developed to relate the crack size to the magnitude and phase of crack characteristic signals provided the dielectric properties of the material is known a *priori*. The current study also needs to be extended to the detection of cracks that may not be oriented perpendicular to the direction of line scan performed, which is more realistic in practical applications. Therefore, the influence of polarization of signals and crack orientation must be included in both forward and inverse models.

REFERENCES

Bakhtiari, S., Qaddoumi, N., Ganchev, S. I., and Zoughi, R. (1994). "Microwave noncontact examination of disbond and thickness variation in stratified composite media," *IEEE Transactions on Microwave Theory and Techniques,* Vol. 42, No. 3, pp. 389–395.

Benson, C. H., and Bosscher, P. J. (1999). "Time-domain reflectometry (TDR) in geotechnics: a review," *Nondestructive and Automated Testing for Soil and Rock Properties*, ASTM STP 1350, W. A. Marr and C. E. Fairhurst (eds.), American Society for Testing and Materials, West Conshohocken.

Bois, K. J. (1999). "Near-field microwave inspection and characterization of cement-based materials," Ph.D. dissertation, Colorado State University, Fort Collins, Colorado.

Bois, K. J., Benally, A. D., and Zoughi, R. (1999). "Multimode solution for the reflection properties of an open-ended rectangular waveguide radiating into a dielectric half-space: the forward and inverse problems," *IEEE Transactions on Instrumentation and Measurement,* Vol. 48, No. 6, pp. 1131–1140.

Chen, G. D., Sun, S. S., Shen, X. L., Pommerenke, D., Greene, G. G., Belarbi, A., and Mu, H. M. (2003). "Crack detection of a 15-meter long reinforced concrete girder with a single distributed cable sensor," *Proceedings of the 1st International Conference on Structural Health Monitoring and Intelligent Infrastructures*, Tokyo, Japan, November.

Chen, G. D. (2004). "Development and validation of novel distributed coaxial cable sensors for crack detection," *Proceedings of the 3rd Sino-Japan-US Symposium on Structural Health Monitoring and Control*, Dalian, China, October.

Chen, G. D., Mu, H. M., Pommerenke, D., and Drewniak, J. L. (2004). "Damage detection of reinforced concrete beams with novel distributed crack/strain sensors," *Journal of Structural Health Monitoring*, Vol. 3, No. 3, pp. 225–243.

Grozic, J., Lefebvre, M., Robertson, P., and Morgenstern, N. (2000). "Using time-domain reflectometry in triaxial testing," *Canadian Geotechnical Journal*, Vol. 37, pp. 1325–1331.

Huber, C., and Zoughi, R. (1996). "Detecting stress and fatigue cracks: findings and characterizing surface breaks using open-ended rectangular waveguides," *IEEE Potentials,* Vol. 15, No. 4, pp. 20–24.

Huber, C., Abiri, H., Ganchev, S. I., and Zoughi, R. (1997a). "Analysis of the 'crack characteristic signal' using a generalized scattering matrix representation," *IEEE Transactions on Microwave Theory and Techniques,* Vol. 45, No. 4, pp. 477–484.

Huber, C., Ganchev, S. I., Mirshahi, R., Easter, J., and Zoughi, R. (1997b). "Remote detection of surface cracks/slots using open-ended rectangular waveguide sensors: an experimental investigation," *Nondestructive Testing and Evaluation,* Vol. 13, pp. 227–237.

Hughes, D. T. (2003). "Development of the embedded modulated scattering technique for dielectric material characterization," Master thesis, University of Missouri-Rolla, Rolla, Missouri.

Lin, M. W., Abatan, A. O., and Zhang, W. (1998). "Crack damage detection of concrete structures using distributed electrical time-domain reflectometry (ETDR) sensors," *Proceedings of the 5th SPIE Annual Symposium on Smart Structures and Materials: Smart Systems for Bridges, Structures, and Highways*, Vol. 3325, Newport Beach.

Lin, M. W., Abatan, A. O., and Zhou, Y. (2000). "High sensitivity electric TDR distributed strain sensor," *Proceedings of the 7th SPIE Annual Symposium on Smart Structures and Materials*

2000: Smart Systems for Bridges, Structures, and Highways, Vol. 3986, Newport Beach, March.
Mu, H. (2002). "Development and validation of coaxial cable sensors for damage detection of reinforced concrete structures," Ph.D. dissertation, University of Missouri-Rolla, Rolla, Missouri.
Nawy, E. G. (2003). *Reinforced Concrete: a Fundamental Approach*, 5th Edition, Prentice Hall, Upper Saddle River, New Jersey.
Nazmul, I. M., and Matsumoto, T. (2003). "Determination of steel stresses in reinforced concrete structures from crack opening profile," *Proceedings of the Structural Health Monitoring and Intelligent Infrastructure*, Tokyo, Japan, Z. Wu and M. Abe (eds.), Vol. 2, pp. 739–746.
Qaddoumi, N. (1998). "Microwave detection and characterization of sub-surface defect properties in composites using an open-ended rectangular waveguide," Ph.D. dissertation, Colorado State University, Fort Collins, Colorado.
O'Connor, K. M., and Murphy, E. W. (1997). "TDR monitoring as a component of subsidence risk assessment over abandoned mines," *International Journal of Rock Mechanics and Mining Science*, Vol. 34, No.3-4, paper No. 230.
O'Connor, K. M., and Dowding, C. H. (1999). *Geomeasurements by Pulsing TDR Cables and Probes,* CRC Press.
Peer, S. (2002). "Nondestructive evaluation of moisture and chloride ingress in cement-based materials using near-field microwave techniques," Master thesis, University of Missouri-Rolla, Rolla, Missouri.
Pierce, C. E. (1998). "Time-domain reflectometry measurements of localized soil deformation," Ph.D. dissertation, Northwestern University, Evansville, Illinois.
Rao, N. N. (2002). *Elements of Engineering Electromagnetics*, 5th Edition, Prentice Hall of India.
Shull, P. J. (2002). "Nondestructive evaluation: theory, techniques, and applications," pp. 645–712, Marcel Dekker, Inc.
Small, E. (1998). "Condition of the nation's highway bridges," *TR News*, Transportation Research Board, 194, 3–8.
Su, M. (1987). "Quantification of cable deformation with time-domain reflectometry techniques," Ph.D. dissertation, Northwestern University, Evansville, Illinois.
Sun, S. S., Pommerenke, D., Drewniak, J. L., and Chen, G. D. (2004). "Signal loss, spatial resolution, and sensitivity of long coaxial crack sensors," *Proceedings of the 11th SPIE Annual Symposium on Smart Structures and Materials*, San Diego, March.
Vanclooster, M., Mallants, D., Diels, J., and Feyen, J. (1993). "Determining local-scale solute transport parameters using time domain reflectometry (TDR)," *Journal of Hydrology*, Vol. 148, pp. 93–107.
Van Dam, R., and Schlager, W. (2000). "Identifying causes of ground-penetrating radar reflections using time-domain reflectometry and sedimentological analyses," *Sedimentology*, Vol. 47, pp. 534–449.
Yeh, C. (1994a). "Detection and sizing of surface cracks in metals using open-ended rectangular waveguides," Ph.D. dissertation, Colorado State University, Fort Collins, Colorado.
Yeh, C., and Zoughi, R. (1994b). "A novel microwave method for detection of long surface cracks in metals," *IEEE Transactions on Instrumentation and Measurement,* Vol. 43, No. 5, pp. 719–725.

Zoughi, R., Ganchev, S. I., and Huber, C. (1996). “Measurement parameter optimization for surface crack detection in metals using an open-ended waveguide probe,” *Proceedings of the IEEE Instrumentation and Measurement Technology Conference,* pp. 1391–1394, Brussels, Belgium.

Zoughi, R. (2000). *Microwave Non-Destructive Testing and Evaluation*, Kluwer Academic Publishers, the Netherlands.